Data Collection Analysis

Chapter Outline

5.1. INTRODUCTION

The raw data collected in a diffraction experiment take the form of photon, electron, or neutron counts versus some variable, such as diffraction angle, energy, time of flight (tof), etc., which will be converted to a Q value. However, the purpose of the diffraction experiment is to determine the normalized total scattering structure function $S(Q)$ as we have discussed. The data have to be collected and processed so that they yield the structure function with high accuracy. Also the experimental setup has to be designed to make the data analysis easier and more accurate. Here, we spend some time on the strategy of data collection and analysis.

    The measured intensity of scattered electrons, neutrons, or X-rays contain, in addition to scattering from the sample, scattering from the addenda such as

the sample holder and experimental apparatus. The first-order job is to remove all the counts due to scattering from the addenda. Thus, we have to perform scattering measurements without the sample in place to account for instrumental backgrounds. Note, however, when the sample is present, a part of the scattering from the addenda is modified due to sample absorption. This complicates the process. In addition, some photons, electrons, or neutrons are scattered twice or more times in the sample and elsewhere in the apparatus before reaching the detector. This multiple-scattering intensity has to be evaluated. The scattered intensity has to be normalized with respect to the intensity or spectrum of the incoming beam. Then the scattered beam intensity has to be corrected for polarization effects, sample absorption, and normalized with respect to the number of atoms in the sample. The properly normalized structure function is obtained only after these laborious steps. Any imperfection in the corrections procedure will affect the outcome.

This sounds complicated and arduous, but there is good news. First, most of the corrections are pretty well understood and can be reliably estimated. They are now implemented in a number of computer programs as we describe later. The second piece of good news is that the structural information in the PDF is fairly robust with respect to analysis errors. The reason is that most data corrections give rise to data modulations that are much more slowly varying with Q than the experimental signal itself. The net result of this is that imperfections in the data correction procedure have a large effect on the very low-r region of the PDF, as long-wavelength features in $S(Q)$ give rise to sharp features in $G(r)$ at low-r. This is the region below the nearest-neighbor distance where there is no physical information about the structure. While accurate data corrections are clearly important, the physical information in the PDF is somewhat robust to imperfect corrections. This fact has long been used to make cosmetic corrections to PDFs, mostly in the field of amorphous materials, by back-transforming the low-r ripples below the nearest-neighbor peak and subtracting this transform from the data and then retransforming the data. The ugly ripples in the low-r region are removed. However, recently, it has been demonstrated that this can be taken to the next level. Enough is known about the asymptotic behavior of the $S(Q)$, $F(Q)$, and $G(r)$ functions, and the nature of the corrections (Peterson *et al.*, 2003), that raw data can be converted to reliable PDFs using a completely *ad hoc* correction process (Billinge and Farrow, 2012; Juhas *et al.*, 2012). This has been implemented in a computer program, PDFgetX3 (Juhas *et al.*, 2012). For rapid acquisition PDF data from 2D area detectors and from laboratory X-ray setups, the *ad hoc* method produced PDFs that were identical to those obtained using the full corrections implemented in PDFgetX2, modulo a scale factor (Qiu *et al.*, 2004). Using this approach, PDFs are obtained from raw data in milliseconds on a laptop computer and tuning of data reduction parameters such as background scale, and Q_{max} can be varied in real time while observing the effect on the PDF. This approach may not be adopted by people studying amorphous and liquid samples where the goal is to obtain a highly accurate

sample scattering cross section. However, for nanoparticles and nanostructure in crystals, the primary focus of this book, where there is ample structural information in the PDF which is extracted by fitting models, this *ad hoc* approach is proving to be very powerful and reduces a significant barrier to entry into the field: the complicated data reduction process described in this chapter!

Having said this, spurious information from this low-r portion of the PDF can propagate into the physical region of the data and one should be guarded against overinterpreting small, individual, features, especially in the low-r region of the PDF. On the plus side, in contrast to other local structural techniques such as EXAFS, the quality of the data does not diminish with increasing r. By fitting models over a range of r to get the structural information, it is unlikely that experimental artifacts will be wrongly interpreted.

In this chapter, we discuss in detail the equations and procedures used to correct the data to obtain $S(Q)$ and subsequently $G(r)$. We develop the equations for the data analysis using the language of differential cross sections. This formalism will be much more familiar to neutron scatterers than X-ray scatterers; however, as defined, it is completely universal. It is also a very intuitive way to describe the real physical measurement, and for those unfamiliar with the slightly mathematical looking formalism, a few moments spent understanding the definition (Section A5.1.1 of Appendix 5.1) in detail will pay back handsomely. The desired structure function, $S(Q)$, depends on the coherent single-scattering sample cross section, $(\mathrm{d}\sigma^s/\mathrm{d}\Omega)$, from Eq. (2.8):

$$S(Q) = \frac{1}{\langle b \rangle^2} \left(\frac{\mathrm{d}\sigma^s}{\mathrm{d}\Omega} \right) + \left(\frac{\langle b \rangle^2 - \langle b^2 \rangle}{\langle b \rangle^2} \right). \tag{5.1}$$

For many PDF users, it is not necessary to understand in detail each of the data corrections, their origin, and application but good enough simply to use the excellent data reduction computer programs that are now available. Indeed, on a first reading of this book, it is probably recommended to skip to Section 5.4.1 where we describe how to get started with data analysis by downloading the programs for doing this. However, we leave a detailed description of the data corrections, and it is well worth spending the time to go through them at some point to better understand and control your future PDF experiments and to get the most from your data. In Section 5.2, we give general equations for $(\mathrm{d}\sigma^s/\mathrm{d}\Omega)$ in terms of the measured intensities from sample and background datasets. These equations are derived in an intuitive step-by-step fashion in Appendix 5.1. We also lay out the theory for the *ad hoc* correction methodology. In Section 5.3, we discuss specific corrections for X-ray and tof neutron data and present the equations that are relevant for these specific cases. In Section 5.4, some aspects of real-world data analysis, including where to get data analysis programs, are laid out.

5.2.   DATA ANALYSIS OVERVIEW

In this section, we give the most general equations that are necessary to reduce raw data to the total scattering structure function $S(Q)$. As per Eq. (5.1), this requires determining $(d\sigma^s/d\Omega)$ from the experimentally measured intensities. The equations given here are systematically defined in Appendix 5.1. The derivation is involved and can be skipped on a first reading. However, we believe that glancing over the derivation steps reveals considerable insight into the philosophy of the data corrections and is well worth the effort.

The problem is set up initially in the most general terms possible by dividing the sample into microscopic volume elements and considering the scattering from each element in turn. There is more than one approach that can be taken to obtain $S(Q)$ from the raw data. Also, exactly which equations are used to make specific corrections depends on the geometry of the particular measurement. By developing the problem in general terms first, we hope that it becomes clear to the reader exactly what problems are being faced by the data analyst. For convenience, the resulting equations are reproduced below from Appendix 5.1.

In general, to obtain a reliable $S(Q)$, three measurements need to be made: sample in a can in its sample environment, empty can in the sample environment, empty environment (sometimes called background). In the equations below, the letters s, c and a are used to denote the presence of sample, container, and sample environment (or apparatus), respectively, in the measurement. People sometimes wonder what is the difference between the sample container, measurement, and the empty environment, or background, since is not the sample container a background? The reason for the distinct measurements is illustrated in Appendix A5.1.2 and Fig. A5.1.3 in that section. The difference is that the container is close to the sample and it is assumed that the other background resides some distance away from the sample. Most of the particles that scatter off the container and reach the detector have to traverse the sample on their journey to or from the scattering point. When we measure the empty container, we get the scattering signal from the container but it is not attenuated by the absorption of the beam as it traverses the sample. Consequently, before subtracting the container scattering, it is corrected for absorption effects due to the presence of the sample. This is not true for the background signal where, predominantly, the scattered particles do not traverse the sample on the way to the detector. In many cases, it is not necessary to measure separate container and background datasets, for example, if the backgrounds are very low (the most desirable case!) or the sample absorption is low, which appears to hold quite true for many RAPDF measurements with high-energy X-rays. In these three experiments, the integrated counts in the detector, N, normalized by the monitor counts, M, are given by Eqs. (A5.1.23)–(A5.1.25)

$$\left(\frac{N}{M}\right)^{\text{sca}} = \mathrm{d}\Omega\mathrm{d}E_s K\varepsilon_\mathrm{d}\{p^{\text{s;sca}} + p^{\text{c;sca}} + p^{\text{a;sca}} + m^{\text{sca}}\}, \tag{5.2}$$

$$\left(\frac{N}{M}\right)^{\text{ca}} = \mathrm{d}\Omega\mathrm{d}E_s K\varepsilon_\mathrm{d}\{p^{\text{c;ca}} + p^{\text{a;ca}} + m^{\text{ca}}\}, \tag{5.3}$$

$$\left(\frac{N}{M}\right)^{\text{a}} = \mathrm{d}\Omega\mathrm{d}E_s K\varepsilon_\mathrm{d}\{p^{\text{a;a}} + m^{\text{a}}\}, \tag{5.4}$$

where all the symbols are defined in Appendix 5.1. Here, the single-scattering contributions are given by Eq. (A5.1.18),

$$p^{y;\{w\}} = \left(\frac{\mathrm{d}^2\sigma^y}{\mathrm{d}\Omega\mathrm{d}E_s}\right)\rho^y D\int_y h\left(\prod_{x\in\{w\}} A_x\right)\mathrm{d}\mathbf{r}, \tag{5.5}$$

and m^{xyz} are the multiple-scattering terms defined in Appendix 5.1. By making certain approximations, these equations can be combined and rearranged to yield Eq. (A5.1.36)

$$\left(\frac{\mathrm{d}^2\sigma^s}{\mathrm{d}\Omega\mathrm{d}E_s}\right) = \left[\left(\frac{N}{M}\right)^{\text{sc}} - \left(\frac{V'_{\text{c;sca}}}{V'_{\text{c;ca}}}\right)\left(\frac{N}{M}\right)^{\text{c}}\right]\left(\frac{1}{\rho^s V'_{\text{s;sca}} D\mathrm{d}\Omega\mathrm{d}E_s K\varepsilon_\mathrm{d}}\right) - m' \tag{5.6}$$

for the sample double-differential cross section (Appendix 5.1) where

$$\left(\frac{N}{M}\right)^{\text{sc}} = \left(\frac{N}{M}\right)^{\text{sca}} - \left(\frac{N}{M}\right)^{\text{a}}$$

and

$$\left(\frac{N}{M}\right)^{\text{c}} = \left(\frac{N}{M}\right)^{\text{ca}} - \left(\frac{N}{M}\right)^{\text{a}}.$$

From here, it is a straightforward integration over the energy window of the measurement, $W(E)$, to obtain an expression for the desired single-scattering cross section in terms of the measured counts (Eq. A5.1.37),

$$\left(\frac{\mathrm{d}\sigma^s}{\mathrm{d}\Omega}\right) = \int\left(\frac{\mathrm{d}^2\sigma^s}{\mathrm{d}\Omega\mathrm{d}E_s}\right)W(E_s)\mathrm{d}E_s, \tag{5.7}$$

$$= \left[\left(\frac{N}{M}\right)^{\text{sc}} - \left(\frac{V'_{\text{c;sca}}}{V'_{\text{c;ca}}}\right)\left(\frac{N}{M}\right)^{\text{c}}\right]\left(\frac{1}{\rho^s V'_{\text{s;sca}} D\mathrm{d}\Omega K\varepsilon_\mathrm{d}}\right) - m'. \tag{5.8}$$

In this equation, the $V'_{y;\{w\}}$ terms give the absorption weighted "effective scattering volume" of the sample. They are discussed further in Section 5.3.6 and defined in detail in Appendix 5.1. They can be evaluated numerically knowing the linear absorption coefficients, $\mu(E)$, of the sample, container and apparatus.

For some simple geometries, such as flat-plate transmission and reflection, there are analytic expressions which are derived in Appendix 5.2.

Within the assumptions we have made, this equation for $(d\sigma^s/d\Omega)$ is quite general. We have not assumed any particular origin for the double-differential cross section. We have not presumed that the scattering is elastic or inelastic or coherent or incoherent, nor have we stipulated that the measurement be made at constant wavelength, or in a particular geometry. We have not even specified that the scatterers be X-rays, electrons, or neutrons. Eq. (5.8) is valid, provided the scattering is weak, that the experimental apparatus other than the sample container is sufficiently far from the sample, that each component of the experimental apparatus, and the sample, is homogeneous, and that we can evaluate the multiple-scattering contributions adequately. Clearly, an accurate determination of the sample cross section also implies that we can evaluate the integrals, $V'_{y:\{w\}}$, accurately and that we know, or can measure, our sample density, detector solid angle, and detector efficiencies. These issues will be dealt with below.

Finally, as we discussed at the beginning of the chapter, $S(Q)$ is obtained from $(d\sigma^s/d\Omega)$ according to Eq. (5.1).

5.2.1.　Quantitatively Reliable PDFs Using *Ad Hoc* Data Corrections

We know a lot about the asymptotic behavior of the total scattering functions $S(Q)$, $F(Q)$, and $G(r)$, and this allows us to assess the quality of resulting PDFs after carrying out the data corrections (Peterson *et al.*, 2003). We also know a great deal about the nature of most of the experimental effects that affect the measured functions, as described in this chapter. The question is whether this known information provides sufficient constraints to allow us to find the right form for correction terms in an *ad hoc* way without distorting the resulting structural information. The protocol is described here and has been implemented in a program, PDFgetX3. We also demonstrate in this section that, for the cases tried, the *ad hoc* corrections give essentially identical results to those obtained with PDFgetX2, which explicitly makes all the corrections using the methods described in the rest of this chapter.

We seek the reduced structure function $F(Q)$, from a sample, given the total measured powder diffraction intensity, $I_T(Q)$ as laid out in Equation (2.1). Now $F(Q)$ comes from $S(Q)$ which comes from I_c, the coherent scattering intensity. Apart from the detector dead-time correction, all the corrections and normalizations that take us from I_T to $F(Q)$ are either simply additive or multiplicative. If we assume that any detector dead time is negligible, or has been corrected before getting I_T, we can write the equation for $F(Q)$ in a completely general form:

$$F(Q) = \alpha(Q)I_T(Q) + \beta(Q), \qquad (5.9)$$

where α and β are unknown Q-dependent functions that contain *all* of the relevant corrections described in this chapter (and any others not described here too!). If we can determine $\alpha(Q)$ and $\beta(Q)$, we can apply this equation to obtain an accurate $F(Q)$.

How do we go about determining α and β? We know that there is a good separation between the frequency of most corrections and the frequency of the structural information in the PDF. The lowest frequency Fourier component in $F(Q)$ coming from a real structural signal is $\sim 2\pi/r_{nn}$, where r_{nn} is the length of the shortest interatomic bond length. This means that all *additive* frequency components in the signal that have lower frequency than this are certainly coming from nonstructural contributions to the signal. On the other hand, the additive contributions to the signal coming from extrinsic sources are predominantly much longer wavelength and more slowly varying than this. Examples are Compton scattering and multiple-scattering intensities, both of which vary very slowly with Q. If we assume that all the multiplicative corrections have been carried out sufficiently well (we will return to this point later), it remains to determine $\beta(Q)$. Provided we explicitly subtract any corrections that contain frequency components higher than $2\pi/r_{nn}$, there is then a clean separation in frequency between the signal and the corrections and we can effectively Fourier filter the data to remove all the corrections. Another approach is to fit an arbitrary function to $I_{\mathrm{T}}(Q)$ where we constrain this function to have no frequencies higher than $2\pi/r_{nn}$, then subtract this function. It turns out that the assumptions laid out here usually hold rather well in practice, except for the signal from the sample container which does contain high-frequency components. However, it is usually rather straightforward to measure an empty container and subtract it explicitly.

Let us now turn our attention to the multiplicative correction term, $\alpha(Q)$. We know from the convolution theorem that the Fourier-transform of the product of two functions is the convolution of their Fourier-transforms. An imperfectly accounted for $\alpha(Q)$ in Eq. (5.9) will result in a multiplicative aberration to $F(Q)$, that is,

$$F'(Q) = \alpha'(Q)F(Q), \tag{5.10}$$

and if we Fourier transform $F'(Q)$, the real sample PDF will be convoluted with the Fourier transform of $\alpha'(Q)$. Convolutions always broaden functions, which suggest that there may be a variational approach to finding $\alpha'(Q)$ where an *ad hoc* $\alpha'(Q)$ is parameterized and the parameters varied in such a way as to minimize the width of peaks in the PDF (Billinge *et al*., 2011, Billinge and Farrow, 2012).

To see how this might work, let us consider a simple case of a PDF containing a single peak (e.g., the PDF of O_2 or N_2) at position r_v originating from two atoms with unitary scattering power (so, we can neglect the form-factors in the equations). The $F(Q)$ of this PDF is

$$F_v(Q) = \frac{\sin r_v Q}{r_v}. \tag{5.11}$$

Now, we can make a cosine Fourier expansion of $\alpha'(Q)$ (since the sine terms will not affect $G(r)$) (Billinge and Farrow, 2012)

$$\alpha'(Q) = \frac{\alpha_0}{2} + \sum_{n=1}^{\infty} \alpha_n \cos\left(n r'_0 Q\right). \tag{5.12}$$

Here, the a_n's are the Fourier coefficients and r'_0 is a very small distance, much shorter than the shortest physical distance in the problem. For our simple example, assume that over the Q-range of interest the aberration $\alpha'(Q)$ is well explained by a cosine function of some wavelength, let us say the jth term in the Fourier expansion. In this case, Eq. (5.10) becomes

$$F_v(Q) = \alpha_j \cos\left(j r'_0 Q\right) \frac{\sin\left(r_v Q\right)}{r_v}, \tag{5.13}$$

which, using trigonometric identities, can be put into the same form as Eq. (5.11), that is,

$$F_v(Q) = \frac{\alpha_j}{2}\left(1 + \frac{j r'_0}{r_v}\right) \frac{\sin\left(r_v + j r'_0\right)Q}{\left(r_v + j r'_0\right)} + \frac{2\left(1 - \frac{j r'_0}{r_v}\right)\sin\left(r_v + j r'_0\right)Q}{\left(r_v + j r'_0\right)}. \tag{5.14}$$

How do we understand this new equation? We see that the single peak in the PDF from before has been replaced by two peaks, each of approximately half the amplitude, located at positions $(r_v + j r'_0)$ and $(r_v - j r'_0)$, that is, shifted to the left and to the right of the position of the original peak by distance $j r'_0$. However, we know that the aberration, $\alpha'(Q)$, is much more slowly varying than the structural signal, which means that $j r'_0 = r_v$. Thus, these two peaks in the PDF will be very close together, with the splitting being less than the intrinsic width of the PDF peak. They will appear as a single peak that has been slightly broadened from the original. The prefactors in Eq. (5.14) also have an effect of skewing this peak a little bit, as the two shifted peaks are not exactly equal to half the intensity of the original peak. However, the skewness will be small since $j r'_0 / r_v$ is very small.

It may be possible to find an *ad hoc* approach to estimate $\alpha'(Q)$ by varying Fourier coefficients in its expansion in such a way as to get the sharpest peaks possible in the resulting PDF. A limitation of this approach becomes quickly evident which is that there are slowly varying multiplicative corrections that are intrinsic to the sample and not aberrations. We already use one of these to sharpen the PDF when we divide by the Q-dependence of the atomic form-factors in the X-ray and electron cases. The other sample-dependent multiplicative factor is more tricky because it is unknown *a priori*; it is the Debye–Waller factor. The *ad hoc* approach we describe here would not only correct the multiplicative aberrations but also eliminate a global

Debye–Waller factor, though differences in Debye–Waller factor from different atoms would survive since it would require Fourier components with frequencies in the structural domain to eliminate intensities from selected Bragg-peaks. This may be addressed in various ways, for example, on the basis that factors such as absorption do not change much with temperature, $\alpha'(Q)$ may be determined for a low-T dataset and fixed as temperature is varied, so the change in the global Debye–Waller factor with temperature is retained.

Despite the question marks surrounding the correct implementation of the multiplicative correction, a program has been written, PDFgetX3, that implements the *ad hoc* method (Juhas *et al.*, 2012). It produces PDFs very rapidly (in milliseconds on a laptop) with little user input or training. On the basis that for X-ray data collected in the rapid acquisition PDF (RAPDF) mode with high-incident X-ray energies the absorption is weak, $\alpha'(Q)$ was set to unity in the first implementation. The resulting PDFs obtained from trial datasets were then benchmarked against the best PDFs that could be obtained using PDFgetX2 (Qiu *et al.*, 2004). After visual comparison between the PDFs obtained by the two approaches, structural models were fit to the PDFs to see if the same structural values were refined for structural parameters. These tests were very successful. Example plots that show this comparison are presented in Fig. 5.1. In the structurally relevant region, the PDFs are equivalent (Juhas *et al.*, 2012). The *ad hoc* data corrections therefore look highly promising and are likely to become of increased importance in the future, at least for crystalline and nanoparticle studies where an absolute normalization (scale factor equals one) is not required.

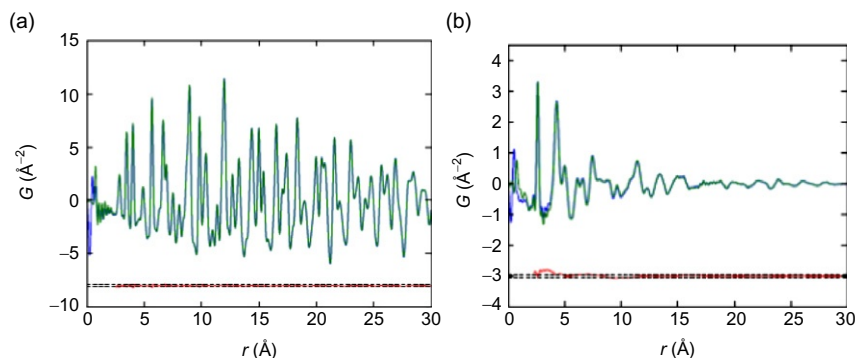**FIGURE 5.1** X-ray PDFs of (left) BaTiO$_3$ and (right) 3.7 nm diameter CdSe nanoparticles showing the comparison of PDFs obtained using the full corrections in PDFgetX2 and using the *ad hoc* approach implemented in PDFgetX3. Offset below is the difference curve. Clearly for these RAPDF data, the two approaches give equivalent PDFs in the region of structural interest (Juhas *et al.*, 2012).

5.3.   OBTAINING $S(Q)$ IN PRACTICE

We will now discuss how to obtain the total scattering structure function, $S(Q)$, in practice in three specific cases: angle dispersive X-ray diffraction, including RAPDF method, tof neutron diffraction, and electron diffraction. It is possible to obtain good PDFs from reactor neutron sources using a constant wavelength angular dispersive mode as well, although except when using a very hot moderator such as the D4 instrument at the Institut Laue Langevin in Grenoble, the Q range is very limited. In this case, the data corrections are much closer to those used for X-ray analysis than the tof data collections, the main difference being that the form-factor is Q-independent, and there are no polarization corrections to be carried out. These corrections are not explicitly discussed here but are implemented in Gudrun, for example.

Up to now, we have defined the sample cross section in a very general way. We did not say that it was only coherent scattering nor did we even specify the scattering mechanism. The cross section was simply the probability that a particle is scattered by a given volume element in a given direction, by any process. In this section, we will explore this in more detail taking the case of X-ray and neutron scattering separately. Before we do this, we will summarize some of the terminology.

5.3.1.   Elastic, Inelastic, Coherent, and Incoherent Scattering

All scatterings can be characterized using two important concepts into four distinct categories. The two concepts are whether the scattering was elastic or inelastic and whether it was coherent or incoherent. These terms are often used imprecisely leading to confusion. This is particularly apparent when a person with a neutron scattering background talks to a person with an X-ray scattering background where the concept of inelastic scattering generally has a very different meaning. We discuss this further here. First we define the terms, the easier to define first. In an elastic scattering event, there is no exchange of energy between the scattering particle and the system it is scattering off (the sample). Conversely, in an inelastic scattering event, there is an exchange of energy. The coherence of the scattering refers to whether there is a definite phase relationship between scattered waves allowing them to interfere constructively and destructively. In the case of coherent scattering, the waves interfere and the resulting intensity is given by the square of the sum of the wave amplitudes. For example, if there are two scattered waves of amplitude ψ_1 and ψ_2, then $I = |\psi_1 + \psi_2|^2$. In the case of incoherent scattering, there is no definite phase relationship between the waves, they do not interfere, and the resulting intensity is simply the sum of the intensities of the individual waves themselves, that is, $I = |\psi_1|^2 + |\psi_2|^2$. Since structural information in the scattering comes from the interference effects of scattered

waves, it is clear that only coherent scattering contains any structural information.

There are many different scattering processes that occur in materials, but all scattering processes can be categorized as being coherent or incoherent and elastic or inelastic. To illustrate this, we mention some types of scattering and categorize them. We will discuss this more below in the Sections 5.3.7 and 5.3.8. Bragg scattering is elastic and coherent. Laue monotonic diffuse scattering (coming from the mixture or different chemical species in a sample) is elastic and incoherent. The incoherent cross section of the nuclear scattering, coming from the different isotopes and spin states of nuclei in a sample, is elastic and incoherent (in some sense, it is the same as Laue monotonic scattering). Thermal diffuse scattering is inelastic and coherent. Compton scattering is inelastic and incoherent. Neutron (and X-ray) scattering from phonons and magnons is inelastic and coherent (actually the same origin as thermal diffuse scattering). All the coherent scattering, elastic (e.g., Bragg) and inelastic (e.g., TDS), becomes incoherent at high enough values of Q due to Debye–Waller effects. We will use these concepts more below.

5.3.2. Real-Time PDFs

In recent history (and probably throughout the history of the method), the data collection and data analysis steps were carried out at different times. Data collection is often a sprint, carried out over a few hectic days of user beam time at an X-ray or neutron user facility. The goal is to g*et al*l of the datasets required to complete the research in the allotted time. Focus is on setting up the experiment and collecting datasets. If there is enough help at the experiment, it is possible for someone to be processing data on the fly to get preliminary results and ensure data quality, but these efforts rarely keep track with the data rates. There are two significant disadvantages of this approach. The most obvious is that you may get home and find that the data are compromised in some way when you process them and find them unusable. The second problem is that it is very difficult to change the direction of the experiment as it is taking place: the measurement that you do is the measurement that you planned ahead of time. After analyzing the data and finding an interesting unexpected phase transition, for example, it is too late to go back and do anything about it until the next beam time. With this in mind, there are a number of efforts afoot to automate the data reduction process to a much greater extent than is the current norm. For a number of years, a setup at the NPDF diffractometer at the Lujan Center at Los Alamos has allowed PDFs to be determined in real time as the data come in, with a very friendly user interface associated with it, and this is a very popular feature with users. This works well for NPDF where datasets typically take from half an hour to a few hours per dataset. The most common X-ray data collection mode is now the RAPDF mode where datasets take between a few tens of milliseconds and

a few minutes each. As we describe below, the data analysis involves a number of steps making it somewhat hard to set up real-time processing, but scripts to do this that tie together the different steps of the processing are in the works. We hope that in the near future, PDF beam lines carrying out RAPDF experiments will also be able to deliver real-time PDFs so researchers are no long "flying blind" in their PDF experimentation. However, it is fair to say that, at the time of writing, this is still in its infancy.

5.3.3.   Detector Dark Counts and Dead-time Corrections

Counts are detected even when the X-ray beam is switched off. These are known as dark counts and come from thermally excited events in the detector and noise in the electronics. Detectors are designed to minimize the dark counts, for example, by cooling. Nonetheless, the dark count rate of the experimental detector and electronics setup should be measured by determining the detected counts with the electronics live, but the X-rays switched off. To ensure long-time stability in the detector/electronics setup, it is good practice to repeat the dark count measurement periodically throughout the experiment. This is especially true for the modern generation of amorphous silicon or CCD technology 2D X-ray detectors such as manufactured by General Electric and Perkin Elmer and the ESRF Frelon detector. In these cases, frames are collected in dark/light pairs. The measured dark count-rate should be subtracted from the data first, before proceeding further with data analysis.

For photon-counting detectors such as solid-state detectors, proportional counters, and strip detectors (but not for integrating detectors such as image-plate detectors), every time an X-ray or a neutron is detected, the detector and its associated electronic circuits have to reset before another event can be detected. This takes some time called the dead time. As the count-rate increases, the probability that a second neutron will arrive during this dead period, and therefore not be counted, increases. There is, therefore, a count-rate-dependent correction to be made to the observed total counts. This effect is distinct from the quantum efficiency of the detectors, ε_d and ε_m, because it is an additive correction to the detected counts that depends on the total count-rate into the detector. The quantum efficiency is simply a multiplicative correction: it says that if a particle impinges on the live detector, it will be detected with the probability $1/\varepsilon_d(E_s)$. To get the total number of particles incident on the detector, you take the measured counts and divide by ε_d. The detector dead time was not specifically taken into account in the discussion of general data corrections. This correction should be applied before proceeding with any other corrections.

Provided the dead time is of the order of a few percent, it can be effectively be corrected using the standard formula for dead-time correction,

$$N' = \frac{N}{1 - R_d \tau_d}, \qquad (5.15)$$

where N are the measured counts and τ_d is the time the detector takes to reset: the detector dead time. R_d is the count-rate (counts per second) in the entire detector. This includes all the particles incident on the detector and not just those that are saved after discrimination. This equation has to be modified in certain circumstances. For example, in tof measurements, the count-rate in one time-channel can affect the dead time in a neighboring time-channel if the detector dead time is comparable to the channel width. This complication was discussed by Soper *et al.* (1989) and is presented briefly in Section 5.3.8.4. It is even more complicated in the current generation of detector banks with multiple pixels that may be multiplexed so that more than one pixel feeds the same photomultiplier tube, as is the case at the GEM diffractometer at ISIS for instance. The detector dead time, τ_d, can be measured, for example, by attenuating the beam systematically with foils of known attenuation coefficient. The resulting curve can be fit by Eq. (5.15) to obtain τ_d.

There are alternative methods for assessing detector dead times. For example, the charge pulses output from an electronic pulser may be fed into the pre-amp of the detector. This pulser produces charge pulses at a known rate, either at random or regular time intervals. The charge pulses propagate through the detector electronics and are recorded on a scalar or in the MCA. The integrated charge in the charge pulses can be adjusted so that the pulser counts appear at a quiet part of the X-ray energy spectrum and do not interfere with real data. The ratio of detected pulses to the known total number of pulses (pulse-rate $\times$ count-time) therefore yields an instantaneous estimate of the dead time. Clearly, this will be accurate only if the dead time is dominated by the detection and acquisition electronics and not the time it takes to extract the charge from the detector itself. This method of estimating dead time also introduces noise into the data unless the signal from the pulser is smoothed. Another method is to compare the elapsed time and the live time of the multichannel analyzer electronics, should one be used; a piece of information which is sometimes available depending on the MCA. This only gives an accurate estimate of the dead time due to the MCA conversion.

An example of the importance of accurately correcting for dead time is shown in Fig. 5.2. These are synchrotron X-ray data shown before and after a dead-time correction. Discontinuities in nondead-time-corrected intensities occur at synchrotron beam fills when the incident intensity, and therefore count-rate into the detector, suddenly takes a significant jump. A big advantage of the new RAPDF style of experiment is that the complete dataset is collected in parallel, rather than point by point, avoiding such issues.

In the case of the figure, an incident beam attenuator was removed in the middle of the experiment accounting for the change in intensity and the discontinuity. Not only the poor overlap but also the amplitude of features in the
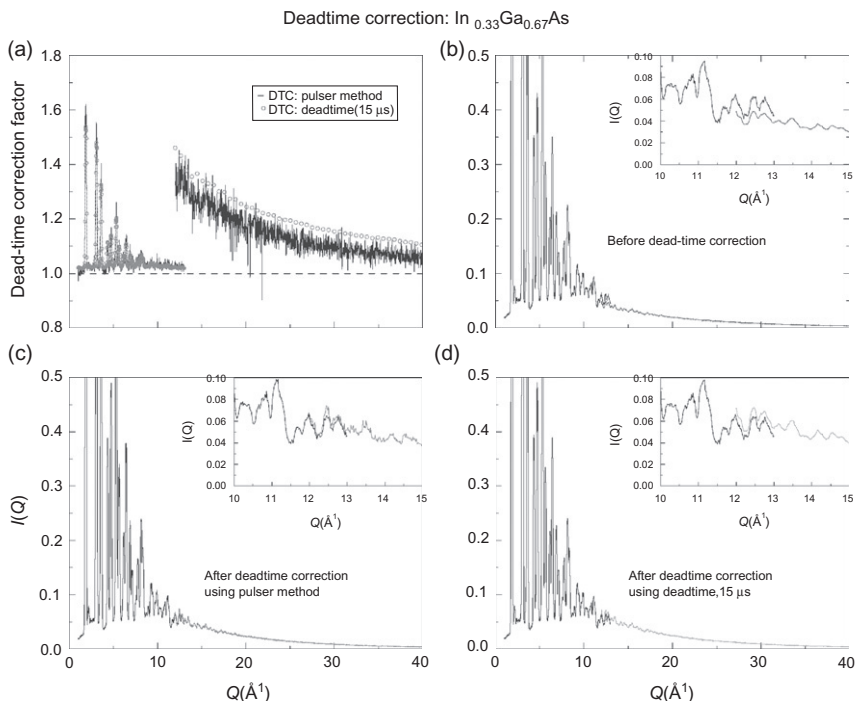
Deadtime correction: In$_{0.33}$Ga$_{0.67}$As

FIGURE 5.2   Comparison of raw and dead-time-corrected data from the CHESS high-energy synchrotron source. The data are from the high-Q region from a sample of GaAs. The data have been normalized for incident flux. The sharp discontinuities coincide with points in time when the synchrotron ring was refilled or attenuators were removed from the beam and the source intensity discontinuously increased. After carrying out the dead-time-correction, the discontinuities are not apparent (PDFgetX manual).

overlap region are only preserved after the dead-time correction (inset to Fig. 5.2b–d). The factor by which the data had to be scaled to account for the detector dead time is shown in Fig. 5.2a determined both using the analytic method (Eq. (5.15) and $\tau_{\mathrm{d}} = 15\,\mu\text{s}$) and using the pulser method. The pulser method results in a slightly better correction but introduces unwanted noise into the data. The region of overlap is collected to ensure that this correction works well, as is evident. Clearly, the effects of dead time are less (but not necessarily negligible) in low-intensity situations such as laboratory X-ray sources and many neutron experiments.

5.3.4.   Propagating Random Errors

A scattering experiment involves estimating an underlying scattering cross section by sending well-characterized scattering particles into the sample

and detecting the scattering pattern. As with all such stochastic measurements, the resulting intensity distribution is just an estimate of the underlying scattering probability. As the scattering process is completely random, this process obeys Poisson statistics (e.g., see Prince, 1982). An estimate of the uncertainty of this measurement is therefore obtained by taking the square root of the number of counts. Thus, if N' particles (photons, neutrons, or electrons) are detected, the uncertainty in this measurement is $\sqrt{N'}$. Note that the standard deviation of the counts is given by the square root of the dark-current and dead-time-corrected counts not the raw counts. The detector dead time makes the scattering/detecting process nonrandom by introducing correlations between events. As a result, the detector dead-time-corrected counts rather than the raw counts are Poissonian.

As we have seen above, many data corrections are carried out before $S(Q)$ is deduced. We would like to propagate the known uncertainties due to the random counting statistics through to the final $S(Q)$. This can be done with a high degree of certainty using standard error propagation procedures (Prince, 1982). This was discussed briefly in Section 3.5.3. The mechanics of error propagation, and some aspects pertinent to the PDF, are discussed in detail in Appendix 5.3. For now, it is sufficient to note that error arrays that will be propagated through the data analysis with the data arrays should be created at this point, after the detector dead-time correction has been applied but before the data are normalized by the monitor counts and any subsequent corrections are applied. At each step, when the data arrays get modified by sample corrections, the error arrays are correspondingly modified according to the principles laid out in Appendix 5.3.

5.3.4.1. Data Collection Strategy for Optimizing the Statistics on G(r)

Note that because the coherent scattering signal diminishes with increasing Q, the signal-to-noise ratio is poorest at high-Q. Thus, this is the region of the diffraction pattern where the most time should be spent in collecting the data. The effect can be dramatic in the case of X-rays as we describe below. We are interested in optimizing the statistical errors on $G(r)$. This has been discussed by Thijsse (1984) for the case of a constant source intensity where he minimizes the expression for var($G(r)$) (Eq. A5.3.9) using calculus of variations with the constraint of a fixed total counting time, T. The result indicates, given a fixed amount of time for the experiment, how much time should be spent on each point. The result is not exactly equal to, though similar (Thijsse, 1984) to, the case of giving equal statistical significance to every point in $S(Q)$ in the Fourier transform. Starting with Eq. (A5.3.9), we see that this amounts to ensuring that $Q_i^2 \Delta Q_i^2 var(S(Q_i))$ is approximately constant in Q. For the case of X-ray scattering, where we have some control over this, we can assume that ΔQ_i^2 is constant and

$$\text{var}(S(Q_i)) = \left(\frac{1}{\langle f(Q)\rangle^4}\right)\text{var}(I^{\text{coh}}) \approx \left(\frac{1}{\langle f(Q)\rangle^4}\right)\text{var}\left(\frac{N}{M}\right),$$

where we neglect all the absorption and multiple-scattering corrections, etc., to N/M. The approximation is much better in high-Q experiments if the Compton scattering is discriminated away and the N/M only in the elastic channel is considered. The variance of N/M is

$$\text{var}\left(\frac{N}{M}\right) = \frac{N}{M^2}\left(1+\frac{N}{M}\right),$$

or, in a well-designed experiment where the monitor counts are much higher than the signal counts,

$$\text{var}\left(\frac{N}{M}\right) \approx \frac{N}{M^2} \approx \frac{\langle f^2(Q)\rangle}{M}.$$

Thus, for every measured point to contribute equally to the Fourier transform, we need to approximately satisfy the condition $M(Q_i) \propto Q_i^2/\langle f^2(Q_i)\rangle$. For very high-$Q$ experiments, this is a demanding criterion. $\langle f^2(Q)\rangle$ falls smoothly from a value of Z^2 at $Q=0$ to a value of order unity at very high-Q. For a Q of $40\ \text{Å}^{-1}$, the counting time at high-Q could be as much as 5 orders of magnitude higher than at low-Q!

The calculus of variations method (Thijsse, 1984) results in the less demanding criterion of $M(Q_i) \propto Q_i/\langle f(Q_i)\rangle$, but still the monitor counts at $Q \sim \text{Å}^{-1}$ should be 2–3 orders of magnitude higher than at $Q \sim \text{Å}^{-1}$. If these criteria are not adhered to, a perfectly valid $G(r)$ is still obtained, but not with optimal statistics. Also, information in $S(Q)$ about small atomic displacements is strongest at high-Q (its intensity scales approximately like $Q^2 \delta r^2$), so it is important to collect the high-Q data with good statistics.

5.3.5. Flux Normalization

When data are collected in a point-by-point fashion, it is important to account for changes in incident flux for each point. This correction is not required for RAPDF data where the entire dataset is collected in parallel and so changes in intensity of the incident beam affect every point in $S(Q)$ the same, yet another advantage of this approach.

For very stable sources such as sealed tube sources, the measurement time can be used to scale data points, provided the primary and secondary beam slits remain unchanged. However, in general, as described in Chapter 4, the incident flux is measured using an incident beam monitor. In this case, the data points are simply divided by the monitor as indicated in Eqs. (5.23)–(5.25) and the flux normalization is a simple division of the (dead-time corrected) detector counts, N', by the (dead-time corrected) monitor counts, M'. In the case of an

angle dispersive monochromatic synchrotron measurement, the incident flux decays with time as the synchrotron beam current decays, with periodic refills where the flux recovers.

In the case of a tof neutron measurement, the flux is strongly energy dependent and the data must be divided by the source spectrum. This consists of a Maxwellian peaked at the temperature of the moderator with an exponential tail on the low-λ, high-E, side due to undermoderated epithermal neutrons. This is shown in Fig. 4.5. An empirical expression has been proposed to explain the spectral shape (Howells, 1984)

$$\phi(\lambda) = \phi_{max} \frac{\lambda_T^4}{\lambda^5} \exp\left\{-\left(\frac{\lambda_T}{\lambda}\right)^2\right\} + \frac{\phi_{epi}}{\lambda^{1+2a}} \frac{1}{1 + \exp\{(\lambda - \lambda_1)/\lambda_2\}}, \quad (5.16)$$

where ϕ_{max}, ϕ_{epi}, λ_T, λ_1, λ_2, and a are fitting parameters. The spectrum is measured with high accuracy by using an almost incoherent scatterer such as vanadium, or a completely incoherent (null-scattering) alloy such as V-Nb. The scattering from this simply reflects the source spectrum, and dividing the data point by point by the vanadium data results in a proper flux normalization. This has the additional advantage that detector efficiencies, solid angles, and the detector profile, D, are automatically corrected since the same detectors are used to collect the sample and vanadium data. In fact, this division is carried out after absorption, and multiple-scattering corrections have been carried out on the sample and vanadium data (Eq. 5.33). Since the shape of the spectrum is accounted for in the measurement of the incoherent scatterer (vanadium), the total monitor counts (integrated over all times of flight) can simply be used to scale a particular dataset. However, to help correct for temporal instabilities in the experimental setup, the sample and vanadium data are often both divided point by point on the time axis by the counts from the vanadium monitor that also reflects the source spectrum. This results in a fairly accurate normalization for the source spectrum that, nonetheless, becomes fully corrected for detector geometry, efficiency, solid angle, and profile by the subsequent division by the vanadium data as described above, though introduces more noise in the data unless the monitor data are smoothed. Note that, because the monitor is upstream of the sample and the detectors downstream, the same λ value occurs at different times of flight, τ, in the monitor and detectors and the monitor spectrum has to be interpolated and the ratio made for neutrons of the same wavelength, not the same τ.

5.3.6.   Absorption and Multiple-Scattering Corrections

The absorption corrections were described in some detail in Appendix 5.1 and are practically the same for X-rays and neutrons. The objective is to evaluate the effective volume integrals $V'_{y;\{w\}}$ laid out in Eq. (A5.1.30). These are integrals of the attenuation factors, A_x, defined in Eq. (A5.1.3), over all

trajectories that beams take through the sample, weighted by the incident beam profile function $h(\mathbf{r})$ (Eq. A5.1.13). To evaluate them correctly, $h(\mathbf{r})$ needs to be known as well as the linear absorption coefficients of the sample. In the single-scattering case, the integrals are over volume elements in the sample; for double-scattering, they are double integrals over all volume elements; and so on.

The beam profile function, $h(\mathbf{r})$, must be evaluated experimentally. For example, this can be done by stretching an incoherently scattering fiber, such as piece of nylon, across the sample position and measuring the intensity. In general, the fiber should be first stretched vertically and systematically translated horizontally and then stretched horizontally and translated vertically. If the experiment has cylindrical symmetry, the horizontal translation is all that is needed. In practice, both making this measurement and correlating the resulting beam profile with the integral over volume elements are nontrivial, and it is common practice to neglect $h(\mathbf{r})$ and assume that the beam is homogeneous without serious detrimental effect on the corrections. In this case, an "effective" beam cross section $A' < A$ is sometimes used in the corrections (Sections A5.1.6) (Soper et al., 1989).

For specific flat-plate geometries, there are analytic expressions for the effective volume integrals as a function of scattering angle. These are derived in Appendix 5.2. Examples of absorption corrections for symmetric flat-plate geometries are shown in Fig. 5.3. For cylindrical, and other more general, sample geometries, the integrals can be evaluated at each scattering angle numerically by dividing the sample into volume elements and evaluating the attenuations due to trajectories to and from each volume element. In this case, it is computationally efficient to take advantage of any symmetries that are present (Paalman and Pings, 1962; Poncett, 1977; Soper and Egelstaff, 1980).

It is helpful to know the attenuation coefficients, $\mu_x(E)$, fairly accurately for sample and sample holder at the energy of interest. These are tabulated for the various elements for X-rays (Wilson, 1995) and neutrons (Bodek et al., 2000) and are now available on the web (e.g., at the US National Institute of Standards and Technology (NIST) website). For flat-plate geometries, it is most accurate to measure the absorption (attenuation) length, $\mu_x(E)t$, of the sample where here t refers to the sample thickness, as described in Chapter 4. If an energy-resolving detector, such as a solid-state detector, is used with an MCA, then $\mu(E)t$, for each MCA channel, is directly determined, though do not destroy the detector with unattenuated direct beam! Because powders are used, the beam spends part of its trajectory traversing the space between grains where it is not attenuated. In this case, the lower powder density, rather than the fully dense material density, should be used when calculating the sample linear absorption coefficient. In tof neutron experiments, the energy dependence of the neutron absorption has to be approximated.
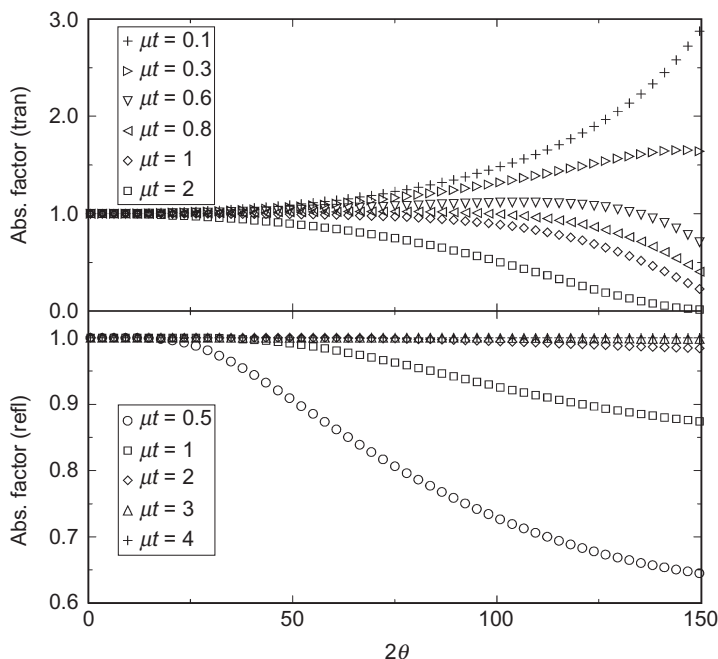
FIGURE 5.3 Calculated absorption factor (defined as the sample effective volume divided by the real volume, V'/V) as a function of scattering angle for symmetric flat-plate geometry. (top) Transmission (bottom) reflection. The curves show the factors calculated for different sample absorption, μt, where a large μt means a highly absorbing sample. The sample effective volume can be greater than the actual sample volume in transmission in the back scattering region. This is because of the long path length the beam takes through the sample. Note the useful property that for an infinitely thick sample (large μt) in reflection geometry, the absorption correction is independent of angle and is simply a constant (PDFgetX manual).

A linear dependence of the absorption cross section with wavelength is assumed: $\sigma^{abs}(\lambda) = \lambda\sigma^{abs}(1)$, where $\sigma^{abs}(1)$ denotes the neutron absorption resonance at $\lambda = 1$ Å (Nield and Keen, 2001). Conventionally, neutron absorption cross sections are reported for neutrons with velocities of 2200 ms^{-1} which is equivalent to $\lambda = 1.798$ Å. This assumption works fairly well except close to neutron absorption resonances. There corrections become more complicated (e.g., see Hannon et al., 1990) with the scattering cross sections, as well as the absorption cross section, having anomalous scattering corrections in exact analogy with the case for X-rays. In general, data in the vicinity of absorption resonances are not used.

These days, the X-ray mass absorption coefficients and neutron absorption cross sections of the elements are often tabulated within data analysis software programs and it suffices to tell the programs the composition of the sample and container and their respective (powder) mass densities.

Multiple-scattering corrections are less straightforward to calculate. They depend on sample thickness and sample transparency and therefore also depend on the sample absorption. As can be seen from Eqs. (A5.1.6) and (A5.1.10), the exact calculation of double and higher order multiple scattering is difficult and requires evaluation of nested integrals. Furthermore, these integrals contain the sample double-differential cross section, precisely the quantity that we are trying to measure. When $S(Q)$ is not highly directional, an approximation can be made that this cross section is isotropic. Another approximation can also be made that higher orders of scattering are just multiples of lower order scattering. This results in a series that converges quickly since each higher order of scattering is significantly weaker than the previous one. Furthermore, it means that only the second-order scattering need to be evaluated explicitly. In this way, the multiple scattering can be straightforwardly, though arduously, calculated (Blech and Averbach, 1965; Dwiggins and Park, 1971; Dwiggins, 1972; Sears, 1975; Serimaa *et al.*, 1990; Warren, 1990). Examples of X-ray double-scattering ratios, I_2/I_1, are shown in Fig. 5.4 for symmetric flat-plate geometries and samples of varying degrees of transparency. Multiple scattering is moderate in low-energy X-ray experiments because of the relatively large sample absorption/scattering ratio. It is a much more significant problem in most neutron measurements where the sample absorption cross section is much less than the scattering cross section.

As can be seen in Fig. 5.4, in the case of X-rays, the multiple-scattering contribution to the intensity is very small in reflection but can be significant in transmission geometry, especially at high-scattering angles. Calculation
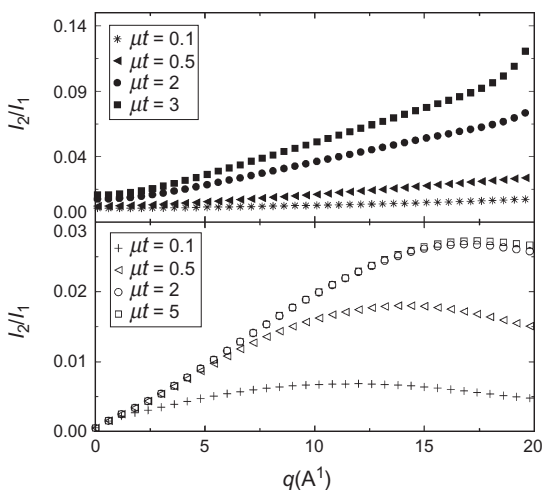

FIGURE 5.4 Calculated double-scattering ratios, I_2/I_1, for symmetric flat-plate geometries and samples of varying degrees of transparency. (top) transmission (bottom) reflection. The double scattering includes elastic and inelastically scattered contributions and was calculated for nickel using X-rays of wavelength $\lambda = 0.7107$ Å (PDFgetX manual).

of the X-ray multiple-scattering intensity is considerably simplified when only purely "elastic" scattering is collected (the Compton scattering is discriminated away) since only completely elastic multiple-scattering events need to be considered.

For crystalline samples, the isotropic approximation is disastrously wrong (the scattering cross section is strongly peaked in the directions of Bragg-peaks!). Nonetheless, the extensive averaging, both due to the powder and of the nested integrals, means that the isotropic approximation is thought still to work rather well and no more sophisticated corrections are generally applied. As we mentioned before, a more accurate approach is to simulate the real experiment using Monte Carlo (e.g., see Howells, 1986) though this is rarely needed in practice. The standard approximate corrections appear only begin to break down when more than ∼% of the incident beam is getting scattered. For very thin samples, it is often adequate to carry out no multiple-scattering corrections at all without problem. Again, multiple-scattering corrections are present in most modern software data analysis programs.

5.3.7. X-Ray-Specific Corrections

5.3.7.1. Overview

Typical X-ray energies used in diffraction experiments are in the range 7–120 keV. Most excitations in materials, such as phonons and magnons, have energies on the scale of meV to eV. In order to resolve these inelastic processes explicitly, it is necessary to have an energy resolution of your measurement of $\Delta E/E \approx 10^{-6}$ or 0.0001% which is an extremely demanding task. Standard experimental practices in powder diffraction do not give nearly this resolution; for example, the use of an energy-resolving detector such as an intrinsic semiconductor detector gives an energy resolution of $\approx 20/20{,}000 = 10^{-3}$ or 0.1%. As a result, the coherent inelastic scattering from the sample, such as phonon scattering, is not resolved and these counts are integrated into the total measured counts: the measured "elastic" X-ray scattering includes all the unresolved low-energy inelastic scattering. The integral over energy of Eq. (5.7) is already carried out in the detector. Furthermore, on the energy scale of the measurement, this coherent inelastic scattering component lies very close to the elastic line, and to a very good approximation, the integration is carried out at a constant value of Q. This is described in detail in Chapter 7. The "elastic" scattering in an X-ray experiment is, to a high degree of precision, the total (or energy integrated) scattering that was defined in Eq. (5.7), plus any elastic incoherent contributions. A consequence of this fact is that the X-ray measurement is very fast on the time-scale of lattice vibrations. As far as the X-ray measurement is concerned, the atoms appear stationary and the resulting structure that is measured is the time, and sample, average of instantaneous snap-shots of the lattice vibrations (sometimes called the static approximation resulting in the "same-time" correlation function).

A second scattering process occurs for X-rays as well as the scattering that gives rise to the coherent elastic scattering. This is Compton scattering. Unbound or weakly bound electrons recoil during the scattering process. The scattering event must conserve momentum and energy. Consider an electron that is initially at rest. After an X-ray scatters off it, the momentum of the X-ray has changed and therefore the momentum of the electron must also change. Since the electron was initially at rest, it is clear that this collision with the photon starts it moving and therefore some energy was imparted to the electron from the X-ray: it is an inelastic process. It is also an incoherent process. This incoherent, inelastic, Compton scattering is often referred by X-ray scatterers simply as "inelastic scattering." This is correct but imprecise and can lead to the confusion we referred to in conversations between X-ray and neutron scatterers. The latter group generally thinks of phonon scattering and other inelastic coherent types of scattering on hearing the expression "inelastic scattering." In general, the electron that is scattering the X-ray is not at rest; it can be moving toward or away from the incoming X-ray. There is therefore a range of energies where Compton scattering occurs, symmetric about the energy shift of the stationary electron. Compton scattering contains information about the momentum distribution of electrons in the atoms and is sometimes used to probe this. An example of Compton and elastic scattering, measured at various Q-values in an MCA using a germanium solid-state detector, is shown in Fig. 5.5. For our purposes, it is an annoying incoherent background that must be removed. The best way to do this is to eliminate it by carrying out an experiment with good enough energy resolution. Failing this, the Compton scattered intensity can be calculated theoretically and subtracted as we describe below.

Another elastic incoherent contribution to the scattering is the self-scattering which occurs in the forward scattering direction. In general, this scattering is confined to very small angles and is inaccessible experimentally because of the incident beam. When large length-scale (nanometer) inhomogeneities exist in the sample, this forward scattering is spread out and becomes visible as small-angle scattering. As was discussed in Chapter 3, this small-angle scattering component is normally excluded, and, indeed, must be excluded in order to obtain the $G(r)$ function. Strictly speaking, this should therefore be explicitly removed from the data before obtaining $S(Q)$. In practice, the contribution from small-angle scattering is generally very small at angles accessible in a normal powder diffraction measurement and this contribution is rarely considered explicitly, though if it is significant it should be removed. In fact, the opposite problem is more common: that features in the wide-angle scattering that occur at low angle are missed in the experiment and this gives rise to long sine-wave-like aberrations in the PDF.

Another feature of the X-ray experiment is that the Thompson scattering process polarizes the scattered beam. The scattered beam is polarized such that the electric vector lies in a direction perpendicular to the scattering plane (the plane defined by the incoming and outgoing beams). Most X-ray
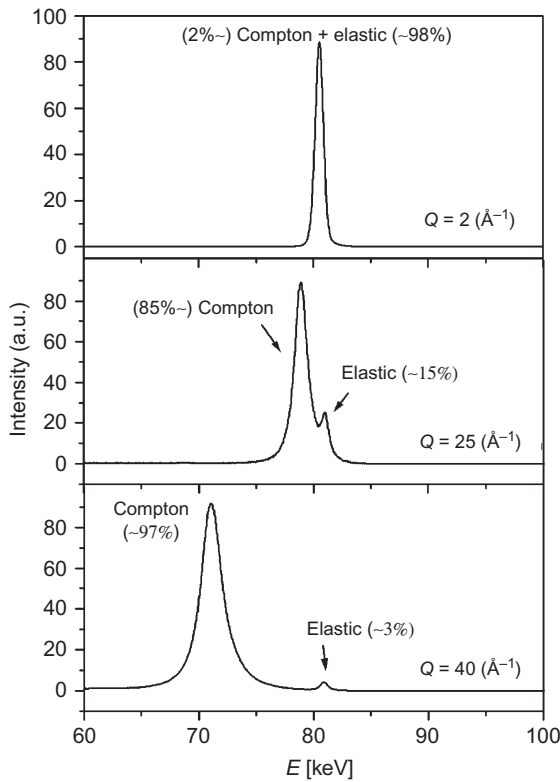
FIGURE 5.5 Comparison between measured Compton and elastic scattering intensities measured in silica glass using 80 keV X-rays. Note the Compton scattering is much stronger than the elastic signal at high-Q (Petkov *et al.*, 2000).

detection schemes are not sensitive to beam polarization, so, on first thought, this fact should not matter. However, on further thought, it becomes obvious that the sample is acting as a polarizer and so the measured intensity will depend on the degree and nature of the polarization of the incident beam. If the incident beam is also polarized with the electric vector perpendicular to the scattering plane, then the full intensity will be transmitted at all angles. However, if the incident beam is polarized in the scattering plane, the scattered intensity will depend on the scattering angle: it is modulated by a polarization correction that is given by the projection of the incident beam electric vector on a plane perpendicular to the scattered beam. For example, at a 90° scattering angle and the electric vector lying in the scattering plane, the scattered beam lies along the direction of the electric vector and the projection gives zero intensity. Clearly, even an unpolarized incident beam results in a polarization correction because an unpolarized beam can be decomposed into components that are parallel and perpendicular to the scattering plane. In this

case, the scattered intensity will be a minimum, but will not fall to zero, at $2\theta = 90°$. We note two interesting side effects of this polarization dependence of the scattering. First, it explains why most synchrotron X-ray experiments are carried out with a vertical scattering plane despite this configuration being more difficult from an engineering standpoint; it is because the X-ray beam from the synchrotron is polarized in the plane of the synchrotron ring. It is easier to stand the experiment on its side than to stand the synchrotron beam on its side! The second point to bear in mind is that a crystal monochromator that monochromatizes a beam by Bragg scattering also polarizes the beam. This should be accounted for in all quantitative X-ray data correction protocols.

5.3.7.2. Polarization Correction

As discussed above, X-rays become polarized by the scattering process and this affects the measured intensity as a function of scattering angle. The correction factor to account for this angle dependence of the scattering is

$$P_i = \frac{(1 + A\cos^2 2\theta)}{(1 + A)}, \tag{5.17}$$

where 2θ is the scattering angle and A depends on the degree of polarization of the incident beam. The term A is given by $A = (1 - f)/(1 + f)$. Here, f is the polarization rate of the incident radiation in the direction perpendicular to the scattering plane. If the radiation is unpolarized, $f = 0$ and $A = 1$; if it is fully plane polarized perpendicular to the scattering plane (the situation for synchrotron radiation exactly in the plane of the synchrotron ring), $f = 1$ and $A = 0$. In this case, there is no angle dependence to the scattered intensity due to polarization effects and therefore no polarization correction. In a real synchrotron experiment, the beam is not 100% plane polarized and A will take a small value in the vicinity of 5%. Note that when 2D detectors are being used, the polarization correction should be carried out on the data before it is integrated to 1D.

A number of special cases are worthy of note. When the source is unpolarized, but a crystal monochromator is used in the incident beam, the beam becomes partially polarized by the monochromator. In this case, $A = \cos^2 2\alpha$, where 2α is the scattering angle of the monochromator. Another common geometry is to have an unpolarized source incident on the sample but a monochromator in the scattered beam. In this case, the polarization correction becomes $P_i = ((1 - \cos^2 2\alpha \cos^2 2\theta)/2)$. Where it is not known, the degree of polarization of the beam can be determined experimentally (Egami, 1978).

Note that the commonly quoted Lorentz polarization factor, given by $\mathrm{LP} = ((1 - \cos^2\theta)/2\sin 2\theta)$ that includes the Lorentz factor, $1/\sin 2\theta$, should not be used. This contains two corrections. The first is the normal correction for beam polarization described above, P_i. The second is a phase-space correction

that should be applied to single crystal data when peak integrated intensities are measured. It effectively normalizes the integrated intensity by the volume of reciprocal space that it is measured over. This correction happens automatically in a powder diffractometer measurement.

5.3.7.3. Compton-Scattering Correction

The idea of Compton scattering was introduced in Section 5.3.1. Traditional measurements with low energy resolution were carried out by collecting the elastic and Compton scattering together and then subtracting the theoretical Compton contribution, $n^{\text{inc}}(Q)$ which is expressed as an intensity per atom in the sample. The Compton cross section (per atom) is given by

$$n^{\text{inc}}(Q) = \left(\frac{E_c}{E_0}\right)^{\alpha}\left[\sum_{a=1}^{n} c_a Z_a - \sum_{a=1}^{n} c_a f_a^2(Q)\right] \tag{5.18}$$

(Warren, 1990). It is simply (neglecting small cross terms between nonorthogonal electrons in neighboring atoms) the classical Thompson scattering intensity minus the coherent scattering power, expressed as $f_a^2(Q)$ for a particular atom, summed over all the atoms. The factor $(E_c/E_0)^{\alpha}$ is known as the Breit–Dirac recoil factor and is a small correction that takes into account the effects of radiation pressure. The exponent α can take values 2 (Ergun, 1968) or 3 (Warren, 1990) depending on the nature of the measurement. When photon flux is measured in a counter, the value 2 is used (Ergun, 1968). Compton intensities for all the atoms are tabulated in the International Tables of Crystallography C (Wilson, 1995). These curves have been fit using an empirical expression and parameterized for all the elements, see, for example, Thijsse (1984). Note that the calculated intensities from the International tables should be scaled by the Breit–Dirac recoil factor, before being subtracted from the data. Here, E_0 is the energy of the elastic scattering, and the average energy of the Compton scattering, E_c, is given by

$$\frac{E_0 - E_c}{E_c} = \frac{E_0}{m_e c^2}(1 - \cos\theta), \tag{5.19}$$

where m_e is the rest-mass of the electron, c is the speed of light, and θ is the half the scattering angle.

The parameters for determining $n^{\text{inc}}(Q)$ are now contained in a number of X-ray data analysis programs. The calculated Compton scattering should also be corrected for absorption before being subtracted, where account should be taken for the fact the Compton scattering has a different energy than the elastic scattering when evaluating the absorption correction (e.g., see Appendix 5.2).

When higher X-ray energies are used, and at higher scattering angles, the elastic scattering cross section decreases and the Compton cross section increases. The ratio of modified (Compton):unmodified scattering also increases as the elements in the sample get lighter. For modern high-resolution PDF measurements at high-Q, the Compton scattering can be considerably

stronger than the elastic signal. This is shown in Fig. 5.5 where the measured elastic and Compton scattering from silica glass measured with 80 keV X-rays is plotted. In this case, serious signal-to-noise problems may be encountered if the old mode of data collection is utilized. It was for this reason that it was thought for a long time that the use of 2D detectors in conjunction with high-energy X-rays, the RAPDF method, would not work. However, in this case, the high fluxes of X-rays available at modern sources, coupled with the highly parallel data collection (the entire Scherrer ring is collected instead of a small slice of it as in a 1D or 0D experiment), mean that the counting statistics in the high-Q region are very high, and even though the signal:noise is not favorable, it is possible to get a clean signal from the data and the RAPDF approach has largely replaced the use of point and line detectors for X-ray measurements, at least at synchrotrons.

When data are being measured using a point detector and high-Q is required, it is common practice to discriminate away the Compton scattering directly. However, a problem with this approach is that at low-Q the elastic and Compton shifted intensities often cannot be resolved. In this case, a method is used where the theoretical Compton is subtracted from the low-Q data and the Compton scattering is discriminated away at high-Q. In the crossover region, the subtracted theoretical Compton component is gradually reduced using a smooth interpolation function. A road-map for doing this that takes into account the finite width of the Compton scattering (generally ignored in the simple Compton subtractions described above) was suggested by Ruland (1964). The proportion of Compton modified scattering that appears in the measured elastic scattering is then given by $R(Q) = \int W(E) n^{\mathrm{inc}}(Q,E) \mathrm{d}E / \int n^{\mathrm{inc}}(Q,E) \mathrm{d}E$, where $W(E)$ is the band-pass function of the detection device and $n^{\mathrm{inc}}(Q,E)$ is the Compton profile. The Compton profile $n^{\mathrm{inc}}(Q = 40 \, \text{Å}, E)$ for silica glass can be seen in Fig. 5.5 as the broad, Lorentzian-like, peak just below the elastic scattering intensity at channel number 640. Then $R(Q) n^{\mathrm{inc}}(Q)$ is subtracted from the data rather than $n^{\mathrm{inc}}(Q, E)$ directly. In practice, neither $W(E)$ nor the exact energy dependence of the Compton profile is known accurately and an empirically determined $R(Q)$ is used. The form

$$R(Q) = \left\{ \left(1 + \frac{Y}{b} \right) \left[1 + \frac{Q^2 d}{(Y+b)^2} \right] \right\}^{-1}$$

has been suggested by Ruland (1964). Here, λ and λ' are the wavelengths of the elastic, and Compton-modified, scattering, respectively. Y is a Q-dependent function given by $Y = cQ^3/(a^2 + Q^2)$. In these equations, a–d are constants. The Ruland function given above is not entirely satisfactory (e.g., see Thijsse, 1984) and is not strictly applicable to the modern experimental setup with energy discrimination by MCA, and a purely empirical function is often used as illustrated in Fig. 5.6.

A more accurate method for removing Compton scattering is to calculate the full profile, $n^{\mathrm{inc}}(Q, E)$, within some approximation for the momentum
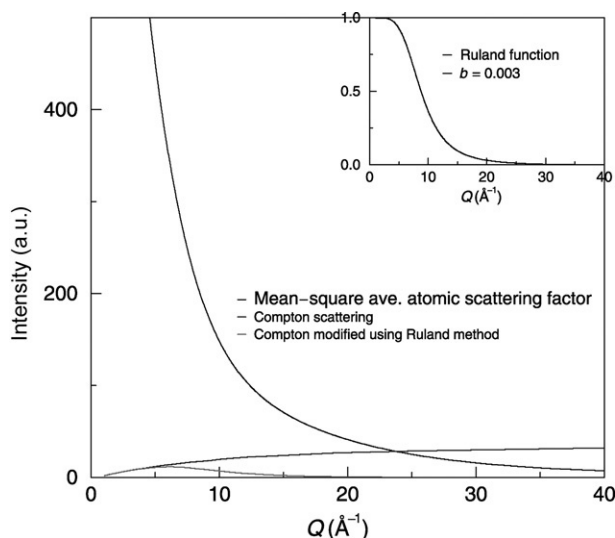
FIGURE 5.6 Comparison between mean-square average atomic scattering factor, $\langle f^2(Q)\rangle$, Compton, and modified Compton contributions to the intensity as a function of Q. The modified Compton curve was multiplied by the Ruland function shown in the inset calculated for an integral width of $b=0.003$ (PDFgetX manual).

distribution in the atom, at every Q value. Then the X-ray spectrum contained in the MCA can be fit with two peaks originating from the Compton and elastic scattering, respectively. The fit can be constrained. For example, the energy shift of the center of the Compton peak is known (Eq. 5.19). The desired elastically scattered intensities are then obtained from the integrated area under the fit elastic peak, or better, by subtracting the calculated Compton peak and integrating numerically the residual counts. This approach has been demonstrated by Laaziri *et al.* (1999). It is computationally very intensive and is easier on simple systems with low-Z elements, as in the case of amorphous silicon (Laaziri *et al.*, 1999). In general, the empirical Ruland method is more often used except where the highest accuracy is required.

5.3.7.4.   Atomic Form-Factor

The final step in determining $S(Q)$ is to divide the data by $\langle f(Q)\rangle^2$ (Eq. 5.1) where this is defined as

$$\langle f(Q)\rangle^2 = \left[\sum_a c_a \left(f_0^a(Q) + f_a' + i f_a''\right)\right]^2 = \left[\sum_a c_a \left(f_0^a(Q) + f_a'\right)\right]^2 + \left[\sum_a c_a f_a''\right]^2.$$
$$(5.20)$$

Here, the sum is over atomic species of concentration c_a, $f_0^a(Q)$ is the atomic form-factor for species a, and f_a' and f_a'' are the anomalous scattering corrections to the form-factor. The i indicates an imaginary number. The

anomalous scattering corrections can be neglected unless the incident X-ray energy is close (within $\sim$ eV) to an absorption edge of one of the elements.

The factor $f_0^a(Q)$ is strongly Q-dependent. It has been calculated for all the elements using relativistic or nonrelativistic Hartree–Foch or Dirac–Slater atomic wavefunctions and the results tabulated (Doyle and Turner, 1968; Fox *et al*., 1989; Wilson, 1995). They are tabulated in one place for all the elements in the International Tables for Crystallography C (Wilson, 1995). These data have been fit and parameterized. Originally, they were expressed as a sum of Gaussians in the low-Q region up to $Q \sim \text{Å}^{-1}$ and in the high-Q region $\ln(f(Q))$ was expressed as a polynomial series (Wilson, 1995). The parameters for each element are in the International Tables of Crystallography C, Tables 6.1.1.4 and 6.1.1.s5 (Wilson, 1995). Clearly, having to join the low- and high-Q ranges is something of a pain. More recently, Waasmaier and Kirfel (1995) have presented new parameterizations for all the elements where the $f(Q)$ functions have been successfully fit over the full range of Q to 75 Å^{-1} using a fit to a sum of 5 Gaussians plus a constant:

$$f(s) = \sum_{i=1}^{5} a_i e^{-b_i s^2} + c, \qquad (5.21)$$

where $s = Q/4\pi$.

Anomalous scattering factors for the elements have also been calculated (Cromer and Liberman, 1970, also see the discussion in Kissel *et al*., 1995). When these need to be known accurately, for example, in an anomalous scattering experiment, it is generally better to evaluate them experimentally by measuring the absorption edge of the element in question and carrying out a Kramers–Kronig transformation on the experimental data (e.g., see Price and Saboungi, 1998; Petkov *et al*., 2000 and references therein).

Because of their importance over a wide spectrum of the sciences and the fact that they are difficult to determine accurately, calculations of atomic scattering factors are constantly being reexamined and improved. See for example, Kissel *et al*. (1995) for a thorough reexamination of the situation as of 1995. With improvements in computing, it is also possible to start trying to take into account solid-state effects that change the electron distribution and, therefore, modify the scattering factor (in general, free-atom scattering factors are used) (Ankudinov and Rehr, 2000).

The other important average form-factor average needed is $\langle f^2(Q) \rangle$. This is proportional to the total sample scattering cross section, including coherent and Laue incoherent scattering, and is defined as

$$\langle f^2(Q) \rangle = \sum_a c_a \left[\left(f_0^a(Q) + f_a' \right)^2 + \left(f_a'' \right)^2 \right], \qquad (5.22)$$

where the symbols have the same meaning as in Eq. (5.20).

An example of corrected, normalized data with $\langle f^2(Q) \rangle$ superimposed on top is shown in Fig. 5.7. When the data are divided by $\langle f^2(Q) \rangle$ and plotted with the Q weighting as $Q(S(Q) - 1)$, significant diffuse scattering is evident at high-Q that is not apparent in the corrected but undivided data, as shown in Fig. 5.8.

5.3.7.5.   Putting It All Together

Putting together the general expression for the sample single-scattering cross section, Eq. (5.8), and the specific X-ray corrections, we get

$$\left(\frac{d\sigma^s}{d\Omega}\right) = \left[\left(\frac{N'}{M'}\right)^{sc} - \left(\frac{V'_{c;sca}}{V'_{c;ca}}\right)\left(\frac{N'}{M'}\right)^c\right]\left(\frac{1}{P_i V'_{s;sca} \rho^s D d\Omega K \varepsilon_d}\right) - m'$$
$$- R\left[n^{inc} + m^{inel}\right], \tag{5.23}$$

where the terms not defined above are defined in Appendix 5.1. The primes on the N and M denote that the data are dead time corrected. Here, m' is the multiple scattering calculated assuming only elastic scattering and m^{inel} is the additional multiple scattering where at least one of the scattering events was an inelastic (Compton) event. Since in the high-Q region where the multiple scattering becomes important, the Ruland window function $R(Q)$ is almost zero, m^{inel} is often neglected. m^{inel} can be significant, and should be calculated, when the Compton is not experimentally discriminated away.

In Eq. (5.23), everything is known well except the product $\rho^s D d\Omega K \varepsilon_d$. In general, none of these factors depends on Q (only $d\Omega$, the detector solid angle, may change with Q if the detector slits or the detector-sample distance vary during the experiment), so the product is simply an unknown constant, β. This
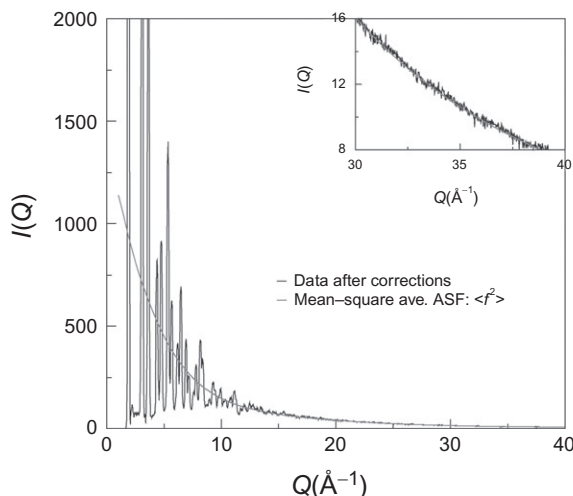

FIGURE 5.7   Comparison between normalized data after corrections and the calculated mean-square average atomic scattering factor, $\langle f^2(Q) \rangle$ (PDFgetX manual).
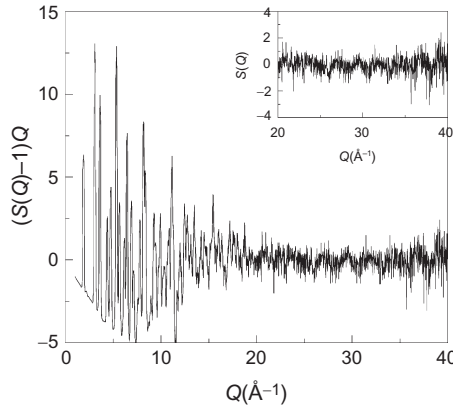
FIGURE 5.8 Same data as shown in Fig. 5.10, but the data are now plotted in the form of $Q(S(Q)-1)$ after being divided by $\langle f(Q)\rangle^2$ to obtain $S(Q)$. Significant diffuse scattering is evident at high-Q that is not immediately apparent in Fig. 5.7 (PDFgetX manual).

scale factor can be estimated by observing that in the high-Q region the scattering from the sample is mostly incoherent and approximately equal to $\langle f^2(Q)\rangle$. Thus, substituting $\langle f^2(Q)\rangle$ for $(d\sigma^s/d\Omega)$ in Eq. (5.23) and rearranging we get

$$\beta = \frac{\lim\limits_{Q\to Q_{max}}\left[\left(\frac{N'}{M'}\right)^{sc} - \left(\frac{V'_{c;sca}}{V'_{c;ca}}\right)\left(\frac{N'}{M'}\right)^{c}\right]}{P_i V'_{s;sca}\left(\langle f^2(Q)\rangle + m' + R(n^{inc} + m^{inc})\right)}. \tag{5.24}$$

Note that if the Compton scattering has been completely discriminated at high-Q, then R is zero here and the theoretically calculated Compton scattering, n^{inc}, and inelastic multiple scattering, m^{inc}, should not be included. More elaborate approaches for data normalization making use of a wider range of data have also been proposed (Thijsse, 1984; Kaszkur, 1990; Cumbrera and Sanchez-Bao, 1995). Finally,

$$\left(\frac{d\sigma^s}{d\Omega}\right) = \left[\left(\frac{N'}{M'}\right)^{sc} - \left(\frac{V'_{c;sca}}{V'_{c;ca}}\right)\left(\frac{N'}{M'}\right)^{c}\right]\left(\frac{1}{P_i V'_{s;sca}\beta}\right) - m' - R\left[n^{inc} + m^{inc}\right]. \tag{5.25}$$

5.3.7.6. Rapid Acquisition PDF-Specific Corrections

The rapid acquisition PDF (RAPDF) data collection method makes use of 2D detectors for the data collection. Since its introduction in 2003 (Chupas *et al.*, 2003), it has become the most popular X-ray PDF data collection method. Here, we discuss aspects of the data corrections to obtain PDFs from RAPDF data. A schematic of the data collection and processing, including modeling of the RAPDF method, is shown in Fig. 5.9. This is the same image that is on the cover of this edition reflecting our view of the the revolutionary impact this development has had for the PDF method.
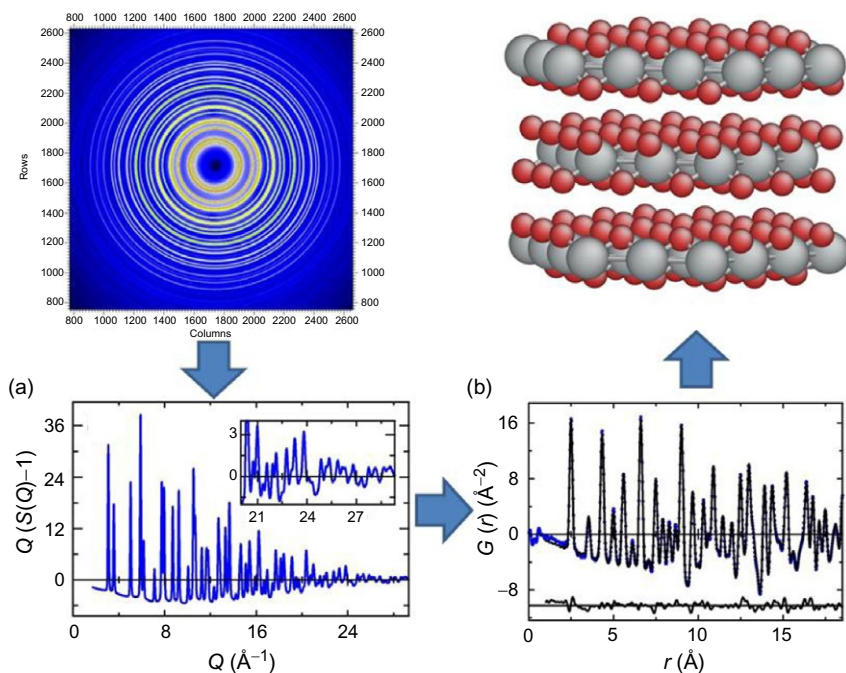
(a)   (b)

FIGURE 5.9 Schematic of the RAPDF data collection, reduction and modeling to obtain nanostructure information. Top left shows the 2D image on the image-plate detector. Lower left panel is the properly corrected and normalized data from this image after integrating to 1D and having all the corrections applied. Lower right panel shows the same data after they are Fourier transformed to the PDF, with a PDF of a model plotted on top of the data. The top right panel shows schematically what the nano-scale structural model may look like.

The 2D detectors that are currently used are integrating, rather than photon counting, detectors such as image plate, amorphous silicon, and (to a lesser extent) CCD detectors. These detectors do not discriminate photon energy. The energy from absorbed X-ray photons is stored in the location in the detector where the photon arrived, and later, this information is read out. Because individual photon absorption events are not detected, when the information is read out, there is an unknown gain, and so the numbers obtained from the detector are proportional to, but not equal to, the number of counts. This results in reliable relative intensities but it means that the statistical uncertainties on the data are not given by the square root of the raw, dead time corrected, counts as for photon counting detectors. This presents challenges for estimating and then propagating uncertainties which are described in Section 5.3.4.

Two-dimensional detectors do not have uniform sensitivity across their surface and a flat field (sometimes called flood field) correction must be

carried out. This is usually a calibration that is done by the detector manufacturer, and a flat field correction file is supplied with each detector that corrects for the pixel to pixel efficiency differences. Depending on the technology of the detector, there may also be spatial distortions to the image. This is common if a phosphor is optically coupled to a CCD chip, for example. In this case, there will also be a geometric correction file that is supplied by the manufacturer that should be applied. It is created by imaging a known uniform grid and mapping pixel positions back to where they should be to recover the known uniform grid from the distorted image of it. Also depending on the technology of the detector, it is often necessary to collect a dark-current measurement, which is basically taking an image with no X-rays shining. This is not required for an image-plate detector but is important for CCD and amorphous silicon technologies. In these cases, it is typical to take data in pairs with equal dark/light exposures. The first data correction step is then to process the raw images by applying any flat field and geometric corrections and subtracting the dark image from the light image.

The next step is to sum together or average any duplicate images. Data collection is carried out in such a way that any individual exposure of the detector does not saturate pixels on the detector. Then, to build up sufficient counting statistics on weaker features, multiple exposures are taken. These separate images are then combined. This can be done by summing or averaging them. A number of programs exist for manipulating images. The most commonly used is Fit2d (Hammersley *et al*., 1996; Hammersley, 2004). But others such as Powder3D (Hinrichsen *et al*., 2006) (http://www.fkf.mpg.de/xray/html/powder3D.html) are also available and others are emerging, such as PDFlive (Yang *et al*., unpublished). The data images should be visually assessed. They are rich in information about the quality of the experiment, for example, the spottiness of the Debye–Scherrer rings gives information about the powder average of the sample. It is also possible to see the width of features and get some feeling for signal/background, though this is often better estimated after integration to a 1D pattern.

Before data can be integrated from 2D to 1D, a calibration has to be carried out. A standard sample is measured. The Fit2d program has a number of built-in calibration materials, and it is convenient to use one of these (they are standard things such as silicon, LaB_6, etc.); however, any material with known lattice parameter can be used as a calibration material and the lattice parameters can be input to Fit2D. The image processing software will be used to integrate the intensities around the Debye–Scherrer rings, which are nominally circles. To do this, it is necessary to find the pixel coordinate of the center of the circles. Also, any nonorthogonality of the detector to the incident X-ray beam will result in the circles becomes ellipses. Fit2D uses a regression algorithm to detect any small deviation from circular rings and returns angular offset parameters. The calibration measurement thus returns a number of parameters: the sample-detector distance or camera length, two angular offset

parameters, and the pixel coordinate of the beam center. For this to occur correctly, the user needs to know the pixel size in the detector. In image place detectors, they are not pixelated *per se*, but a resolution is selected when the image is read giving an effective pixelation. Once the user has obtained these parameters from the calibration measurement, these are entered into the respective fields in Fit2d, or whatever software is being used, so that the 2D->1D integration can proceed for the sample. Clearly, it is important to ensure that the calibration data were collected with the exact and unperturbed setup that is used for collecting the sample data, or else the calibration constants will not be transferrable.

Finally, before integration, it is possible to mask regions of the image to be ignored in the integration. This can be done in a number of ways. First, it is possible to define "cake-slices" to take different sections of the circular image and ignore other regions. Second, it is possible to set a threshold mask so that, for example, any saturated pixels (mask all pixels above a high threshold) or dead pixels (mask all pixels below a low threshold) are ignored. Finally, it is possible to construct any kind of geometrical shape as a mask to eliminate regions as desired. This last case is often used to mask a region containing the beam-stop for example. It is also sometimes helpful to mask the pixels at the very edge of the detector as sometimes integration errors occur at the detector edge.

The image can now be azimuthally integrated resulting in a 1D pattern. It is possible to carry out any background subtraction (e.g., from an empty sample capillary) in the raw images or from the integrated 1D datasets, depending on which is more convenient or gives the more certain results. If the background scaling can be estimated better in the raw than the integrated image (this is the case for some electron diffraction measurements where there is a clear noncircularly-symmetric ghost image of the electron source), then it may be better to do the subtraction on the unintegrated data. However, in general, there is more control in the background subtraction steps at the data reduction step in programs such as PDFgetX2 and PDFgetX3, and in general, the background data are treated as actual datasets up to the point of integration. Any corrections that depend on azimuthal angle, for example, the X-ray polarization correction, should be done before (or rather, during) the integration step. This is a standard correction in Fit2d, though care must be taken to make sure that the physical orientation of the detector is correctly translated to the image processing program: sometimes images are rotated from the physical orientation by the image capture software, and in this case, the polarization correction will not be carried out correctly (in fact, the polarization effect will be amplified by the correction!).

In general, it was thought important to discriminate incoherent signals that contribute to the measured intensity but not the signal, such as Compton scattering and Fluorescence, for example. The thinking behind this was that statistics are important and the best way to get good statistics is to improve

signal–noise. In some sense, it was a surprise when the RAPDF method worked so well because it went against all of this prior wisdom. The measured intensity contains all of the inelastic incoherent signals, including Compton scattering which for high-incident X-ray energies can be larger than the coherent elastic scattering. Nonetheless, the method works well because of the high intensities of the incident beam and the parallel counting afforded by the 2D detector so that sufficient raw counts can be collected to overcome the poor signal–noise. One of the advantages in this case is that the data corrections tend to work rather well. It turns out that it is easier to estimate the theoretical Compton scattering and to subtract it than to have the situation that occurs when you try to discriminate away the Compton scattering with an energy-resolving detection setup. In the latter case, the Compton scattering is in the signal at low-Q but gradually moves out of the resolution window of the measurement in an unknown way with increasing-Q. It turns out that this can be a rather difficult thing to correct for adequately.

Other than the things discussed above, the corrections for RAPDF data are quite similar to those for regular X-ray powder diffraction data. One additional geometric correction should be made to account for the transparency of the photon absorbing phosphors of the detectors. At the high X-ray energies used for RAPDF experiments, the X-rays tend to penetrate deeply, and often all the way through, the phosphor. This means that the path length of the photon through the phosphor is angle dependent, being longer at higher angles (in the forward scattering geometry used). Since the probability of depositing its energy in the phosphor is proportional to this path length, there is a slight tendency to overcount photons at higher angles compared to lower angles. This additional geometric correction is incorporated into PDFgetX2.

5.3.8.   Time-of-Flight Neutron-Specific Corrections

5.3.8.1.   Overview

Neutrons that have appropriate wavelengths for structural studies have thermal energies: $\approx$ meV. This is comparable to the energy of solid-state excitations such as phonons and magnons. Many typical diffraction geometries will have sufficient energy resolution to choose whether these effects are included or excluded in the measured scattering intensity. Thus, it is possible to obtain two distinct differential scattering cross sections: the elastic differential cross section $d\sigma/d\Omega(\Delta E = 0)$ and the total scattering differential cross section, $d\sigma/d\Omega$, as we discuss in Chapter 7. A perfectly legitimate PDF can be obtained from either cross section, the former giving the time-averaged structure (time-dependent atomic correlations are lost) and the latter giving the average of the instantaneous structure (time-dependent correlations are preserved). By varying the range of energy over which the data are integrated,

the time-scale of the experiment can be continuously varied. For example, if the range of integration, ΔE, is larger than the energy range of the phonons (≈ 100 meV), then the measurement is quicker than the lattice vibrations and the correlated atom displacements (the phonons) will be seen explicitly in the resulting PDF. This is (approximately) the situation in the most common neutron PDF experiments; the tof powder diffraction experiment at a spallation neutron source. In this case, as with the X-rays, the measured intensity is automatically integrated over all energy transfers.

As with X-rays, there are additional scattering processes for neutrons that do not yield structural information. In the case of neutrons, it is the magnetic scattering. To obtain a purely structural PDF, it is necessary to remove magnetic scattering from the measured intensity. In practice, this is often neglected. The reason that this is possible is that the magnetic scattering contributes rather weakly to the PDF. Because of the magnetic form-factor, coherent magnetic scattering is confined to rather low Q-values, whereas the nuclear scattering extends to high-Q. All data at all Q-values are used in the PDF, but high-Q scattering is relatively more important because of the Q-weighting in the kernel of the Fourier transform. If the magnetic scattering is not explicitly removed from the data, it distorts the resulting structural PDF. However, experience suggests that the distortion to the PDF is small enough (it is a weak long-wavelength oscillation) to be neglected in most cases. On the other hand, as was discussed in Section 3.3.2, it is possible to remove the nuclear scattering component and Fourier-transform the magnetic scattering to learn about magnetic correlations in the solid or model it directly in Q-space. As with X-rays, significant small angle scattering should be removed, though similar arguments that apply to the magnetic scattering also apply to the small angle intensity. Finally, we note that the scattering of neutrons by nuclei is isotropic (s-wave) and does not introduce any polarization so there is no polarization correction for nuclear scattering.

Thus, to obtain $S(Q)$ from the corrected intensity from an energy integrated experiment (tof neutron powder diffraction experiment, or a two-circle reactor experiment with no energy analysis), first, if desired, the magnetic scattering should be removed. Then the elastic incoherent scattering, small angle and $\langle b \rangle^2 - \langle b^2 \rangle$, is removed and the resulting coherent single-scattering intensity divided by the mean scattering length squared, $\langle b \rangle^2$ according to Eq. (5.1). $\langle b \rangle^2$ and $\langle b^2 \rangle$ are defined in the same way as the average form-factors (Eqs. 5.20 and 5.22) except the sums run over all isotopes and spin-states of the nuclei as well as over chemical species. In practice, the information about the sum over isotopes and nuclear spin-states are contained in tabulated values of the coherent and incoherent nuclear cross sections for elements in their natural abundances.

The energy dependence of the neutron scattering cross sections is assumed to be linear with wavelength. A better approximation is to measure the energy dependence of the ratio of the transmitted beam to the incident beam. This is

done by placing a vanadium monitor downstream of the sample in addition to the upstream monitor. This ratio yields the total attenuation cross section of the sample from which can be extracted the average scattering cross section (Howe *et al*., 1989; Soper *et al*., 1989).

In an energy-analyzed experiment (triple-axis measurement at a reactor or a measurement at a chopper spectrometer at a spallation source), the data should be integrated over the desired range of energy transfer to obtain $d\sigma/d\Omega$ (Chapter 3). This should then be treated in the same way as the energy integrated measurements to obtain $S(Q)$.

5.3.8.2. Datasets

It is normal to collect a number of datasets as well as the sample data in order to make the necessary data corrections.

Sample data. Sample is usually in a container, or can, and mounted in some sample environment (cold-stage, furnace, cryostat, magnet, pressure cell, etc.)

Empty sample can. The sample container is mounted in the same environment as the sample was measured but empty. This dataset is typically collected with less integrated incident flux than the sample datasets received. However, better statistics are required in the container data if the scattering from the container is significant. The rule of thumb is that the measurement time should be in proportion with the strength of the scattering. Provided there is good reproducibility between sample containers, it is not necessary to measure exactly the same container as held the sample.

Empty environment. An additional background is measured from the diffractometer without anything at the sample position but all the rest of the sample environment in place. This is the instrument background. Collection time depends on how large the background is. The data can be collected for considerably less time (e.g., 1/4 the collection time) if there is a negligibly small background as is generally the case for measurements in ambient temperatures and pressures. However, if an environment is used with significant background such as a furnace or pressure cell so that the background scattering is a significant proportion of the total measured scattering, then data should be collected for longer.

Vanadium rod. Vanadium is an almost perfectly incoherent scatterer of neutrons. It is customary to measure a sample of vanadium to determine the source spectrum. This dataset should be measured with good accuracy as it will be used to normalize all the other datasets. This need not be measured in a sample environment (indeed, it is better to make this measurement with a low background for increased accuracy). However, it should be made close in time to the main measurements to ensure that slowly varying changes in the source spectrum are accounted for as well as possible. Careful experimenters often measure a series of vanadium datasets periodically throughout an

experiment. These are combined together for increased statistics and to average out long time-scale fluctuations in the spectrum.

Crystalline standard. A sample with known lattice parameters is also run periodically. This is used to convert accurately the neutron tof information into momentum transfer, Q. This must be done individually for each detector for the greatest accuracy and resolution to be obtained when detectors are combined. The standard sample is often silicon or quartz.

Intensity standard. As discussed in Section A5.4, a crystalline standard with similar total scattering cross section to the sample may also be measured to help achieve an absolute intensity normalization.

Datasets 5 and 6 are optional. The Q-calibration is often carried out by the instrument scientist of the diffractometer and standard calibrations are available on file. The intensity calibration is only required if the absolute intensity of a PDF is required with high accuracy. Additional vanadium container and vanadium background runs may also be required if, for some reason, the vanadium is supported in a container.

5.3.8.3.   Converting tof to Q

For a given value of 2θ, the value of Q depends on the wavelength which is obtained from the tof of the neutron. A polychromatic pulse of neutrons of width $\sim\mu s$ emerges from the moderator at time $t=0$. The neutrons fly down the primary flight path, L_1, which is typically of order 10 m or more to the sample. After scattering, the neutrons fly along the secondary flight path ($L_2 \sim m$) to the detectors. The tof, τ, is the time it takes for the neutron to get from the moderator to the detector. If an elastic scattering event is assumed in the sample, this directly gives the velocity of the neutron, v, its momentum and therefore its wavelength using the de Broglie relationship, that is,

$$v = \frac{L_2 + L_1}{\tau} = \frac{L}{\tau}, \quad p = m_n v = \hbar k, \quad \lambda = \frac{2\pi}{k} = \frac{2\pi \hbar \tau}{m(L_1 + L_2)}. \tag{5.26}$$

Some useful empirical relationships that hold for neutrons are given below:

$$k\left(\text{Å}^{-1}\right) = \frac{1588.2 L(m)}{\tau(\mu s)}, \quad \lambda(\text{Å}) = \frac{0.0039562 \, \tau(\mu s)}{L(m)}, \tag{5.27}$$

$$E(\text{meV}) = \frac{81.807}{\lambda^2(\text{Å})}. \tag{5.28}$$

In practice, the $t=0$ point is not perfectly known and the exact trajectory through the instrument can depend on the sample position for example. To obtain accurate Q-values, it is therefore necessary to make corrections to the above expressions using a calibration standard. A standard crystalline sample is run and a number of diffractometer constants are determined for

each detector or detector bank. The same practice is used when powder dif-
fractometers are used for Rietveld refinement studies. However, we note here
that the diffractometer constants used in Rietveld refinements are not, in gen-
eral, suitable for PDF measurements. The reason is that pulsed neutron peaks
are highly asymmetric. Rietveld refinements determine the peak position
according to some arbitrary consideration, for example, the peak maximum.
This is fine if the same Rietveld code is used to analyze the calibration sample
and the data themselves since the Q-assignment is done in a self-consistent
way. However, in a PDF analysis, the data are Fourier transformed and the
continuous distribution of intensity as a function of Q is required; the absolute
value of Q of each data point is therefore needed. Ideally, the data should be
deconvoluted from the instrument resolution function. In practice, empirical
diffractometer constants are determined with different Q-dependences to
account for these effects.

5.3.8.4.   Detector Dead-time Corrections

Corrections have to be made to the simple detector dead-time equations
(Eq. 5.15) if the dead time is greater than the tof channel width (Soper *et al.*,
1989). Then the dead-time correction in a particular time-channel depends on
the count-rate in nearby earlier time channels. In this case,

$$R = \frac{\Delta R_m}{\left(\Delta - \tau_d \sum_j \Delta_j R_j\right)}, \tag{5.29}$$

where the sum goes over all the time channels which affect the channel in
question. Other complications can arise if detectors are multiplexed so that
more than one detector feeds through some part of the data-acquisition elec-
tronics. In this case, an additional dead time can be introduced because of a
high count-rate in a different detector and the sum in Eq. (5.29) should be a
double sum over all the time channels and detectors which affect the time
channel in the detector in question.

Detector dead-time corrections are generally sorted out by the staff at the
neutron facility and are not generally the concern of the user other than to
ensure that they are properly accounted for.

5.3.8.5.   Inelasticity (Placzek) Corrections

Unlike with X-rays, the energy of the thermal neutron is comparable to
the energies of low-energy excitations (phonons and magnons) in the solid.
Thus, when the neutrons are scattered inelastically, their energy changes sig-
nificantly. This is made extensive use of in the field of inelastic neutron scat-
tering. Lattice dynamics and inelastic scattering in the context of total
scattering studies are discussed in detail in Chapter 7. Here, we discuss simply

corrections that have to be applied to the data to account for inelastically scattered neutrons that become incorrectly binned in Q. This occurs because of the geometry of the experiment. It amounts to making the integration of the double-differential cross section over energy not along a path of constant-Q as assumed in the definition. It occurs for reactor-based angle dispersive measurements as well as tof neutron measurements though the corrections are different. It is described in detail in Section 7.5.1. To carry out a precise correction, the sample dynamic structure factor, $S(Q, \omega)$, must be known as well as the loci through (Q, ω) space along which inelastic neutrons are integrated due to the specific geometry of the measurement. For example, loci of integration for various detectors on the, now retired, LAD diffractometer at ISIS are shown in Fig. 5.10. The deviations from ideal (constant-Q) loci are clearly largest at small diffraction angle and small-Q. A complete correction is impossible because, in general, we are trying to measure $S(Q)$, so if we already knew $S(Q, \omega)$ as required to make the correction, we would not have to measure $S(Q)$! An approximate approach is to expand $S(Q, \omega)$ in moments. The first few moments do not involve details of the potential and phonon
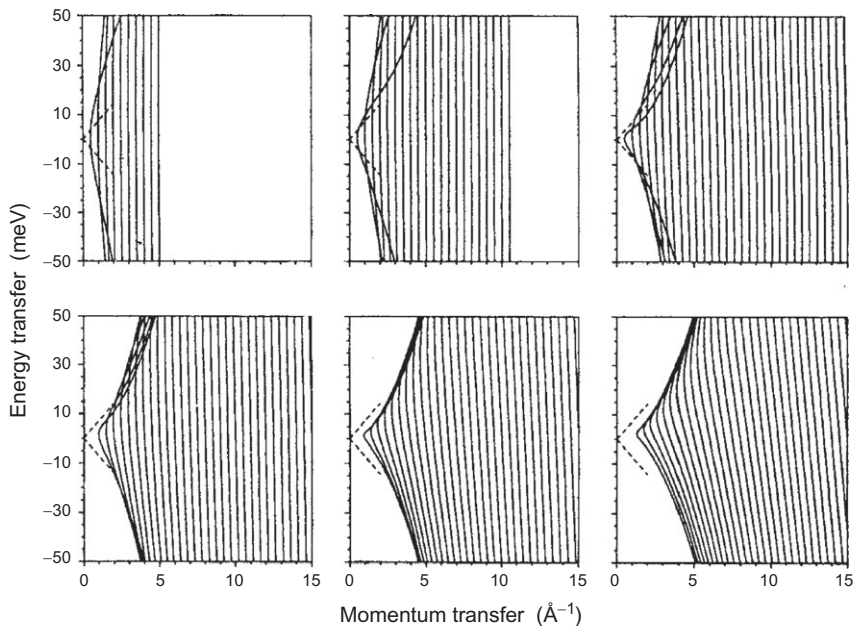

FIGURE 5.10   Loci of integration from time of flight neutron powder diffractometer LAD. The vertical axis shows energy transfer, $\hbar\omega$, and the horizontal axis shows Q. Neutrons that are scattered inelastically (i.e., at finite ω) will be assigned an incorrect Q-value because of the geometry of the tof experiment. The Q-value that will be assigned to an inelastically scattered neutron can be deduced by following the line from the (Q,ω) value of the scattering event to the $\omega = 0$ line. The six panels correspond to the six detector banks on LAD at (top left to bottom right) $2\theta = 5°$ $10°$, $20°$, $35°$, $58°$, and $90°$ (Howe *et al.*, 1989).

band-structure and so the approximation is made that the correction involving only these first few terms is sufficient (Section 7.5.1). This approach was first laid out by Placzek (1952) and developed by Yarnell *et al.* (1973) and Powles (1973) for reactor experiments and further refined and extended to tof neutron experiments by Howe *et al.* (1989). By way of example, the corrections for a model system of free atoms are shown in Fig. 5.11 (Howe *et al.*, 1989) with mass of 84.2 g/mol (the average of Cs and Cl) and assuming the LAD detectors (Howe *et al.*, 1989).

The result of this kind of analysis is an additive correction, $P^{inc}(Q, 2\theta)$, to the measured intensities. The corrections are small since the scale in these plots is 10^{-3} b sr^{-1} that compares with typical scattering cross sections of the order 1 b sr^{-1}. The corrections become more significant as the mass of the scatterer gets less. From Fig. 5.11, we see that the corrections become significant at low-Q. In this model system, $S(Q, \omega)$ is known and the exact correction can be calculated and is shown as a dotted line. It is apparent from this test that the approximate Placzek corrections to second-order work well for the low-angle detectors but not very well at higher scattering angle. Therefore,
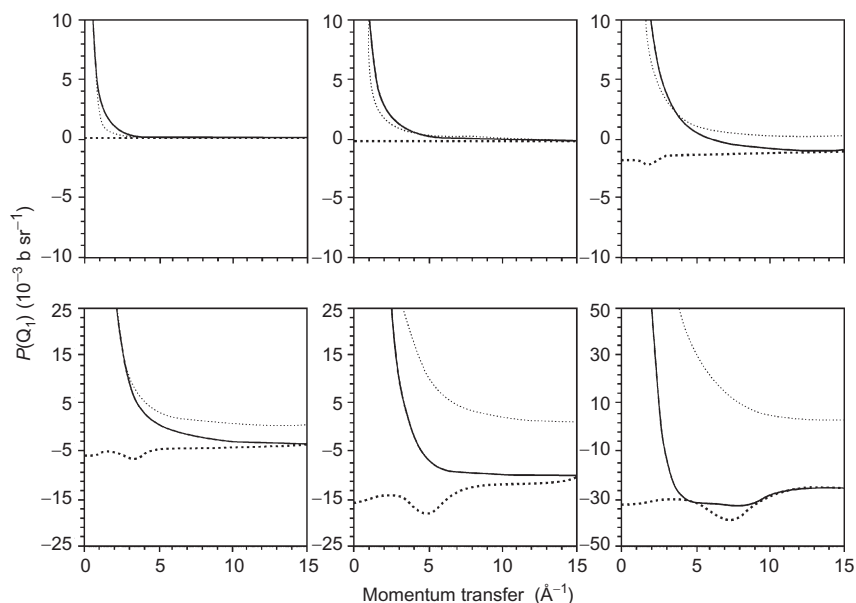
FIGURE 5.11   Inelasticity corrections to the scattered intensity as a function of Q for the six detector banks of LAD shown in Fig. 5.9 (from top left to bottom right $2\theta = 5°$ $10°$, $20°$, $35°$, $58°$). The dotted curves are the exact result from model calculations on CsCl. The dashed curves are given by the approximate Placzek correction taken to first order. The solid curves are the approximate Placzek correction taken to second order. Notice that the corrections are most significant at low-Q and that the approximate corrections to second-order work best at low detector angles (Howe *et al.*, 1989).

for studying liquids of low atomic mass (e.g., water and organic liquids), low angle detectors should be utilized. This insight led to the building of the SANDALS diffractometer at ISIS. Bound atoms do not recoil so much and there is much less inelastic scattering as a proportion of the total scattering, so this becomes less of an issue (though does not go away) in solids.

5.3.8.6. Putting It All Together

As in the case of X-ray scattering, we can put together the specific corrections discussed here with the general corrections (Eq. 5.8). In this case, the flux, detector efficiencies, and detector profiles are Q-dependent; however, by measuring an incoherently scattering vanadium sample, we have a dynamic measurement of all these quantities. Thus, we have

$$\left(\frac{d\sigma^s}{d\Omega}\right) = \left[\left(\frac{N'}{M'}\right)^{sc} - \left(\frac{V'_{c;sca}}{V'_{c;ca}}\right)\left(\frac{N'}{M'}\right)^{c}\right]\left(\frac{1}{V'_{s;sca}\rho^s D d\Omega K \varepsilon_d}\right) - m' - P^{inel} \tag{5.30}$$

and

$$\left(\frac{d\sigma^v}{d\Omega}\right) = \left[\left(\frac{N'}{M'}\right)^{vc} - \left(\frac{V'_{c(v);vca}}{V'_{c(v);ca}}\right)\left(\frac{N'}{M'}\right)^{c(v)}\right]\left(\frac{1}{V'_{v;vca}\rho^v D d\Omega K \varepsilon_d}\right) - m'_v - P^{inel}_v \tag{5.31}$$

from the sample and vanadium experiments, respectively. Note that c(v) refers to scattering from the vanadium container, if one was used. The primes on the N and M denote that the data are dead time corrected. In general, there is no signal from the sample can (or experimental apparatus) to subtract from the vanadium data because a self-supporting solid V rod is used; however, these terms are retained in Eq. (5.31) for completeness. Here, $P^{inel}(Q)$ is the Placzek correction for inelastically scattered neutrons as discussed in Section 5.3.8.5. Since vanadium is an incoherent scatterer, its differential cross section is just equal to $(d\sigma^v/d\Omega)d\Omega = \langle b_v^2 \rangle$. Therefore, we get

$$DK\varepsilon_d = \left[\left(\frac{N'}{M'}\right)^{vc} - \left(\frac{V'_{c;vca}}{V'_{c;ca}}\right)\left(\frac{N'}{M'}\right)^{c(v)}\right]\left(\frac{1}{V'_{v;vca}\rho^v\left(\langle b_v^2 \rangle + m'_v + P^{inel}_v\right)}\right) \tag{5.32}$$

and the desired

$$\left(\frac{d\sigma^s}{d\Omega}\right) = \frac{\left[\left(\frac{N'}{M'}\right)^{sc} - \left(\frac{V'_{c;sca}}{V'_{c;ca}}\right)\left(\frac{N'}{M'}\right)^{c}\right]}{\left[\left(\frac{N'}{M'}\right)^{vc} - \left(\frac{V'_{c(v);vca}}{V'_{c(v);ca}}\right)\left(\frac{N'}{M'}\right)^{c(v)}\right]}\left(\frac{\left(\langle b_v^2 \rangle + m'_v + P^{inel}_v V'_{v;vca}\rho^v\right)}{V'_{s;sca}\rho^s d\Omega}\right) - m' - P^{inel}. \tag{5.33}$$

As in the case of X-rays, $\rho^s\,d\Omega$ is independent of Q and can be treated as a constant scaling factor that can be varied to give the right asymptotic behavior for $(d\sigma^s/d\Omega)$ and $S(Q)$. However, it should be noted that the common practice of using ρ^s as a parameter in the data analysis for obtaining the correct normalization affects not only the scale of the data but also the V' integrals. It is not a purely multiplicative scale factor and it should retain a value close to the real powder density. This is discussed further in Section A5.4.

5.3.9.   Electron-Specific Data Corrections

As described in Chapter 4, in the most common setup, the electron diffraction experiment uses a 2D CCD detector to collect the data and so many of the initial corrections are similar to the RAPDF experiment, involving integrating the 2D detector images to 1D diffraction patterns before reducing the data to $S(Q)$ and Fourier transforming to get the PDF. To obtain correct Q-values for the pattern, it is important to know accurately the wavelength of the electrons and the camera length. For X-rays, the camera length is simply the distance from the sample to the detector. However, electrons in a TEM traverse a number of magnetic lenses after the sample and before the detector resulting in an effective camera length different from the actual distance. As explained in Section 5.3.7.6, in the RAPDF experiment, the X-ray wavelength is known and the sample-detector distance is determined by measuring a standard sample with known d-spacing and the same approach is taken in the case of electron PDF.

The wavelength, λ, of the electrons depends on the deBroglie relation, $\lambda = h/p$, where h is Planck's constant and p is the relativistic momentum of the electron. The electron is accelerated through a voltage U in the TEM from the electron source that is either a thermionic or a field emission source. This results in an expression for the wavelength

$$\lambda = \frac{h}{\sqrt{2m_e e U}} \frac{1}{1 + eU/2m_e C^2},\tag{5.34}$$

where e and m_e are the charge and rest mass of the electron and c is the speed of light. For the high accelerating voltages used in TEMs, the velocity of the electrons is a significant proportion of the speed of light (e.g., 70% for 200 kV microscope) and the relativistic correction in the second factor is significant. Typical wavelengths are a few picometers, much smaller than for X-ray diffraction experiments in which the wavelengths are 10 times longer in typical RAPDF experiments and 100 times longer using conventional sources such as Cu K_α.

As for the RAPDF experiment, once the wavelength is known accurately, the measurement of the camera length (sometimes called camera constant in the TEM literature) is carried out by measuring a calibration sample of known d-spacing and using this to refine the accurate camera length. A couple of factors make this less straightforward than in the RAPDF case. First, it is difficult to find a good calibration sample. In the X-ray case, a NIST silicon standard reference material (SRM), SRM 640, is often used. It is a carefully prepared sample with no strain and a uniform small, but not too small, particle size. However, in an ePDF experiment, the grains from such a sample are too large for the electron beam to penetrate. Also, the standard correction in RAPDF assumes that the calibrant is a powder, though in principle this need not be the case, and such large grains will give a poor powder average in the small

electron beam. In that case, it is desirable to create a calibration sample with nano-sized grains to overcome these difficulties. The problem then is that the lattice spacing of the sample is poorly determined because of strains introduced in making the sample as well as the effect of nanoparticle size on lattice parameter (Masadeh *et al.*, 2007). In principle, this can be overcome if the lattice parameter of the calibrant sample is measured accurately using X-ray diffraction or xPDF methods. We also note that the National Institute of Standards and Technology of the United States recently released its first nano-sized SRMs, SRM 8011, 8012, and 8013, which are 10, 30, and 60 nm diameter gold nanoparticles in aqueous solution stabilized by citrate. Some tests need to be done to determine if these will make good lattice constant calibration samples in the TEM, which will depend on how easy to use and how beam-stable they are. NIST is also working on other nano-sized reference materials.

The second issue for calibrating camera length in the TEM is that the camera length depends on the current settings of the lens as well as the sample height. For the calibration to work, the measurement of the calibration sample must be transferable to the case of the specimen under study. For the most accurate calibration, it is desirable to mix the calibrant with the sample, so the calibrant is measured under identical conditions as the sample. However, this is rarely a good idea since you are incorporating an impurity into the sample, something that is normally to be avoided. Thus, we would like to have a way of measuring the calibration material separately and then transferring the information to our sample. This can be done if the calibrant is measured with care under identical settings as the sample, in particular, at a standard condenser lens current. An alternative approach is to measure calibration curves of the calibration sample as a function of the relevant measurement variables. In this way, when the diffraction pattern of the sample under study is taken, the measurement settings can be recorded and compared to the calibration curves to obtain an accurate camera length. This approach has been discussed by Kolb *et al.* (2011) in the context of measuring under nonstandard illumination conditions in order to obtain nano-sized beams. As these ePDF measurements are refined in the future, we expect that standard approaches for carrying out these calibrations will become available making them much easier. If the ePDF method catches on, it is also likely that this will be offered as a feature on microscopes and calibration will become quite automated. Finally, we note that if ePDF is being used as a "quick and dirty" batch characterization method, for example, to determine how samples made under different processing conditions vary, and accurate lattice parameters of the sample are not a question, then a more approximate approach for estimating the camera length is appropriate, for example, assuming that your nano sample has approximately the same known lattice parameter as the bulk material and using it as a self-calibrant.

The beam center on the CCD and any nonorthogonality of the detector with respect to the incident beam should be corrected. These corrections are done in precisely the same way as the RAPDF corrections as described in Section 5.3.7.6. A special issue in the TEM case is that the powder rings can become distorted from circular due to the beam-stop becoming electrically charged during the measurement, which creates an electric field that deflects electrons before they reach the CCD. Careful grounding of the beam-stop is desirable to minimize this. This affects mostly the image close to the shadow of the beam-stop, and it is possible as a workaround to mask this part of the image to minimize the effect on the integrated 1D pattern. In future data analysis software packages, there may be corrections incorporated for this effect.

To increase the Q-range of the measurement, it is possible to place the beam center at a corner of the CCD detector. The trade-off is poorer statistics and less powder averaging, but a wider Q-range. Because of the small size of CCD detectors in standard TEMs (typically of the order of 2 cm on the side), this is more relevant than with X-rays. In any case, this does not introduce any special data processing issues.

As with RAPDF measurements, it is common to average multiple exposures to obtain the required statistics without saturating the detector. This may be done at the image stage or after integration; both seem to work well. A background signal should also be subtracted. To a greater extent than the X-ray case, the background contains intensities that are not circularly symmetric, for example, a ghost image of the electron source can sometimes be seen in the diffraction pattern. This is easily removed as part of the background subtraction. It is sometimes helpful for scaling the background intensity to do this subtraction on the raw images rather than the integrated data. Again, in the future, this kind of subtraction may well become automated. Another advantage of averaging multiple images, rather than averaging the 1D patterns, is that the degree of powder averaging in the measurement can be easily assessed visually (or numerically). Samples with very poor powder statistics will give unreliable integrated powder intensities.

The image averaging, background subtraction of images, and integration to a 1D pattern can be carried out using similar image integration software as used for RAPDF measurements, such as Fit2d or powder3D, as described in Section 5.3.7.6. The 1D diffraction pattern is corrected and reduced to $S(Q)$ and Fourier transformed to $G(r)$ using program PDFgetE. This program is based on *ad hoc* data correction methods as used in PDFgetX3. The main difference is that the division by the atomic form-factor must be done using the electron form-factor and not the X-ray form-factor, $f_x(Q)$. The form-factor encodes information about the spatial extent of the scattering potential. In the case of X-rays, the scattering potential is the electron density and the form-factor is the Fourier transform of $\rho_e(r)$ the spherically averaged electron density. For electrons, the scattering potential is the actual electric potential in the vicinity of the atom. This is the potential due to the charge on the nucleus,

screened by the electron density. The electron atomic form-factor, $f_e(Q)$, is thus related to (Cowley, 1992), but not equal to, $f_x(Q)$,

$$f_e(Q) = \frac{m_e e^2}{2h} \left(\frac{Z - f_x(Q)}{Q^2} \right), \qquad (5.35)$$

where Z is the atomic number of the atom. This expression is ill defined at $Q = 0$, but in this limit, the expression (Cowley, 1992)

$$f_e(Q) = 4\pi^2 \frac{m_e e^2}{3h^2} \left(Z \langle r_e^2 \rangle \right) \qquad (5.36)$$

may be used, where $\langle r_e^2 \rangle$ is the mean-square radius of the electronic shell of the atom. The Q-dependence of the electron and X-ray atomic form-factors, normalized to their values at $Q = 0$, is shown in Fig. 5.12. The electron form-factor falls off more quickly initially than the X-ray form-factor with increasing Q.

   This approach has been shown (Abeykoon *et al.*, 2012) to give PDFs from nanoparticles that can be successfully modeled using the known crystal structure of the bulk material and that compare favorably with PDFs from similar materials obtained using X-rays, as shown in Fig. 5.13.

5.3.10. Combining Datasets

This issue has been addressed for data collected with 2D detectors. Here, we discuss merging data from multiple detectors or spectra in tof neutron measurements.
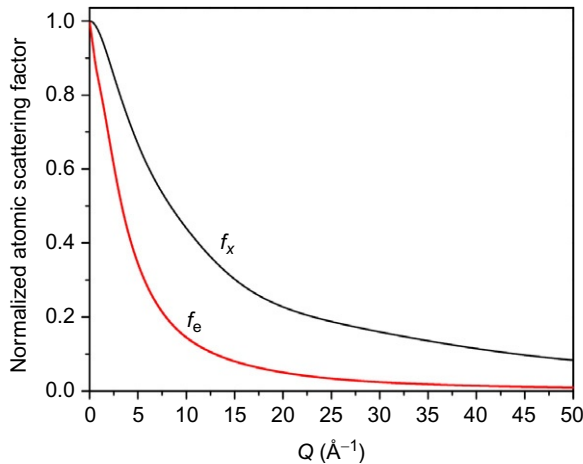

FIGURE 5.12 Comparison of the Q-dependence of the X-ray and electron atomic form-factors. These form-factors have been put on the same scale by setting the value of $f(Q=0)=1$ for both curves. The form-factors shown are for gold.
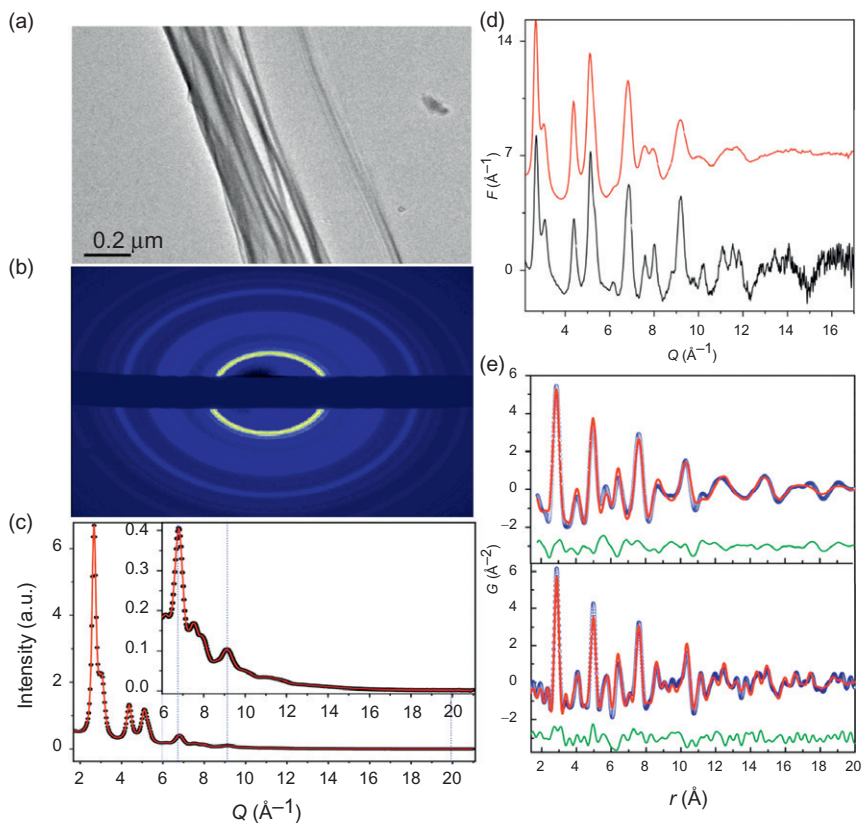
FIGURE 5.13 Example of the ePDF technique. All panels contain data from nanostructured gold. (a) shows a TEM image of the 2.7 nm thick Au film used for ePDF. (b) shows the image of the diffraction pattern obtained in a TEM at an accelerating voltage of 200 keV. (c) is the 1D integrated diffraction pattern, with the inset showing the high-Q region on an expanded scale. (d) shows the reduced structure function obtained from the data in (c). The lower line in (d) is the reduced structure function calculated from an X-ray diffraction experiment performed on Au nanoparticles. (e) shows the best-fit model for the ePDF (top) and the X-ray PDF (bottom). In this case, the thin nanostructured gold film used for the ePDF experiment contained much more disorder than the nanoparticles measured with X-rays. See Abeykoon *et al.* (2012) for details.

The data to be processed often are not contained in a single continuous dataset. It may have originated from more than one detector, or from multiple repeated data runs to improve statistics. If the detector position and solid angle are the same between two measurements, by far, the easiest approach is to combine data at the beginning of the analysis by summing together the dead-time-corrected data at each Q point. The monitor counts from each run should also be summed. This underscores the importance of having a stable monitoring system.

An approach similar to this has been utilized in tof neutron experiments where the detector angles were not identical, but close. In this case, the data from a series of detectors close to the nominal average angle are summed together and the small differences in angle between the detectors are ignored in the subsequent corrections which are computed assuming all the intensity originated from a detector at the average position. Care must be taken to bin together data on the same λ- or Q-grid. Because the tof to Q conversion depends on detector angle, the same Q point will occur at a different tof in each detector. Correcting for this sometimes takes the grand title of "time focusing." It can be done electronically before the data are stored, or using software after data collection.

In general, when the detector solid angle or position is different, the data corrections and normalization are different. In this case, the most precise approach is to propagate the data all the way through to a properly corrected and normalized $S(Q)$ and to combine the $S(Q)$ values to improve the statistics of the compound $S(Q)$. The resolutions of the different detectors also depend on angle and are not included in the corrections described above, so the different $S(Q)$ values will have different resolutions and will cover different regions of Q-space. In this case, it is prudent to make a patchwork so that as wide a range of Q-space is covered but the lower resolution detectors are not contaminating data from higher-resolution detectors. These arguments particularly apply to tof neutron experiments where, also, data from the most intense part of the source spectrum should be used (a rule of thumb is to take the wavelengths $0.2 < \lambda < 2$ Å). At the same time, it is of great importance to obtain sufficient statistics, especially at high-Q, and it is common practice to combine data from as many detectors as possible in this region, keeping in mind the comments above about resolution. When combining the data from normalized $S(Q)$ values, it is important to weight them according to their statistical significance. This is easy if the random errors have been propagated through the data.

Problems arise if the corrected $S(Q)$ functions do not overlap due to imperfect corrections. Small deviations are often ignored and large deviations are handled by not including data banks that are too deviant. In the former case, blending should be done carefully or it introduces noise into the blended $S(Q)$. These issues have not really been adequately addressed up to now (though see Howe *et al.*, 1989). This may change in the future as the next generation of powder diffractometers are expected to yield data in "frames" that are highly fragmented. Correcting and overlapping this kind of data to obtain an undistorted $S(Q)$ will require careful attention to this point. One of the challenges in this regard is to match both the baseline and the integrated intensity of features using additive and multiplicative corrections.

5.3.11. Terminating Data

The Fourier transform to get $G(r)$ from $S(Q)$, Eq. (3.1), involves an integral over Q from zero to infinity. However, the data are only measured over finite

range, $Q_{min} < Q < Q_{max}$. Errors in $G(r)$ due to the finite range of data, so-called termination errors, have been discussed in Section 3.5.2.

The low-Q cutoff rarely presents a problem. Data can usually be measured down to rather low values in Q, so little information is lost, other than the small angle scattering that, according to the definition of $S(Q)$, should not be included anyway. When low-Q Bragg-peaks or coherent diffuse intensity is lost (or mistakenly included as in the case of magnetic scattering), it gives rise to weak long-wavelength oscillations in $G(r)$ (e.g., see Peterson *et al.*, 2003) which add to the residuals in modeling but rarely present a significant problem. As always, the only remedy for this problem is somehow to extend the measurement range to include the missing low-Q information. For example, in tof neutron experiments, missing Bragg-peaks can often be found in the data from very low-angle detectors that otherwise would not be of much interest. When all the low-Q Bragg-peaks are recovered, or methods to extend the measurement are exhausted, it is common practice to take the data at Q_{min} and extrapolate it to zero. This is better than setting the data to zero because, in general, $S(Q)$ asymptotes to the value of $(\langle f^2(0) \rangle - \langle f(0) \rangle^2)/\langle f(0) \rangle^2$ at $Q = 0$. Thijsse (1984) suggests fitting the first 40 or so data points of $Q[S(Q) - 1]$ with a form $c_1 Q + c_2 Q^3$ and extrapolating to zero. This is equivalent to a quadratic dependence of $S(Q)$ at low-Q. Note that this extrapolation scheme (or any other for that matter) relies on the fact that there is no measured coherent scattering at Q_{min} and should not be attempted if Q_{min} lies on top of a low-Q Bragg peak!

As discussed in Section 3.5.2, the high-Q termination results in short-wavelength ripples in $G(r)$. There are a number of ways of artificially reducing these spurious ripples as has been discussed at length. These typically use a method of damping the $S(Q)$ with increasing Q so that the Fourier ringing dies out more quickly in real space (Waser and Schomaker, 1953; Lorch, 1969; Warren, 1990). This always has the effect of reducing the resolution of the resulting $G(r)$ as discussed by Leadbetter and Wright (1972). An alternative is to use an inverse method for carrying out the Fourier transform as we discuss below, though these approaches also have their drawbacks. Fourier transform ripples are not a problem if $S(Q)$ is measured over a sufficiently wide range that the real signal in the data has died out due to Debye–Waller effects and there is really no substitute for taking this approach where possible. The Fourier ripples can also be included when modeling the data.

The term "termination ripples" is often used generally to describe spurious ripples in the Fourier transform. These often result from systematic errors in the processing giving rise to sharp unphysical features at low-r in $G(r)$ that become convoluted with the termination function, Eq. (3.47). This should be distinguished from the narrower but more precise definition above. Clearly, the best way to remove these is to improve the processing to remove the systematic errors. Iterative filtering methods have been proposed to deal with these and they are successful at removing ripples below the first peak (Kaplow *et al.*, 1965; Narayan and Ramaseshan, 1979); however, it is not clear how successful

they are at removing features in the region of real physical interest. Along the same lines approaches where data measured over finite ranges and including systematic errors are "sampled" so that $G(r)$ is only plotted at the nodes of the largest ripples (Lovell *et al.*, 1979). Again, there is no substitute for measuring data over a wide range with good statistics and making good data corrections.

The choice of where to terminate data is made such that Q_{max} is chosen where the signal-to-noise ratio becomes unfavorable. Accepting data to higher Q-values introduces unnecessary statistical noise into the data (which becomes convoluted by the termination function and has the appearance of termination ripples) and terminating lower lowers the resolution of the measurement and results in unnecessarily large termination ripples (i.e., the data themselves are convoluted with the termination function). Note that the termination ripples from the data can be modeled accurately, but the ripples from the correlated statistical errors cannot. The program PDFgetX3 allows an optimal Q_{max} to be determined by varying it using a slider and watching the resulting PDF update in real time in the plot window until the desired result is obtained.

5.3.12. Fourier Transforming the Data

Historically, the most common method of Fourier transforming the data is a straightforward direct numerical transform. However, the latest programs such as PDFgetX3 make use of the fast Fourier transform (FFT) algorithm which dramatically improves performance. The point spacing is in an FFT $\Delta r = \pi/Q_{max}$. It is common practice to evaluate $G(r)$ on a much finer grid than this resulting in smooth and functionally well-defined peaks in $G(r)$. The FFT can still be used with a user-defined fine grid in r-space by padding the pattern in Q with zeros and artificially extending Q_{max}. This does not introduce any additional information, neither does it distort the resulting PDF as discussed in greater detail in Chapter 6 in the context of Nyquist–Shannon sampling theory as applied to the PDF.

Conversely, as we discussed in Section 4.3.5, when measuring the data, the Q-space grid spacing should be less than the measurement resolution. This should also be taken into account when setting the grid (sometimes called quadrature) for the Fourier transform. It results in the criterion $\Delta Q \le \pi/r_{max}$ (Ino, 1957; Leadbetter and Wright, 1972), where r_{max} is a measure of the range in r-space where structural features are evident in $G(r)$. For reasonably high-resolution measurements and crystalline materials, this can be $r_{max} > 300$ Å requiring a grid spacing of $\Delta Q < 0.01$ Å^{-1}.

An interesting alternative approach to the direct Fourier transform is to use an "inverse" method where a $G(r)$ is constructed directly in real space that is consistent with the measured $S(Q)$ but not determined by a direct transform. This can be accomplished using Monte Carlo methods (Soper, 1990; Pusztai and McGreevy, 1997) or using a Maximum Entropy approach (Soper, 1990; Terwilliger, 1994;

Petkov and Danev, 1998). The main drawback to these approaches is philosophical that there is no unique relationship between the measured $S(Q)$ and the resulting $G(r)$. From a practical point of view, the Monte Carlo methods work best if the real space $G(r)$ is calculated to a point where it becomes flat which can be impractically far out in r in the case of crystalline materials. If this criterion is not satisfied, the measured $S(Q)$ has to be convoluted with the Fourier transform of the real-space box being used to determine $G(r)$, thus artificially reducing the resolution of the measurement. This is a somewhat small problem since in practice $G(r)$ is often only modeled over a rather narrow r-range anyway. On the plus side, the resulting PDFs are very clean and free of termination errors.

The maximum entropy method has most utility in cases where the data range is limited, data are unacceptably noisy, or other troublesome systematic errors are present (Petkov and Danev, 1998). Where possible, in such cases where the data are "bad," the best solution is to repeat the measurement taking care of the problems. There is really no substitute for good data.

To summarize, the choice of using a direct or inverse method for determining $G(r)$ from $S(Q)$ remains largely a matter of personal choice. Directly transformed data contain spurious ripples from termination effects that one must guard against misinterpreting. As we discuss in the next chapter, this is less likely when data are modeled over a wider range using physically reasonable models. In addition, it is the actual transformed data that are presented, including all the deficiencies of the measurement such as statistical and systematic errors. This allows a critical assessment to be made by the reader about the quality of the data that gave rise to this $G(r)$. With an inverse transform, the effects of experimental uncertainties, such as termination ripples, instrument resolution function, and inadequacies in the corrections, are removed. On the other hand, the resulting $G(r)$ is not unique and depends on the assumptions and method used to make the inverse transform. In some respect, the uncertainties inherent in making a nonideal measurement (with finite range, statistics, and resolution) that appear as distortions to $G(r)$ in the direct transform have not been removed in the inverse transform but are manifest in the uncertainty about the uniqueness of the resulting $G(r)$. A drawback to the inverse approach is that the resulting $G(r)$ does not reflect the quality and uncertainties of the measurement and it is therefore harder to gauge the quality of a fit with respect to the extent of the errors in the data. In some respect, making an inverse transform amounts to fitting the data in Q-space. Modeling total scattering data directly in real space using the RMC method has been applied with considerable success as we discuss in the next chapter, in which case there is no need to Fourier transform the data at all.

5.3.13.   Instrument Resolution Function

The resolution of a measurement depends on a number of factors such as detector pixel solid angle, incident beam divergence, sample size, diffractometer misalignment, and so on (e.g., see Klug and Alexander, 1968). This has

the effect of broadening features in $S(Q)$ as was discussed in Section 3.5.4. The effects on $G(r)$ are rather mild and the instrument resolution function is often not deconvoluted as part of the data corrections, rather the effects are incorporated into calculated models of the PDF. This is discussed in Chapter 6. Attempts have been made to deconvolute data directly (e.g., see Howells, 1984, 1985; Ida and Toraya, 2002). Also, when fitting Q-space, or carrying out an inverse Fourier transform, the calculated $S(Q)$ can be convoluted with the instrument resolution function before being compared with the data (Howe *et al.*, 1989; Dimitrov *et al.*, 1999).

5.4. REAL-WORLD DATA ANALYSIS

5.4.1. Data Analysis Programs

A large number of programs exist for carrying out data analysis to obtain PDFs from X-ray sources, constant-wavelength neutron sources, and tof neutron sources. An excellent resource for finding out about developments in data analysis is the Journal of Applied Crystallography, a journal of the International Union of Crystallography (IUCr, http://www.iucr.org), where many new developments and new programs are reported. Although strictly speaking, it is intended for discussions about software from the Billinge-group, the online Google group diffpy-users (http://groups.google.com/group/diffpy-users) is also a useful resource where data analysis questions are posted and answered.

Because the number of spallation neutron facilities where tof neutron experiments are carried out is limited, the number of tof neutron codes is also limited. Currently, the two most widely used programs for this purpose are PDFgetN and Gudrun. Gudrun is written by the disordered materials group at Rutherford Appleton Laboratory (RAL) in the UK and is available at (http://www.isis.stfc.ac.uk/instruments/sandals/data-analysis/gudrun8864. html). It makes explicit corrections for modern high areal coverage detector banks, where many detector pixels lie outside the horizontal plane. It has a GUI and the appropriate analysis parameters for the diffractometers at ISIS are preloaded. This feature is available to other diffractometers also (e.g., D4 of ILL is there) and presumably more will be added in the future. PDFgetN is also a GUI-based program (Peterson *et al.*, 2000) that grew out of the IPNS GLASS package but has been considerably extended. It can now analyze data from virtually all of the major tof powder diffractometers in the world. PDFgetN is well documented and easy to use. An example of an analysis carried out using this package is shown in Appendix 5.4. It will run on linux, most unix, and windows platforms and is available free from (http://pdfgetn.sourceforge.net/). PDFgetN has been installed on the NPDF diffractometer at Los Alamos National Laboratory in such a way as to give real-time PDFs during measurement which is a popular feature. Statistical errors are propagated along with the data, and all of the data analysis

parameters used in the data processing are stored as a header in the final PDF file. This is particularly important for a technique like the PDF where the "data" that are used for modeling and extracting structural information are somewhat removed from the raw measured data by processing. Maintaining a quantitative data analysis history in the header of the PDF file facilitates post-facto checking and comparison of a particular PDF.

Historically, there were almost as many X-ray analysis codes as there are groups doing X-ray PDF analysis. However, now this has settled down a bit as more people use PDF to do science rather than develop the method! Popular programs include PDFgetX2, PDFgetX3, PDFgetO, and GudrunX. PDFgetX2 (Qiu *et al.*, 2004), its replacement that uses the *ad hoc* data reduction methods described in Section 5.2.1, and PDFgetX3 (Juhas *et al.*, 2012) are available from http://www.diffpy.org. PDFgetO is an online version of PDFgetX3 that is currently under development. These programs are free for academic research, but a license is required for commercial use. PDFgetX3 and PDFgetO are designed to be quick to learn and easy to use and to handle large numbers of datasets quickly. PDFgetX2 (Qiu *et al.*, 2004) has many corrections implemented and has a graphical user interface with many plots possible for tracking the nature of different intermediate corrections. Like Gudrun, GudrunX is developed by the disordered materials group at RAL and is available from (http://www.isis.stfc.ac.uk/support-laboratories/xrd/data-analysis/xrd-data-analysis9203.html). The program implements many corrections and has a GUI. Both PDFgetX2 and GudrunX require some learning before they can be used properly, which can be accomplished using the documentation and examples included with the program, or better by attending workshops that are given periodically or working initially with an established user. Because of the success of PDFgetX3 at reproducing the results of PDFgetX2, it is unlikely that the program, and workshops to teach its use, will continue to be supported in the future. All these programs can handle Rapid Acquisition PDF data from 2D detectors. There are also less widely used codes that still have their adherents, such as RAD (Petkov, 1989) and IFO which uses a maximum entropy-based algorithm (Petkov and Danev, 1998) for the transform. Two codes for Monte-Carlo Fourier inversion are MCGOFR (Soper, 1990) and MCGR (Pusztai and McGreevy, 1997; Tucker *et al.*, 2001). Another useful and versatile X-ray data preprocessing package is Brian Toby's "Swiss army knife" for diffraction, CMPR (Toby, 2005) (e.g., see the NIST crystallography web-page http://www.ncnr.nist.gov/programs/crystallography/. This web-page also contains a number of useful applications for calculating sample absorption as a function of composition and X-ray energy and also neutron absorption and activation).

5.4.2.   Correction of Large Hydrogen Backgrounds in tof Neutron Measurements

In inelastic neutron scattering, hydrogen is your friend because of its enormous scattering cross section; however, this is not so for diffraction experiments

because the enormous scattering cross section is for incoherent scattering which carries no structural information. As a consequence, the relatively small diffraction intensities are swamped by a huge, featureless, incoherent background. The hydrogen background contributes statistical noise, tends to saturate the detectors, and basically makes diffraction experiments in hydrogenated samples a big pain. Nonetheless, there is a strong motivation for studying hydrogen in materials using neutrons, in biological, molecular, and polymeric systems, and as hydrogen, water, and hydrates in inorganic materials, not least because hydrogen is very difficult to see in X-ray measurements and nanoparticles tend to come covered in it.

Traditionally, the best approach to this problem is to deuterate the samples to the extent possible. Deuterium is chemically identical to hydrogen and has a very small incoherent cross section and a relatively strong coherent scattering cross section. However, deuteration is arduous and often impossible, especially because of the relatively large size of samples used in neutron measurements. Complex hydrogenated liquids are studied at the SANDALS, and now, NIMROD diffractometers at ISIS where these challenges have been met for these kinds of studies. Recently, methods have been developed at the Lujan Center at Los Alamos National Laboratory that allow for correction of hydrogen backgrounds in diffraction experiments from crystals and nanocrystals (Page *et al.*, 2011). The approach very much takes the philosophy of the *ad hoc* corrections described in Section 5.2.1 in the sense that known information asymptotic behavior of the $S(Q)$ function is used to subtract an unknown background from the measured data. As we know from Chapter 3, in the limit as Q goes to zero, $S(Q)$ approaches $(\langle b^2 \rangle - \langle b \rangle^2)/\langle b \rangle^2$, and in the high-$Q$ limit, it approaches unity (when the most commonly used Faber-Ziman normalization is used). $S(Q)$ contains all the coherent scattering including Bragg and diffuse scattering. The main contribution to the diffuse scattering in the high-Q region is single and multiphonon dynamic scattering as described in Section 7.2.2 and Equations (2.17) and (7.27). A well-behaved $S(Q)$ should then look like a series of Bragg-peaks or oscillating diffuse scattering sitting on top of a background that increases smoothly from $(\langle b^2 \rangle - \langle b \rangle^2)/\langle b \rangle^2$ to 1 with a shape that looks like $1 - e^{-i\langle\langle (Q,u)^2 \rangle\rangle}$, (Thorpe *et al.*, 2002) where the exponential is none other than the Debye–Waller factor of the material. If there is a significant incoherent inelastic background, for example, as coming from hydrogen, this appears as an additional contribution to the measured intensity which should be removed before obtaining $S(Q)$. The approach demonstrated in Page *et al.* (2011) is simply to subtract all of the background from the measured signal and then to add back in the phonon background as a smooth curve of the form $1 - e^{-i\langle\langle (Q,u)^2 \rangle\rangle}$. This works for much the same reason that the *ad hoc* methods described in Section 5.2.1 work: the hydrogen background is smoothly varying with no frequency components that lie in the structurally relevant region of the spectrum. The results are very satisfactory (Page *et al.*, 2011) and have been incorporated into recent versions of

PDFgetN, opening the door to more diffraction and PDF work on hydrogenated samples. However, as mentioned previously, care must be taken that the large hydrogen signal is not saturating detectors, in which case it is affecting the structurally relevant information. For this reason, experiments must, in general, be done on smaller samples and counted for much longer to make up for both the smaller sample size and the additional statistical noise that is coming from the hydrogen signal but not removed by the *ad hoc* subtraction. As we discuss in Section 5.4.3, errors should also be correctly propagated to ensure unbiased fits in modeling later on.

5.4.3.   Statistical Uncertainties on PDFs

In science, it is important to report an estimated uncertainty on any measured number, and this is no less true in the case of PDF. The effect of errors in the PDF was introduced in general terms in Section 3.5 and a review of error propagation as applied to the PDF is given in Appendix A5.3. Here, we address a number of issues that have often been overlooked in PDF data analysis, but which are beginning to receive more attention now, related to the statistical correlations of data points.

First a word about counting statistics. Scattering of X-rays, neutrons, and electrons is a stochastic process and subject to quantum fluctuations. The goal of the experiment is to estimate an underlying scattering probability (the $S(Q)$ function, say) by sending in many particles and counting how many come out at each Q-value, then dividing by how many were sent in, thus obtaining an estimate of the scattering probability. As with any stochastic process, such as tossing a coin, the actual number measured is only an estimate of the underlying probability, but the more trials you do, the closer the estimate is to the real value, and for a truly random process the uncertainty, or standard deviation, on the average value is given by $1/\sqrt{N}$, where N is the number of measured counts: for a 1% uncertainty, you need 10,000 counts. The detection of particles is also a stochastic process, and for a particle-counting detector, where the arrival of each particle (e.g., photon in the case of X-rays) is registered as a "count," the correct value of N to take for the uncertainty estimate is the number of detected counts in a pixel after correcting for dead time. The first step taken in data analysis programs such as PDFgetN, PDFgetX2, and Gudrun, after detector dead-time correction, is to create an uncertainty array with one bin for each bin in the data array but containing the corresponding value of the uncertainty, that is, for the ith bin containing N_i counts, the ith bin of the uncertainty array would contain $\sqrt{N_i}$. At each subsequent step in the processing, whatever transformation is applied to the data (e.g., multiplying by an absorption correction), the corresponding transformation is applied to an uncertainty array such that the uncertainties are propagated correctly. There are many books on the subject of propagating errors (Bevington *et al*., 1992; Prince, 1994; Taylor, 1997; Hughes and Hase, 2010; Peralta, 2012).

The propagation of statistical uncertainties (s.u.) through to the PDF was described in Toby and Egami (1992) and Billinge (1992), and some subtleties of this are reproduced in Appendix A5.3. Because all of the processing steps are algorithmic, including the Fourier transform step, it is possible to propagate the errors accurately all the way to the PDF such that each point in the PDF has an associated uncertainty that correctly reflects the uncertainty coming from the statistical fluctuations. However, a complication in the case of the PDF is that points in the PDF are not statistically independent. This means that, although the estimated error on a particular point in the PDF is accurate, if you fit a curve over a number of points, you cannot estimate the uncertainty on the fit parameters by simply adding the correctly weighted uncertainties on each point. To get a correct estimation of the uncertainty on the fit parameters, you should calculate the uncertainties taking into account the statistical correlations between the different points, using Equation A5.3.6. This equation assumes that the covariance terms between the data points in the PDF are known. In principle, it is straightforward to obtain these by properly propagating a full variance–covariance (VC) matrix (see Appendix A5.3 and Toby and Billinge (2004)); though at the time of writing, this is rarely, if ever, done in the PDF world.

Statistical correlation between points in the PDF is introduced by the Fourier Transform step. This is not only widely known but also widely misunderstood. It is often thought that, because each point in the PDF contains data from every point in the $S(Q)$ due to the Fourier transform, every point in the PDF becomes statistically correlated with every other point. In fact, the reality is more subtle than that as discussed in detail in appendix A5.3, and the correlations appear only due to the finite range of the FT and the resulting convolution of $G(r)$ with the FT of the termination function. The result is that neighboring points in the PDF can be highly correlated, but points further apart are often less so (this breaks down when most of the uncertainty in the PDF is coming from a few points in $S(Q)$, as, e.g., if there are a small number of very strong Bragg-peaks). How quickly this correlation falls off depends on Q_{max}: the higher Q_{max} the faster the fall-off. As mentioned, the full VC matrix is rarely, if ever, propagated, which is probably due to a number of reasons. First, a large, memory hogging $M \times M$ (where M is the number of points in the PDF) array must be propagated. Second, and probably more importantly, there is currently no modeling program that can actually take this information and do anything with it. Third, it requires a substantial refactoring of current data analysis codes to implement. All of these issues should be resolved in the future, which is an important step for putting quantitative PDF fitting on a more sound footing.

We can summarize the discussion thus far. First, if uncertainties are known on the raw data, they can be propagated all the way to the PDF. These estimated uncertainties on each point in the PDF are themselves accurate. However, even in the case where points in the diffraction pattern are

statistically independent, points in the PDF that are close together may be significantly statistically correlated. If a model is fit over a range of the PDF, as is common in programs such as PDFgui, uncertainties in the resulting fit parameters will not be accurate unless computed using the full VC matrix following the method described in Appendix A5.3 and Toby and Billinge (2004). At the time of writing, this is rarely, if ever done.

If the uncertainties on the PDF are not well known, as well as *uncertainties in refined parameters* being incorrectly estimated as we described above, there is a possibility that the best-fit *values of the refined parameters themselves* are not being correctly estimated in the fits. The reason is that in a correct least-squares minimization (i.e., when the function being minimized is χ^2 or some variant of it), each point in the fit is weighted by $1/\sigma^2$, where σ is the standard deviation on that point. If the weights are not used, or are incorrect, then a different function than χ^2 is being minimized that will, in general, have a different solution. For example, this effect was shown recently in a careful analysis of the uncertainty estimations from Rietveld refinements (Tian and Billinge, 2011). This is particularly pronounced in a Rietveld refinement because of the massive variation in uncertainty from point to point depending on whether or not the point is on a Bragg peak. In the case of the PDF, the uncertainties are distributed very smoothly between the points (as a result of the Fourier transform). In this case, incorrect weights will not result in refined parameter values being wrong, though the estimated uncertainties on the fit parameters will be incorrect.

One of the key assumptions in the above discussion is that points in $S(Q)$ are statistically independent and uncertainty correlations in the PDF just come from the Fourier transform. This is true in the simplest measurement where a point detector is moved around a sample to obtain the powder pattern. However, these days, this kind of experiment is in the minority. RAPDF measurements using 2D detectors, and tof neutron experiments taking data from multiple pixels arranged in 3D and in time, are more the norm these days. Invariably in these cases, there are interpolation and integration steps that introduce uncertainty correlations between points in the data and it is becoming increasingly important that these are handled correctly. Some tests have been done recently on the effects of these different issues on uncertainties in the PDF for the RAPDF case (Yang and Billinge, 2012). The effects of correlation can be quite important. When 2D data are azimuthally integrated to obtain a 1-D diffraction pattern, there are two different approaches that can be taken. The one that results in the highest resolution 1D powder pattern, and the one implemented in the widely used Fit2D program, is to proportionally assign intensity in a detector pixel into different 2θ or Q bins that it overlaps following a lever rule (i.e., if the pixel is 2/3 in one 1-D bin and 1/3 in the neighboring bin, the bins will get 2/3 and 1/3 of the intensity, respectively). The other way to do the integration is to assume that all the intensity in the pixel goes into a single bin, normally the bin where the pixel center resides.

The important point here is that the second method does not introduce any statistical correlation between bins in the diffraction pattern but the first method does. Yang and Billinge (2012) show that for RAPDF experiments the loss of resolution due to this change in integration algorithm is negligible as long as the beam center is well calibrated (and this can vary slightly from image to image) and there is a significant advantage in the single bin approach. In a similar way, statistical correlations between points may also be introduced every time a dataset is interpolated onto a different grid, for example, when converting from a 2θ to a Q grid. It is therefore strongly recommended to do the 2D–1D integration directly onto a Q-grid (Yang and Billinge, 2012). This approach is taken with the new data-reduction software under development, PDFlive, that also incorporates PDFgetX3 and propagates the full VC matrix. It should be noted that in the use of Fit2D in its default setup, and in the tof neutron data reduction programs, the points in $S(Q)$ are generally statistically correlated to some unknown degree and at the time of writing the full VC is not propagated.

Finally, we note that, in the absence of statistical correlations in $S(Q)$, the best estimates of the uncertainties on refined parameters will be obtained when the data are fit on a grid with the Nyquist–Shannon (Shannon, 1949) sampling frequency. On this sampling grid, neighboring points of the PDF are as far apart in r as they can be without losing information from the original signal, and so the points used in the fit are the least correlated that they can be without introducing aliasing errors (Farrow *et al.*, 2011). This has been explicitly verified recently (Yang and Billinge, 2012).

APPENDIX 5.1.   DATA ANALYSIS EQUATIONS DERIVED

In this appendix, the general equations are derived for the scattering from a sample of finite dimension. These are used in Section 5.3 to determine equations allowing $S(Q)$ to be obtained from a real powder diffraction experiment.

A5.1.1.   Definitions and Things

The definition of the double-differential scattering cross section, $d^2\sigma/(d\Omega dE)$, of a scattering sample is as follows (e.g., see Lovesey, 1984). Let $I_s(\theta, \phi, E_i, E_s, t)$ be the number of scattered particles per second with energy between E_s and $E_s + dE_s$ entering a detector that subtends a solid angle of $d\Omega$ and is positioned at an angle of (θ,ϕ) to the origin where the sample is located. This is illustrated in Fig. A5.1.1. Here, and in the following, the parameters in parentheses, the "argument" of the quantity, indicate what the quantity depends on. For example, in the present case, $I_s(\theta,\phi,E_i,E_s,t)$ depends on the angular position of the detector, (θ,ϕ), on the energy of the incoming and scattered beams, E_i and E_s, respectively, and in general on time, t. Then
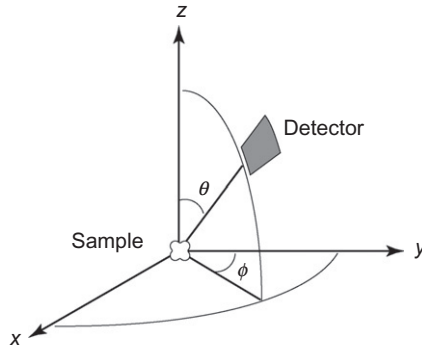
FIGURE A5.1.1   Schematic illustration of the angles used in the definition of the detector solid angle and the definition of the double-differential cross section.

$$I_s(\theta,\phi,E_i,E_s,t) = J(\mathbf{r},E_i,t)\left[\frac{d^2\sigma(\theta,\phi,E_i,E_s)}{d\Omega dE_s}\right]d\Omega dE_s, \qquad (A5.1.1)$$

where J is the number of scattering particles (neutrons or X-rays) per unit area per second impinging on the sample: the incident flux.

From this definition, it is clear that σ has the units of area, and this is the origin of its name: cross section. The cross section contains the structural information from the sample. It gives the probability of a particle (X-ray or neutron) of a particular energy (E_i) being scattered in a particular direction (θ,ϕ) with a particular energy transfer $\Delta E = E_s - E_i$. For example, Bragg scattering is elastic ($\Delta E = 0$ and $E_i = E_s$). Pure elastic scattering can be measured if you have a detector with good energy resolution, dE_s, that is set up in such a way as to measure scattered particles with the same energy as the incident particles. This amounts to integrating the double-differential cross section over the band-pass of the detector, $W(E)$, as discussed in Chapter 7, to yield the differential cross section for our measurement,

$$\frac{d\sigma(\theta,\phi,E_i)}{d\Omega} = \int\frac{d^2\sigma(\theta,\phi,E_i,E_s)}{d\Omega dE_s}W(E_s)dE_s.$$

In the case described here, $W(E_s)$ is a sharply peaked function centered around $E_s = E_i$. The resulting differential cross section contains the pattern of Bragg-peaks from the sample.

The measured intensities depend on this underlying cross section, the structural information of interest. They also depend on experimental parameters such as the incident flux, detector energy resolution, and the detector solid angle (or the angular width of the slits in front of the detector). This highlights the nice feature of this formalism. A real experimental intensity is described (i.e., the number of counts per second into a real detector) in terms of an underlying scattering probability (i.e., the cross section which is the thing we are trying to measure), and some experimental factors

(J, $d\Omega$, E_s). The total scattering structure function, $S(Q)$, depends on the differential scattering cross section according to Eq. (2.8). We will also develop the precise relationship in more detail below. For now, it is sufficient to realize that the objective of the data analysis steps is to recover the coherent single-scattering differential cross section, $d\sigma_s/d\Omega$, from the measured intensity, I_s.

A5.1.2.   Step 1: Single-Scattering Intensity from a Small Volume Element in the Sample

In the definition of the double-differential cross section given above, it was assumed that the sample is small compared to the dimension from the sample to the detector. We then placed the origin of our coordinate system at the sample position. We now want to consider the sample in finer detail. We will define the origin arbitrarily somewhere inside the sample; for example, it could be at the center of mass. We will then consider the scattering from tiny three-dimensional volume elements, $d\mathbf{r} = dxdydz$, located at positions $\mathbf{r}$ away from the origin. This is illustrated in Fig. A5.1.2. Initially, let us consider that our entire sample is just a single volume element. The scattered intensity entering the detector from this sample element will be

$$dI_s(\theta,\phi,E_i,E_s,t,\mathbf{r}) = J(\mathbf{r},E_i,t)\left[\frac{d^2\sigma(\theta,\phi,E_i,E_s)}{d\Omega dE_s}\right]d\Omega dE_s. \qquad (A5.1.2)$$

The incident flux is a function of the position of the scattering element, $\mathbf{r}$, because, in general, the incident beam will not be uniform. However, here, we assume that the sample is uniform and the cross section does not depend on position.

   If this sample element is located at some position inside a macroscopic sample (Fig. A5.1.2), then we have to consider two effects. First is the possibility that a particle being scattered in this volume element at $\mathbf{r}$ has already undergone a scattering event (or more than one) in another volume element(s) in the sample. This is called "multiple scattering" and will be explicitly dealt with in the
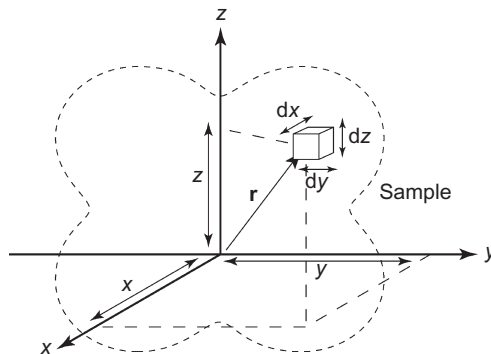

FIGURE A5.1.2   Schematic of the volume element dx, dy, dz at position x, y, z.

next section. In the rest of this section, we consider only the single-scattered intensity, dI_s^1, reaching the detector. The second effect is that the incident beam has first to reach the element and then to emerge from the sample to reach the detector. As the beam traverses the sample, it is attenuated according to $I = I_0 e^{-\mu(E)l}$, where I and I_0 are the attenuated and unattenuated beam intensities, respectively, $\mu(E)$ is the linear attenuation coefficient (often, not strictly correctly, called the linear absorption coefficient) and l is the path length through the sample. In general, the sample is held in a container. There may also be other pieces of experimental apparatus such as heat-shields and furnace elements in the beam. This is illustrated in Fig. A5.1.3. We will refer to these different media as apparatus, container, and sample. We can trace deterministic paths through the sample, container, and apparatus, and the absorption of an X-ray following this path is uniquely specified (see Fig. A5.1.3).

Consider first the absorption of the incident beam before the sample element is reached. The ray travels through a length l_a^i of apparatus that has an absorption coefficient of $\mu_a(E_i)$, l_c^i of sample container with absorption coefficient $\mu_c(E_i)$ and l_s^i of the sample with absorption coefficient $\mu_s(E_i)$. The same set of parameters are generated for the scattered beam with the superscript i replaced with s and E_i replaced with E_s. The intensity of the ray following this path is therefore attenuated by the factor $\exp - \{(\mu_a(E_i)l_a^i + \mu_c(E_i)l_c^i + \mu_s(E_i)l_s^i + \mu_a(E_s)l_a^s + \mu_c(E_s)l_c^s + \mu_s(E_s)l_s^s)\}$. This is a product of attenuation factors, $A_s A_c A_a$, one for each medium; that is,

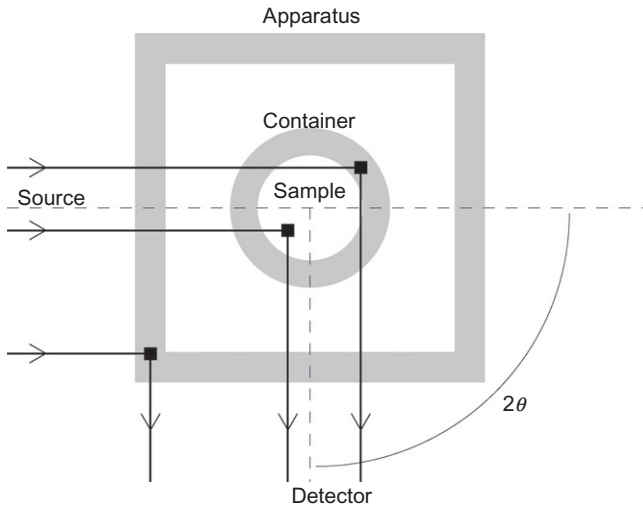$$A_x = \exp\{-\mu_x(E_i)l_x^i + \mu_x(E_s)l_x^s\}, \tag{A5.1.3}$$

FIG. A5.1.3   Schematic cross section of a sample surrounded by sample environments. Some particle tracks through the sample/can/apparatus are shown as the arrowed lines.

where x takes the values a, c, or s. If there are more items of apparatus then the set of values, x can be extended as required and, in general, the intensity reaching the detector is attenuated by the product $\Pi_x A_x(\mathbf{r},\theta,\phi,E_i,E_s)$. The attenuation factors can be evaluated numerically (and sometimes analytically) if the $\mu_x(E)$ coefficients are known for the different media. The μ_x coefficients can be evaluated if the composition and density of the sample are known, or they can be measured directly by carrying out an absorption measurement on a sample of the material of known uniform thickness.

The number of particles per second reaching the detector that were singly scattered in volume element d$\mathbf{r}$ at position $\mathbf{r}$ is therefore given by

$$dI_s^1(\theta,\phi,E_i,E_s,t,\mathbf{r}) = J(\mathbf{r},E_i,t)\left(\frac{d^2\sigma(\theta,\phi,E_i,E_s)}{d\Omega dE_s}\right)$$
$$\left(\Pi_x A_x(\mathbf{r},\theta,\phi,E_i,E_s)\right)d\Omega dE_s. \tag{A5.1.4}$$

Continuing our simulation of the scattering experiment, we have to take into account the efficiency of detection of the scattered particles. Two things affect this. The first, and most obvious, is the quantum efficiency of the detectors themselves, $\varepsilon_d(E_s)$. This is the probability that a scattered particle of energy E_s that is incident on the detector will be detected. The second factor that affects whether a scattered particle is detected comes from the scattered beam collimating optics of the diffractometer. Ideally, these are constructed so that every neutron/X-ray emerging from the sample position is detected and every neutron/X-ray whose scattered path originates away from the sample is not. However, it is clear that this can complicate corrections significantly since it becomes important to know whether a scattering event in part of the apparatus away from the sample position should be included in the corrections or not. This effect can be represented in our scattering expression as a "detector profile" (Soper and Egelstaff, 1980), $D(\mathbf{r},\theta,\phi,E_s)$, which can take values between 0 and 1. If the detector element at position (θ,ϕ) has an unobstructed view of the scattering element at $\mathbf{r}$, then $D(\mathbf{r},\theta,\phi,E_s) = 1$. If the view is completely obstructed, it takes a value 0. In general, it can take any intermediate value. The energy dependence comes about because the absorption of collimator materials is energy dependent. For simplicity later on, we will assume that the sample is small enough that D does not depend on $\mathbf{r}$, the position of the scattering element within the sample.

The expression for the number of particles per second counted in a detector at (θ,ϕ) due to single-scattering events in the volume element d$\mathbf{r}$ at $\mathbf{r}$ is then

$$dI_s^1(\theta,\phi,E_i,E_s,t,\mathbf{r}) = J\left(\frac{d^2\sigma}{d\Omega dE_s}\right)\left(\Pi_x A_x\right)\varepsilon_d D d\Omega dE_s, \tag{A5.1.5}$$

where the explicit position, angle, and energy dependencies of the respective factors have been suppressed for conciseness.

This description of the measured single-scattering intensity from a volume element is very general, and it presents a road-map for how to correct measured intensities to obtain the differential scattering cross section, and therefore obtain $S(Q)$. In the next section we develop a similar expression for multiple-scattering intensity. We will then show how the required scattering cross sections can be recovered from the measured raw intensities from the sample, container, and backgrounds.

A5.1.3.   Step 2: Double and Multiple Scattering from Two Volume Elements in the Sample

We now consider the intensity reaching the detector located at (θ,ϕ) from particles that were scattered twice in the sample/container/apparatus: the double scattering. This is shown schematically in Fig. A5.1.4. The qualitative ideas behind this are very straightforward, but the mathematical equations quickly become dense and complicated. On a first reading, it is recommended that the qualitative ideas behind the multiple-scattering phenomenon are understood by studying Fig. A5.1.4. It is then sufficient to skip to the last paragraph in this section where the magnitude of multiple-scattering effects is discussed. A qualitative understanding of multiple scattering is all that is required to understand the discussion of data corrections in general.

We derive an equation for the double scattering from two volume elements. We consider that the particle is first scattered in the volume element
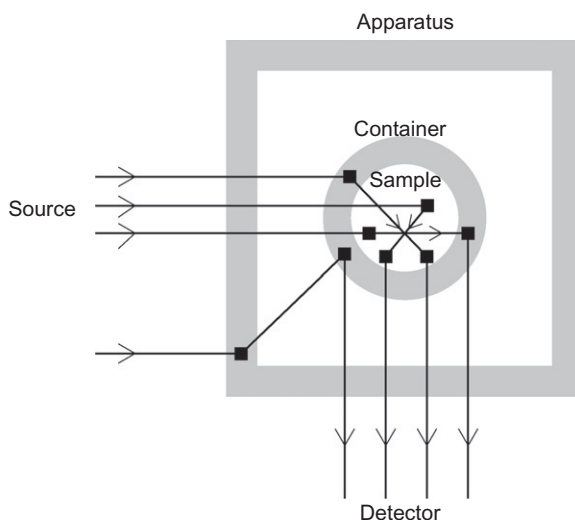

FIGURE A5.1.4   Reproduction of Fig. A5.1.3 but with a number of different multiply scattered particle tracks illustrated.

at $\mathbf{r}_1$ and then subsequently at $\mathbf{r}_2$. The scattered beam from the first event then becomes the incident beam for the second event. It becomes clear that the complexity of the situation increases dramatically because the direction of the incident beam for the secondary scattering event depends on the positions of $\mathbf{r}_1$ and $\mathbf{r}_2$. The angles (θ,ϕ) give the source-sample-detector angle, that is, the global scattering angle. The angle dependence of the scattering cross section refers to the local scattering angle, the angle between the incoming and outgoing beam locally. For single-scattering events, the global and local scattering angles are the same. For higher order scattering, this is no longer the case.

The secondary scattering intensity reaching the detector at (θ,ϕ) can be written as follows:

$$
dI_s^2 = J\left(E_S^0, \mathbf{r}_1\right)\left(\prod_x A_x^0\left(\mathbf{r}, E_S^0\right)\right)\left[\int dE_s^1\left(\frac{d^2\sigma\left(\mathbf{r}_1, E_S^0, E_S^1, P_s^0, \theta', \phi'\right)}{d\Omega dE_s^1}\right)\right.
$$
$$
\times\left(\prod_x A_x^1\left(\mathbf{r}_1, \mathbf{r}_2, E_S^1\right)\right)\left(\frac{d^2\sigma\left(\mathbf{r}_2, E_S^1, E_S^2, P_s^1, \theta'', \phi''\right)}{d\Omega dE_s^2}\right)\right]
$$
$$
\times d\Omega'(\mathbf{r}_2;\mathbf{r}_1)\left(\prod_x A_x^2\left(\mathbf{r}_2, \theta, \phi, E_S^2\right)\right)\varepsilon_d\left(E_S^2\right)D(\mathbf{r}_2)d\Omega dE_s^2. \qquad (A5.1.6)
$$

We now write E_s^n as the energy of the nth scattered radiation, where n takes values 0, 1, and 2. Thus, $E_s^0 = E_i$, and so on. Here, $A_x^n = \exp\{\mu_x(E_s^n)l_x^n\}$ is the absorption factor for the nth scattered beam in medium x. The factor A_x^n depends on the trajectory of the beam and so depends on the relative source-$\mathbf{r}_1$, $\mathbf{r}_1 - \mathbf{r}_2$, and $\mathbf{r}$-detector positions for $n = 0$, 1, and 2, respectively, and $d\Omega'(\mathbf{r}_2;\mathbf{r}_1)$ is the solid angle subtended at $\mathbf{r}_1$ by the volume element $d\mathbf{r}_2$. There is an integral over all energies of the intermediate scattering event because only the initial and final energies of the radiation can be known, for example, by having a monochromatic beam and an energy sensitive detection scheme. Thus, all intermediate scattering events will be recorded at their final energy, regardless of the energy of the intermediate scattering. The equation for dI_s^2 has been written in a, more or less, chronological fashion to aid readability. The flux J is incident on the sample, and this is attenuated by the A_x^0 factors before reaching the first scattering element at $\mathbf{r}_1$ where it is scattered through an angle (θ',ϕ') emerging in a direction toward the second element at $\mathbf{r}_2$ with the probability given by the double-differential cross section of the element at $\mathbf{r}_1$. On its way to $\mathbf{r}_2$, it is attenuated by the A_x^1 factors. These singly scattered particles reaching the second volume element will be scattered through an angle (θ'',ϕ'') with respect to the incoming direction, $\mathbf{r}_2 - \mathbf{r}_1$, emerging in a direction towards the detector with a probability given by the double-differential cross section of the second element. These secondary scattered particles are then attenuated by the A_x^2 factors before reaching the detector and being detected with probability $\varepsilon_d D$. Here, we give the

double-differential cross sections an **r** dependence since, in general, the multiple scattering could occur first in one medium then another.

This seems enormously complicated, and the complications diverge as we go to higher and higher orders of scattering. However, we are dealing with X-rays and neutrons which are weak scatterers. In the case of X-rays, the total multiple-scattering corrections are generally less than 10% of the single-scattering intensity (though we hope to do much better than this!), third and higher order scattering contributes less than 1%. In the case of neutrons, the multiple-scattering corrections are significant and must be carefully corrected. These corrections have been discussed in considerable detail by Sears (1975).

The multiple-scattering intensity represents an annoying background signal in the data. It does not carry useful structural information and must be subtracted from the measured intensity before we can obtain $S(Q)$. The approach is to calculate the multiple-scattering intensity in some reasonable way and then subtract it from the measured intensity. Since the multiple-scattering contributions are small, we can make certain approximations when we calculate them which, even if they give a 10% error on the calculated multiple scattering, result in a $\sim\%$ error on the data. Furthermore, the multiple scattering is quite featureless and changes the shape of $S(Q)$ somewhat but does not interfere with the structural information. In Section 5.3.6, we discussed approaches for calculating the multiple-scattering intensity. Let us assume for now that the multiple-scattering contribution can be evaluated in some reasonable way and proceed with the discussion of how to recover the differential scattering cross section from the measured data.

A5.1.4. Step 3: The Total Single and Multiple-Scattering Intensities Observed in the Detector

The differential scattered intensity expressions, dI_s^n, we have derived up to now give the intensity appearing in a detector due to scattered particles being scattered in specific volume elements and taking a particular trajectory through the sample. The total intensity in the detector will clearly be the integral of the dI_s^n over all possible trajectories.

The total single scattered intensity in a detector at (θ,ϕ) will be $\int dI_s^1$ where the integral is taken over all trajectories through the sample. For the single-scattering case, this amounts to an integral over all volume elements. To do this, it becomes useful to define a double-differential cross section per scatterer,

$$\frac{d^2\sigma'(E_i,E_s,\theta,\phi)}{d\Omega\,dE_s} = \frac{1}{\rho(\mathbf{r})d\mathbf{r}}\frac{d^2\sigma(E_i,E_s,\theta,\phi)}{d\Omega\,dE_s}, \qquad (A5.1.7)$$

where $\rho(\mathbf{r})$ is the number density of scatterers in the volume element of volume $d\mathbf{r} = dx\,dy\,dz$ at position $\mathbf{r}$. This definition for $d^2\sigma'(E_i,E_s,\theta,\phi)d\Omega\,dE_s$ makes sense if we are considering volume elements that are much smaller than the macroscopic sample but larger than the coherence volume of

the scattering. This will typically be a volume containing many thousands of atoms. The total single scattered intensity, I_s^1, detected in a detector of solid angle $d\Omega$ at (θ, ϕ) will then be

$$I_s^1(\theta, \phi, E_i, E_s) = \int dI_s^1 = \int J\left(\frac{d^2\sigma'}{d\Omega dE_s}\right)\left(\prod_x A_x\right)\varepsilon_d D d\Omega dE_s \rho d\mathbf{r}, \qquad (A5.1.8)$$

$$= d\Omega dE_s \varepsilon_d \int J\left(\frac{d^2\sigma'}{d\Omega dE_s}\right)\left(\prod_x A_x\right) D\rho d\mathbf{r}. \qquad (A5.1.9)$$

Similarly, the total double scattering in the detector is given by a double integral over all the volume elements in the sample:

$$I_s^2 = \int_{\text{trajectories}} dI_s^2$$

$$= d\Omega dE_s \varepsilon_d \int d\mathbf{r}_1 \left\{ p(\mathbf{r}_1)J(\mathbf{r}_1)\int d\mathbf{r}_2 \left\{ D(\mathbf{r}_2)\rho(\mathbf{r}_2)\int dE_s^1 \left\{ \left(\frac{d^2\sigma_s\left(\mathbf{r}_1, \theta', \phi', E_s^0, E_s^1\right)}{d\Omega dE_s^1} \right) \right. \right. \right.$$

$$\left. \left. \left. \left(\frac{d^2\sigma_s\left(\mathbf{r}_2, \theta'', \phi'', E_s^1, E_s^2\right)}{d\Omega dE_s^2} \right)\left(\prod_{n=0}^{2} \prod_x A_x^n \right) d\Omega'(\mathbf{r}_1; \mathbf{r}_2) \right\} \right\} \right\}. \qquad (A5.1.10)$$

A5.1.5. Step 4: The Total Measured Intensity in the Detector

The total measured intensity in the detector at position (θ, ϕ) is given by the sum of all the orders of scattering, plus any other sources of counts in the detector other than scattering. These can include such things as fluorescence from the sample, ambient backgrounds not originating from close to the sample, noise in the electronics, and so on. We assume that these latter effects are kept to a minimum in regions of the energy spectrum of practical interest and can be neglected. Thus, the total measured intensity at time t in the detector, I_s^m, is given by

$$I_s^m(\theta, \phi, E_i, E_s, t) = \sum_n I_s^n, \qquad (A5.1.11)$$

where the sum is over all orders of scattering.

A5.1.6. Step 5: Normalizing for the Incident Flux

What is actually measured in the detector is the integrated counts:

$$N(\theta, \phi, E_i, E_s) = \int I_s^m(\theta, \phi, E_i, E_s, t)dt, \qquad (A5.1.12)$$

where the integration is carried out over the elapsed time of the measurement. If desired, the average intensity can be obtained by dividing by the time of the measurement. To obtain the differential scattering cross section, it will be

necessary to normalize the counts by the integrated flux. This is possible if we assume that the beam is stable in position and that the beam inhomogeneities are not time dependent. Thus,

$$J(\mathbf{r},E_i,t) = \bar{J}(t,E_i)h(\mathbf{r},E_i), \qquad (A5.1.13)$$

where $\bar{J}(t,E_i) = I_i(t,E_i)/A$ is the flux averaged over the beam profile of area A. Here, $I_i(t,E_i)$ is the integrated counts per second in the incident beam at time t as measured by the beam monitor. Thus, $h(\mathbf{r},E_i)$ is a dimensionless factor that contains the information about the beam inhomogeneities or beam profile. In this case, $\int I_s^m(\theta,\phi,E_i,E_s,t)dt = \{I_s^m\}' \int I_i(t,E_i)dt$, where $\{I_s^{m'}\}$ is the same as I_s^m (Eqs. A5.1.8–A5.1.10) but with the Js replaced with hs. The integrated flux is generally measured using a beam monitor where the number of counts in the beam monitor, $M(E_i)$, is proportional to the number of particles in the incident beam, integrated over the length of the measurement: $\int I_i(t,E_i)dt = K(E_i)M(E_i)$, where $K(E_i) = 1/\varepsilon_m(E_i)$ is the constant of proportionality and ε_m is the quantum efficiency of the monitoring system. A monitor with a fairly low quantum efficiency is desirable so as not to attenuate the incident beam significantly. Clearly, if the beam is inhomogeneous, it is important that the beam be smaller than the monitor. The measured, flux normalized, counts (really it is the probability of detecting a scattered particle) is then given by

$$n_s^m(\theta,\phi,E_i,E_s) = \frac{N(\theta,\phi,E_i,E_s)}{K(E_i)M(E_i)} = \{I_s^m\}'. \qquad (A5.1.14)$$

The number of counts in the detector, N, and the monitor, M, are known quantities and, therefore, so is $Kn_s^m(\theta,\phi,E_i,E_s)$. In a particular measurement n_S^m may only be known at a single value of E_i (monochromatic incident beam measurement) or at a single value of E_s (analyzer after the sample) or integrated over all values of E_s (detector with no energy resolution). However, in the most general case, $Kn_s^m(\theta,\phi,E_i,E_s)$ is known.

If we consider only the singly scattered counts, from Eq. (A5.1.9), we see that

$$Kn_s^1 = K\{I_s^1\}' = d\Omega dE_s K\varepsilon_d \int h\left(\frac{d^2\sigma'}{d\Omega dE_s}\right)\left(\prod_x A_x\right)D\rho d\mathbf{r}, \qquad (A5.1.15)$$

where n_s^1 denotes the singly-scattered normalized counts in the detector. Referring to Eq. (A5.1.10), it is straightforward to get the respective expression for the double-scattered contribution and, by generalizing this expression, the higher orders of scattering. The total normalized counts in the detector are then given by

$$\frac{N}{M} = K\sum_n n_s^n = Kn_s^1 + K\sum_{n=2}^{\infty} n_s^n. \qquad (A5.1.16)$$

A5.1.7.   The Inverse Problem: Obtaining the Double-Differential Cross Section from Measured Intensities

The measured normalized counts, n_s^m, contain contributions from backgrounds and containers. These contributions can be estimated by making measurements of empty sample containers and the empty apparatus. It is a reasonable approximation to make that the sample, can, and apparatus are each macroscopically homogeneous. In that case, the double-differential scattering cross section and the density from each volume element only depend on the medium in which it is located. The integral over volume elements in Eq. (A5.1.15) can then be split into 3 (or more, as needed) integrals taken over volume elements in each medium. Thus, the single scattering is given by

$$Kn_s^1 = \mathrm{d}\Omega \mathrm{d}E_s K \varepsilon_d \{ p^{s;\{w\}} + p^{c;\{w\}} + p^{a;\{w\}} \}, \tag{A5.1.17}$$

where

$$p^{y;\{w\}} = \int_y h \left(\frac{\mathrm{d}^2\sigma^y}{\mathrm{d}\Omega \mathrm{d}E_s} \right) \left(\prod_{x\in\{w\}} A_x \right) D\rho^y \mathrm{d}\mathbf{r} \left(\frac{\mathrm{d}^2\sigma^y}{\mathrm{d}\Omega \mathrm{d}E_s} \right) \rho^y D \int_y h \left(\prod_{x\in\{w\}} A_x \right) \mathrm{d}\mathbf{r} \tag{A5.1.18}$$

is the contribution to the normalized single-scattering counts from scattering in medium y. Here, and hereafter, for notational simplicity, the primes on the double-differential cross sections have been dropped, but it is understood that the cross sections are normalized per scatterer. The $\{w\}$ in the superscripts and subscripts refers to the set of media which are present in the experiment. In the sample experiment, $\{w\} = \{s, c, a\}$; in the container experiment, $\{w\} = \{c, a\}$ (no sample present); and so on where, as usual, s, c, and a refer to sample, container, and apparatus, respectively. The integral is carried over all volume elements in medium y.

For the case of double scattering, we get

$$p^{xy;\{w\}} = \int_y \mathrm{d}\mathbf{r}_2 \left\{ D\rho^y \int_x \mathrm{d}\mathbf{r}_1 \left\{ \rho^x \int \mathrm{d}E_s^1 \left\{ h \left(\frac{\mathrm{d}^2\sigma^x}{\mathrm{d}\Omega \mathrm{d}E_s^1} \right) \times \left(\frac{\mathrm{d}^2\sigma_s^y}{\mathrm{d}\Omega \mathrm{d}E_s^2} \right) \left(\prod_{n=0}^2 \prod_{x=\{w\}} A_x^n \right) \right\} \mathrm{d}\Omega' \right\} \right\}, \tag{A5.1.19}$$

which is the contribution from scattering first in medium x followed by scattering in medium y. This expression can be generalized to get the higher-order scattering terms, $p^{xyz;abc}$, and so on.

It is readily verified that the total normalized counts in the detectors from the three experiments are then given by

$$\left(\frac{N}{M} \right)^{sca} = \mathrm{d}\Omega \mathrm{d}E_s \times K\varepsilon_d \left[p^{s;sca} + p^{c;sca} + p^{a;sca} + \left\{ \sum_x \sum_y p^{xy;sca} \right\} + \left\{ \sum_{xyz} p^{xyz;sca} \right\} + \cdots \right], \tag{A5.1.20}$$

$$\left(\frac{N}{M}\right)^{\mathrm{ca}} = \mathrm{d}\Omega \, \mathrm{d}E_{\mathrm{s}} K \varepsilon_{\mathrm{d}} \left[p^{\mathrm{c;ca}} + p^{\mathrm{a;ca}} + \left\{ \sum_{x} \sum_{y} p^{xy;\mathrm{ca}} \right\} + \left\{ \sum_{xyz} p^{xyz;\mathrm{ca}} \right\} + \cdots \right],$$

$$\text{(A5.1.21)}$$

$$\left(\frac{N}{M}\right)^{\mathrm{a}} = \mathrm{d}\Omega \, \mathrm{d}E_{\mathrm{s}} K \varepsilon_{\mathrm{d}} [p^{\mathrm{a;a}} + p^{\mathrm{aa;a}} + p^{\mathrm{aaa;a}} + \cdots].$$

$$\text{(A5.1.22)}$$

In Eq. (A5.1.20), x, y, and z can take values of s, c and a, and in Eq. (5.21), x, y and z take values of c and a. The terms in braces are the second and higher orders of scattering.

The three measured intensities give us a set of three simultaneous equations containing three unknowns: the double-differential scattering cross sections $(\mathrm{d}^2\sigma^x/(\mathrm{d}\Omega \, \mathrm{d}E_{\mathrm{s}}))$ with x being s, c, and a. In principle, the remaining parameters in the equations consist of known experimental variables. The equations are, however, implicit equations. There is no way of solving them explicitly to get expressions for $(\mathrm{d}^2\sigma^x/(\mathrm{d}\Omega \, \mathrm{d}E_{\mathrm{s}}))$.

There are really two ways to proceed. The first is to simulate the experiment in a computer using an iterative process. The second is to make some approximations that allow explicit single-scattering cross sections to be calculated. In the first approach, an initial trial is used for the cross sections and the measured intensity calculated. The trial can then be updated and the process repeated. This can then be iterated until the calculated and measured intensities agree. This is a regression method; a kind of refinement method where it is the "experimental data" (the relevant differential cross sections to be precise) being refined against the raw data rather than a model being refined against raw data. The initial trial could be the cross section calculated from a model structure, or it could be the raw data themselves after a rough correction process has been carried out. The advantage of this approach is that the multiple scattering is treated in a self-consistent and accurate way. In practice, this approach is enormously computationally intensive, even with modern high-speed computers, and in most cases is unwarranted; for example, if the multiple scattering is not the largest source of uncertainty in the measurement. As we have discussed, multiple-scattering contributions often contribute less than 10% (and often much less than 10%). In these cases, a less accurate estimation of the multiple scattering (or even no multiple-scattering correction at all!) can give acceptable results. We now continue to discuss in more detail the second approach: an approximate method for extracting the cross section explicitly from the raw data.

A5.1.8.   Approximate Method for Extracting the Sample Scattering Cross Section

We now explore the possibility of making reasonable approximations allowing us to solve the set of Eqs. (A5.1.20)–(A5.1.22) to obtain $(\mathrm{d}^2\sigma^{\mathrm{s}}/(\mathrm{d}\Omega \, \mathrm{d}E_{\mathrm{s}}))$, the double-differential scattering cross section of the sample. First,

we note that in most experiments, all the multiple scattering combined is a minor part of the total measured intensity. If the multiple scattering can be calculated in some reasonable way, then it can be subtracted directly from the data. For now, assume that it can be calculated to acceptable accuracy.

Eqs. (A5.1.20)–(A5.1.22) yield the following expressions for the normalized counts in our detectors from each of the three measurements:

$$\left(\frac{N}{M}\right)^{\text{sca}} = \mathrm{d}\Omega \mathrm{d}E_s K \varepsilon_d \{p^{\text{s;sca}} + p^{\text{c;sca}} + p^{\text{a;sca}} + m^{\text{sca}}\}, \qquad (A5.1.23)$$

$$\left(\frac{N}{M}\right)^{\text{ca}} = \mathrm{d}\Omega \mathrm{d}E_s K \varepsilon_d \{p^{\text{c;ca}} + p^{\text{a;ca}} + m^{\text{ca}}\}, \qquad (A5.1.24)$$

$$\left(\frac{N}{M}\right)^{\text{a}} = \mathrm{d}\Omega \mathrm{d}E_s K \varepsilon_d \{p^{\text{a;a}} + m^{\text{a}}\}, \qquad (A5.1.25)$$

where the $p^{\text{x;}\{w\}}$ is defined in Eq. (A5.1.19). The $m^{\{w\}}$ indicate all of the multiple-scattering contributions which we assume to be adequately calculable.

If we subtract Eq. (A5.1.25) from Eqs. (A5.1.24) and (A5.1.23), we get

$$\left(\frac{N}{M}\right)^{\text{sca}} - \left(\frac{N}{M}\right)^{\text{a}} = \mathrm{d}\Omega \mathrm{d}E_s K \varepsilon_d \{p^{\text{s;sca}} + p^{\text{c;sca}} + (p^{\text{a;sca}} - p^{\text{a;a}}) + (m^{\text{sca}} - m^{\text{a}})\}, \quad (A5.1.26)$$

$$\left(\frac{N}{M}\right)^{\text{ca}} - \left(\frac{N}{M}\right)^{\text{a}} = \mathrm{d}\Omega \mathrm{d}E_s K \varepsilon_d \{p^{\text{c;ca}} + (p^{\text{a;ca}} - p^{\text{a;a}}) + (m^{\text{ca}} - m^{\text{a}})\}. \quad (A5.1.27)$$

Referring to Eq. (A5.1.18), we see that

$$(p^{\text{a;ca}} - p^{\text{a;a}}) = \left(\frac{\mathrm{d}^2\sigma^{\text{a}}}{\mathrm{d}\Omega \mathrm{d}E_s}\right) D\rho^{\text{a}} \int_a h A_a A_c \mathrm{d}\mathbf{r} - \left(\frac{\mathrm{d}^2\sigma^{\text{a}}}{\mathrm{d}\Omega \mathrm{d}E_s}\right) D\rho^{\text{a}} \int_a h A_a \mathrm{d}\mathbf{r},$$

$$= \left(\frac{\mathrm{d}^2\sigma^{\text{a}}}{\mathrm{d}\Omega \mathrm{d}E_s}\right) D\rho^{\text{a}} \left(\int_a h A_a A_c \mathrm{d}\mathbf{r} - \int_a h A_a \mathrm{d}\mathbf{r}\right), \qquad (A5.1.28)$$

$$= \left(\frac{\mathrm{d}^2\sigma^{\text{a}}}{\mathrm{d}\Omega \mathrm{d}E_s}\right) D\rho^{\text{a}} \left(V'_{\text{a;ac}} - V'_{\text{a;a}}\right), \qquad (A5.1.29)$$

where

$$V'_{y;\{w\}} = \int_y h \left(\prod_{x \in \{w\}} A_x\right) \mathrm{d}\mathbf{r} \qquad (A5.1.30)$$

has dimensions of volume and contains all the information about incident beam inhomogeneities and absorption effects. It thus represents the effective scattering volume of the experiment. The absorption factor A_x is defined in Eq. (A5.1.3), and h describes the incident beam inhomogeneities introduced

in Eq. (A5.1.13). Referring to Eq. (A5.1.29), we see that the cancelation would be perfect but for the correction for absorption of intensity scattered in the apparatus but traversing the sample can, A_c. By design, we try to place shields, furnace elements, and so on as far as possible from the sample position. The result of this is that most of the apparatus scattering does not originate from close to the sample position (Fig. A5.1.3). The contribution to the integral $V'_{a;ac}$ of trajectories traversing the sample container should therefore be small, $V'_{a;ac} \approx V'_{a;a}$, and the single scattering from the apparatus cancels. By the same argument, the single scattering from the apparatus will also cancel quite effectively from the sample experiment, Eq. (A5.1.27). Assuming the assumptions are reasonable, Eqs. (A5.1.26) and (A5.1.27) thus become

$$\left(\frac{N}{M}\right)^{\text{sc}} = \left(\frac{\text{N}}{M}\right)^{\text{sca}} - \left(\frac{\text{N}}{M}\right)^{\text{a}} = \text{d}\Omega \text{d}E_s K \varepsilon_{\text{d}} \{p^{\text{s;sca}} + p^{\text{c;sca}} + (m^{\text{sca}} - m^{\text{a}})\},$$

(A5.1.31)

$$\left(\frac{N}{M}\right)^{\text{c}} = \left(\frac{\text{N}}{M}\right)^{\text{ca}} - \left(\frac{\text{N}}{M}\right)^{\text{a}} = \text{d}\Omega \text{d}E_s K \varepsilon_{\text{d}} \{p^{\text{c;ca}} + (m^{\text{ca}} - m^{\text{a}})\}. \qquad \text{(A5.1.32)}$$

Some cancelation will also occur in the multiple scattering. For example, using similar arguments as were used above to justify canceling the single scattering from the apparatus, we see that multiple scattering occurring exclusively in the apparatus will effectively cancel in Eqs. (A5.1.31) and (A5.1.32). This leaves multiple scattering which occurs in the can or which is scattered at least once each in the container and the apparatus. The contribution of these events to the total scattering is expected to be very small.

We now consider what happens when we take the difference between Eqs. (A5.1.31) and (A5.1.32). As before we will get an expression $(p^{\text{c;sca}} - p^{\text{c;ca}})$ that will have the form

$$(p^{\text{c;sca}} - p^{\text{c;ca}}) = \left(\frac{\text{d}^2\sigma^{\text{c}}}{\text{d}\Omega \text{d}E_s}\right) D\rho^{\text{c}} \left\{ \int_c h A_a A_c A_s \text{d}\mathbf{r} - \int_a h A_a A_c \text{d}\mathbf{r} \right\}$$

$$= \left(\frac{\text{d}^2\sigma^{\text{c}}}{\text{d}\Omega \text{d}E_s}\right) D\rho^{\text{c}} \left(V'_{\text{c;sca}} - V'_{\text{c;ca}}\right). \qquad \text{(A5.1.33)}$$

It is now no longer true that these terms nearly cancel out because the absorption by the sample of intensity scattered in the container will be highly significant: $V'_{\text{c;sca}} \neq V'_{\text{c;ca}}$. However, if the effective volume integrals, $V'_{\text{c;\{w\}}}$, can be adequately evaluated, we can get cancelation of the single- scattering intensity from the can by scaling $p^{\text{c;ca}}$ by $V'_{\text{c;sca}}/V'_{\text{c;ca}}$. Thus,

$$\left(\frac{N}{M}\right)^{\text{s}} = \left(\frac{N}{M}\right)^{\text{sc}} - \left(\frac{V'_{\text{c;sca}}}{V'_{\text{c;ca}}}\right)\left(\frac{N}{M}\right)^{\text{c}} = \text{d}\Omega \text{d}E_s K \varepsilon_{\text{d}} \{\rho^{\text{s;sca}} + m'\}, \qquad \text{(A5.1.34)}$$

where

$$m' = \left\{ (m^{\text{sca}} - m^{\text{a}}) - \left(V'_{\text{c;sca}} / V'_{\text{c;ca}} \right) (m^{\text{ca}} - m^{\text{a}}) \right\} \tag{A5.1.35}$$

is the multiple-scattering correction which we, *a priori*, assumed that we could adequately calculate. After subtracting the multiple scattering, we are left with the normalized single-scattering intensity from the sample alone: $d\Omega \, dE_{\text{s}} \, K\varepsilon_{\text{d}} p^{\text{s;sca}}$. The double-differential cross section for the sample is then given by

$$\left(\frac{d^2\sigma^{\text{s}}}{d\Omega dE_{\text{s}}} \right) = \left[\left(\frac{N}{M} \right)^{\text{sc}} - \left(\frac{V'_{\text{c;sca}}}{V'_{\text{c;ca}}} \right) \left(\frac{N}{M} \right)^{\text{c}} \right] \left(\frac{1}{\rho^{\text{s}} V'_{\text{s;sca}} D d\Omega dE_{\text{s}} K\varepsilon_{\text{d}}} \right) - m'. \tag{A5.1.36}$$

The actual measurement is carried out with a detection system of finite energy resolution (or perhaps the double-differential cross section is determined with high-energy resolution, but it is desired to integrate over a finite range of energy transfers). Thus, what is really obtained from the measurement is a differential cross section,

$$\begin{aligned}
\left(\frac{d\sigma^{\text{s}}}{d\Omega} \right) &= \int \left(\frac{d^2\sigma^{\text{s}}}{d\Omega dE_{\text{s}}} \right) W(E_{\text{s}}) dE_{\text{s}} \\
&= \left[\left(\frac{N}{M} \right)^{\text{sc}} - \left(\frac{V'_{\text{c;sca}}}{V'_{\text{c;ca}}} \right) \left(\frac{N}{M} \right)^{\text{c}} \right] \left(\frac{1}{\rho^{\text{s}} V'_{\text{s;sca}} D d\Omega K\varepsilon_{\text{d}}} \right) - m',
\end{aligned} \tag{A5.1.37}$$

where $W(E)$ is the band-pass function of the detector.

APPENDIX 5.2.   ABSORPTION CORRECTIONS IN SOME COMMON GEOMETRIES

A5.2.1.   Summary of Equations in This Appendix

In this appendix, various analytic expressions for the effective sample volume, $V'_{\text{c;\{w\}}}$, introduced in Eq. (A5.1.30) and used in the data analysis equations such as Eq. (A5.1.37), are derived for some specific geometries. For convenience, the derived equations are summarized below.

Reflection geometry:
No support:
$V'_{\text{s;s}}$: general equation: Eq. (A5.2.3)
infinitely thick sample: Eq. (A5.2.4)
symmetric reflection, transparent sample: Eq. (A5.2.5)
symmetric reflection, infinitely thick sample: Eq. (A5.2.6)
Support above and below the sample
$V'_{\text{s;sc}}$: general equation: Eq. (A5.2.7)

infinitely thick sample: Eq. (A5.2.7)
thin or thick sample, symmetric reflection: Eq. (A5.2.8)
thin or thick sample, symmetric and elastic scattering: Eq. (A5.2.9)
$V'_{c;sc}$: general equation: Eq. (A5.2.10)
$V'_{c;c}$: general equation: Eq. (A5.2.11)
$V'_{c;sc}/V'_{c;c}$: general equation: Eq. (A5.2.12)
symmetric reflection: Eq. (A5.2.13)
symmetric reflection, elastic scattering: Eq. (A5.2.14)
symmetric reflection, elastic, infinitely thick sample: Eqs. (A5.2.15) and (A5.2.16)
Transmission geometry:
No support:
$V'_{s;s}$: general equation: Eq. (A5.2.17)
symmetric transmission: Eq. (A5.2.18)
symmetric transmission, elastic scattering: Eq. (A5.2.20)
Support above and below the sample:
$V'_{s;sc}$: general equation: Eq. (A5.2.21)
symmetric transmission: Eq. (A5.2.22)
symmetric transmission, elastic scattering: Eq. (A5.2.23)
$V'_{c;sc}$: general equation: Eq. (A5.2.24)
$V'_{c;c}$: general equation: Eq. (A5.2.25)
$V'_{c;sc}/V'_{c;c}$: general equation: Eq. (A5.2.26)
symmetric transmission: Eq. (A5.2.27)
symmetric transmission, elastic scattering: Eq. (A5.2.28)

A5.2.2.   Attenuation Coefficients

All the equations given here require accurate knowledge of the linear attenuation coefficients $\mu(E)$ for the sample and container. If the sample (powder) density is known, this can be calculated for the case of X-rays using tabulated values for $\mu(E)$ of the different elements. These are generally tabulated as mass absorption coefficients, $\mu_\rho(E)$, (e.g., see probably the most complete and up-to-date compilation at http://physics.nist.gov/xaamdi (Hubbell and Seltzer, 1997)). The mass-attenuation coefficient of a compound can be found from its constituents using simple additivity: $\mu_\rho^s(E) = \Sigma_\alpha w_\alpha \mu_\rho^\alpha(E)$, where $\mu_\rho^\alpha(E)$ is the mass attenuation coefficient of the αth atom and w_α is the fraction by weight of this element, $w_\alpha = c_\alpha M_\alpha/(\Sigma \alpha c_\alpha M_\alpha)$, where c_α and M_α are the concentration and molar mass, respectively. The sample linear absorption coefficient, $\mu^s(E)$, is then obtained by multiplying by the sample (powder) density, $\mu^s(E) = \rho^s \mu_\rho^s(E)$. If possible, it is better to measure the sample attenuation directly by making a flat, uniform sample (in the flat-plate geometries described later the samples already have this geometry). As described in Section 4.3.6, $\mu(E)t$ for the sample can then be measured. The simplest way is to measure the intensity in a detector in the direct beam with the sample,

respectively, in the beam and out of the beam. The flat face of the sample must be perpendicular to the beam. The log of the ratio of the attenuated to unattenuated intensities then gives μt: $\ln(I/I_0) = -\mu t$. Thus, μ for the sample can be obtained by dividing by the sample thickness, t. In the flat-plate geometry equations, μt appears rather than μ, so there is no need to measure the sample thickness, provided the μt measurement was done on the same sample used in the experiment. If the detector used in the absorption measurement is energy resolving, such as a solid-state detector connected to an MCA, then $\mu(E)t$ can be measured for each channel in the MCA by applying the equation $\ln(I(E)/(I_0(E))) = -\mu(E)t$ independently to each channel in the MCA. When you make the measurement, do not destroy the delicate detector with unattenuated direct beam!

A5.2.3.   Absorption: Cylindrical Geometry

Cylindrically symmetric geometry, or so-called Debye–Scherrer geometry, is common in tof neutron measurements and also some X-ray measurements. In this geometry, the sample is held in a cylindrical container (often called a "can") that is placed at the center of the diffractometer perpendicular to the scattering plane defined by the incoming and outgoing beams. It is not generally the geometry of choice for X-ray PDF measurements from divergent sources such as laboratory X-ray sources because of the small sample area that can be illuminated compared to flat-plate geometries. The Debye–Scherrer geometry is popular in powder diffraction for very high Q-space resolution measurements, for example, accurate lattice parameter determinations but is less popular when quantitative intensity measurements are required. However, with the advent of bright synchrotron sources producing small, highly parallel, beams, these considerations become less of a factor. The convenience of the Debye–Scherrer geometry may make it more popular at high-flux synchrotrons in the future. Like laboratory sources, neutron beams tend to be weak and divergent so why is this geometry preferred in tof measurements? The reason is that these instruments have a wide array of detectors filling much of the scattering plane. The cylindrical geometry means that all of the detectors have the same view of the sample; it is the most natural geometry when wide ranges of solid angle are being filled with detectors. For this reason, this geometry will also find use in X-ray cameras using film (e.g., the original Debye–Scherrer cameras) or image-plate detectors, and diffractometers with wide angular range 1D detectors.

   There is no adequate analytic form for the absorption corrections in this geometry and the corrections must be assessed using numerical calculations. The basic approach is the same as was discussed in Appendix A5.1, whereby the sample is split up into volume elements, and the absorption integrals, $V'_{y;\{w\}}$, are determined by summing over all the possible paths through the sample. This procedure is made easier by taking advantage of the symmetry of the situation and the efficiency of the calculation can be greatly improved. This was first

discussed by Paalman and Pings (1962, 1963). As with the discussion of Appendix 5.1, the Paalman and Pings approach yields the effective volume for the singly scattered particles and so the data must be corrected for multiple scattering first. In the original Paalman and Pings papers, and in many subsequent papers on the subject, the absorption corrected effective volume of the sample (or container, etc.), $V'_{y;\{w\}}$, is replaced by the absorption factor $A_{y;\{w\}} = V'_{y;\{w\}} / \int\int h(W,H)\mathrm{d}W\mathrm{d}H$, where the integrations are taken over the width, W, (perpendicular to the scattering plane) and the height, H, (in the scattering plane) of the beam, respectively, incident on the sample and $h(W,H)$ is a measure of the beam inhomogeneities, defined in Eq. (A5.1.13). For a homogeneous beam, h is constant and unity and $\int\int h(W,H)\mathrm{d}W\mathrm{d}H = WH$.

The original Paalman and Pings corrections presumed that the sample was completely bathed in the beam. For beams smaller than the sample diameter, the approach was generalized by Kendig and Pings (1962) and further for inhomogeneous beams by Soper and Egelstaff (1980). This latter paper also describes an approach to carrying out the numerical integration which leads greatly improved computational efficiency without loss of significant accuracy.

A5.2.4.   Absorption: Flat-Plate Reflection Geometry

Absorption corrections for flat-plate reflection geometry can be derived fairly straightforwardly for the approximation of a parallel incident beam. Small corrections are required for a divergent incident beam, though this is rarely necessary given the moderate divergences of normal diffractometers and the small thickness of samples (especially at low X-ray energies). The geometry is shown in Fig. A5.2.1. The incoming beam makes an angle of γ with the sample surface. In the most general case, the scattering is not symmetric and the outgoing beam makes an angle β with the sample surface. The geometry suggests that volume elements should be selected that are parallel to the sample surface with thickness $\mathrm{d}t'$ (see Fig. A5.2.1). We then consider scattering from a volume element at a distance t' below the sample surface. The attenuation of the beam in the sample above the element is $\exp\{-\mu_s(E_i)\ell_i\}$ where $\ell_i = t'/\sin\gamma$ is the path length through the sample before reaching the volume element and $\mu_s(E_i)$ is the linear absorption coefficient of the sample at the energy of the incoming beam. After being scattered, the scattered beam
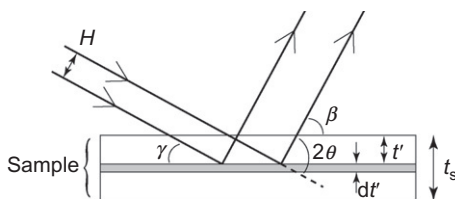

FIG. A5.2.1   Cross section of a flat-plate geometry sample showing incoming and outgoing X-ray beams in reflection geometry. The incoming (outgoing) beam makes an angle $\gamma(\beta)$ with the sample. In Eq. (A5.2.1), we consider the absorption of beams scattered at the planar volume element of thickness $\mathrm{d}t'$ at position t' below the sample surface. The total sample thickness is t_s.

is also attenuated, this time by $\exp\{-\mu_s(E_s)\ell_s\}$, where the absorption coefficient is now that of the sample at the energy, E_s, of the scattered beam that, again in the most general case of inelastic scattering, is different from the incoming beam. Because of the geometry, the integral along the length and the width of the sample simply yield L and W, the length and width of the beam footprint on the sample. The width, W, is simply the beam dimension perpendicular to the scattering plane. The length of the beam footprint, L, depends on the height, H, of the beam (its dimension in the scattering plane) and the incident beam angle, $L = H/\sin\gamma$. Thus, for the case of a sample without any support, we get for the effective sample volume

$$V'_{s;s} = \frac{WH}{\sin\gamma}\int_0^{t_s} \exp\left\{-t'\left(\frac{\mu(E_i)}{\sin\gamma} + \frac{\mu(E_s)}{\sin\beta}\right)\right\}dt'. \qquad (A5.2.1)$$

The integration is carried out over the direction perpendicular to the sample surface from the top surface ($t' = 0$) to the bottom surface ($t' = t_s$) (Fig. A5.2.1). The meaning of the subscripts on the effective volume, $V'_{y;\{w\}}$, is defined in Appendix 5.1 and indicates scattering taking place in medium y in the presence of media in the set $\{w\}$. In this case, we are considering scattering in the sample in the presence of only the sample, $V'_{s;s}$. Eq. (A5.2.1) is straightforwardly generalized to the cases where sample supports need to be considered, as laid out below.

The above expression can easily be generalized to the case where the beam profile, $h(W,H)$ (Appendix 5.1) is inhomogeneous by replacing WH with an effective area

$$(WH)'(\gamma,\beta) = \int\int h(W,H)dWdH. \qquad (A5.2.2)$$

The integration in Eq. (A5.2.1) can be straightforwardly evaluated as

$$V'_{s;s} = \frac{WH}{\sin\gamma}\left(\frac{1}{\left(\frac{\mu_s(E_i)}{\sin\gamma} + \frac{\mu_s(E_s)}{\sin\beta}\right)}\right)\left\{1 - \exp\left\{-t_s\left(\frac{\mu_s(E_i)}{\sin\gamma} + \frac{\mu_s(E_s)}{\sin\beta}\right)\right\}\right\}$$

$$= \frac{WH\sin\beta}{(\mu_s(E_i)\sin\beta + \mu_s(E_s)\sin\gamma)}\left\{1 - \exp\left\{-t_s\left(\frac{\mu_s(E_i)}{\sin\gamma} + \frac{\mu_s(E_s)}{\sin\beta}\right)\right\}\right\},$$

$$(A5.2.3)$$

where t_s is the thickness of the sample. If the sample is infinitely thick (in practice if $\mu t_s > 5$ or so), then

$$V'_{s;s} = \frac{WH\sin\beta}{(\mu_s(E_i)\sin\beta + \mu_s(E_s)\sin\gamma)}. \qquad (A5.2.4)$$

Furthermore, if symmetric reflection geometry is used (i.e., Bragg-Brentano geometry), then $\gamma = \beta = 2\theta/2 = \theta$, where 2θ is the scattering angle, and

$$V'_{s;s} = \frac{WH}{(\mu_s(E_i) + \mu_s(E_s))} \left\{ 1 - \exp \left\{ -\frac{t_s(\mu_s(E_i) + \mu_s(E_s))}{\sin\theta} \right\} \right\}. \qquad (A5.2.5)$$

A very convenient result is obtained in symmetric reflection if the sample is infinitely thick:

$$V'_{s;s} = \frac{WH}{(\mu_s(E_i) + \mu_s(E_s))}, \qquad (A5.2.6)$$

that is, the absorption corrected effective sample volume is independent of scattering angle. This makes the absorption corrections in the case of angle resolved measurements in symmetric flat-plate geometry measurements rather straightforward.

A note of caution is warranted here. The derivation assumes above that the footprint of the incident beam on the sample is smaller than the sample area. In that case, the length of sample illuminated is given by $H/\sin\gamma$. Especially, at small scattering angles, the beam footprint may get bigger than the sample. In this region of the diffraction pattern, $H/\sin\gamma$ should be replaced by l_s, the length of the sample. This adds an additional angle dependence to V'_s. It is then quite important to control the alignment of the diffractometer so that you know precisely where the footprint exceeds the sample size. It may also be possible to measure the very low-angle region of the diffraction pattern in transmission geometry, or asymmetric reflection, and join the low- and high-angle portions of $S(Q)$ before Fourier transforming them. For low energy laboratory measurements in reflection geometry, obtaining agreement between low-angle reflection and transmission measurements has been advocated as a self-consistency check on the quality of the data and corrections (Thijsse, 1984). In practice, for samples and beam heights of reasonable dimensions, the region of $S(Q)$ that is affected is small and at very low Q and errors in the corrections will have a very small effect on the PDF. For example, for a $1\text{-cm} \times 1\text{-cm}$ sample-face and a 1-mm beam height, the footprint exceeds the sample length at $\gamma = 5.7°$ which is a Q-value of 1.8 Å^{-1} for Mo K_α in symmetric reflection. These low-Q data make a small contribution to $G(r)$ because of the $Q/\langle f \rangle^2$ weighting and is rarely missed, except in the most accurate measurements.

Often the sample is supported above and below with a thin tape such as a kapton foil to stabilize it. In this case, the various $V'_{s;w}$ can again be evaluated fairly straightforwardly. These corrections also apply to thick samples ($\mu t_s > 4$ or so) with a thin cover.

We now evaluate $V'_{s;sc}$ the effective volume of the sample in the presence of the foil. The integral is carried out as before in Eq. (A5.2.1) except that the incident beam traverses the foil before reaching the sample. There is, therefore, an additional factor of

$$\exp\left\{-\frac{\mu_c(E_i)t_c}{\sin\gamma}-\frac{\mu_c(E_s)t_c}{\sin\beta}\right\},$$

where $t_c/\sin\gamma$ and $t_c/\sin\beta$ are the path lengths through the foil as the beam enters and exits the sample, respectively. This is shown in Fig. A5.2.2. Thus,

$$
V'_{s;sc}=\frac{WH}{\sin\gamma}\exp\left\{-\left(\frac{\mu_c(E_i)t_c}{\sin\gamma}+\frac{\mu_c(E_s)t_c}{\sin\beta}\right)\right\}\int_0^{t_s}\exp\left\{-t'\left(\frac{\mu_s(E_i)}{\sin\gamma}+\frac{\mu_s(E_s)}{\sin\beta}\right)\right\}dt'
$$

$$
=\frac{WH\sin\beta}{(\mu_s(E_i)\sin\beta+\mu_s(E_s)\sin\gamma)}\exp\left\{-\left(\frac{\mu_c(E_i)t_c}{\sin\gamma}+\frac{\mu_c(E_s)t_c}{\sin\beta}\right)\right\}
$$

$$
\times\left[1-\exp\left\{-\left(\frac{\mu_s(E_i)t_s}{\sin\gamma}+\frac{\mu_s(E_s)t_s}{\sin\beta}\right)\right\}\right].
$$

(A5.2.7)

In all these equations, $\mu_c t_c$ is the absorption coefficient of the Kapton foil (or whatever the sample cover is) that can be readily measured. The result is exactly the same for the thick sample covered by a thin cover since in both cases the beam scattered from the sample never sees the back tape.

In the case of symmetric reflection, Eq. (A5.2.7) reduces to

$$
V'_{s;sc}=\frac{WH}{(\mu_s(E_i)+\mu_s(E_s))}\exp\left\{-\left(\frac{\mu_c(E_i)t_c+\mu_c(E_s)t_c}{\sin\theta}\right)\right\}
$$

$$
\times\left\{1-\exp\left\{-\frac{t_s(\mu_s(E_i)+\mu_s(E_s))}{\sin\theta}\right\}\right\},
$$

(A5.2.8)

and for symmetric geometry and elastic scattering, it reduces to

$$
V'_{s;sc}=\frac{WH}{2\mu_s(E)}\exp\left\{-\left(\frac{2\mu_c(E)t_c}{\sin\theta}\right)\right\}\left\{1-\exp\left\{-\frac{2\mu_s(E)t_s}{\sin\theta}\right\}\right\}.
$$
   (A5.2.9)

Similarly, the effective volumes of the scattering from the foils, with and without the sample, can be obtained analytically. $V'_{c;sc}$ is straightforward but
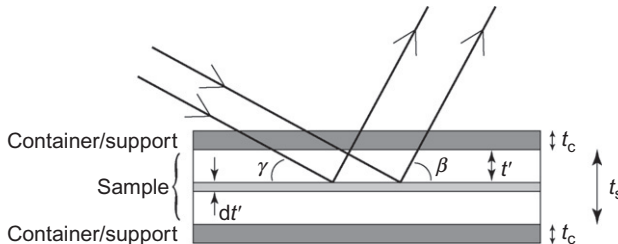

FIGURE A5.2.2   As Fig. A5.2.1 but for the case of scattering in the sample when the sample is supported above and below by a support such as kapton foil.
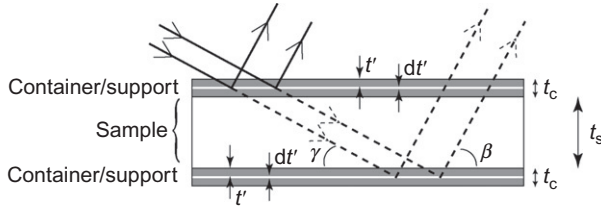
FIGURE A5.2.3   As Fig. A5.2.2 for the case of a supported sample in reflection geometry, but showing the case of scattering occurring within the support.

somewhat complicated. In this case, we can consider two independent contributions to the intensity contributing to V': scattering from the top foil and scattering from the bottom foil. The contribution from the top foil is the same as $V'_{s;s}$ with the t_s replaced by t_c. This is shown in Fig. A5.2.3. The contribution from the bottom foil is like a reflection experiment on a transparent sample with a cover that is the top foil and the sample. The resulting expression gives

$$
\begin{aligned}
V'_{c;sc} = \frac{WH}{\sin\gamma} & \left\{ \int_0^{t_c} \exp\left\{ -t'\left(\frac{\mu_c(E_i)}{\sin\gamma} + \frac{\mu_c(E_s)}{\sin\beta} \right) \right\} dt' \right. \\
& + \exp\left\{ -\left(\frac{\mu_c(E_i)t_c + \mu_s(E_i)t_s}{\sin\gamma} + \frac{\mu_s(E_s)t_s + \mu_c(E_s)t_c}{\sin\beta} \right) \right\} \\
& \left. \times \int_0^{t_c} \exp\left\{ -t'\left(\frac{\mu_c(E_i)}{\sin\gamma} + \frac{\mu_c(E_s)}{\sin\beta} \right) \right\} dt' \right\} \\
= \frac{WH\sin\beta}{(\mu_c(E_i)\sin\beta + \mu_c(E_s)\sin\gamma)} & \left[1 - \exp\left\{ -t_c\left(\frac{\mu_c(E_i)}{\sin\gamma} + \frac{\mu_c(E_s)}{\sin\beta} \right) \right\} \right] \\
& \times \left[1 + \exp\left\{ -\left(\frac{\mu_c(E_i)t_c + \mu_s(E_i)t_s}{\sin\gamma} + \frac{\mu_s(E_s)t_s + \mu_c(E_s)t_c}{\sin\beta} \right) \right\} \right].
\end{aligned}
$$

(A5.2.10)

For the experiment with the top and bottom foils present in the absence of a sample between, the effective volume is the same as given in Eq. (A5.2.10) but without the beam traversing the sample. Thus we get

$$
\begin{aligned}
V'_{c;c} = \frac{WH\sin\beta}{(\mu_c(E_i)\sin\beta + \mu_c(E_s)\sin\gamma)} & \left[1 - \exp\left\{ -t_c\left(\frac{\mu_c(E_i)}{\sin\gamma} + \frac{\mu_c(E_s)}{\sin\beta} \right) \right\} \right] \\
& \times \left[1 + \exp\left\{ -\left(\frac{\mu_c(E_i)t_c}{\sin\gamma} + \frac{\mu_c(E_s)t_c}{\sin\beta} \right) \right\} \right].
\end{aligned}
$$

(A5.2.11)

Thus, the desired effective volume ratio is

$$\frac{V'_{c;sc}}{V'_{c;c}} = \frac{\left[1 + \exp\left\{-\left(\frac{\mu_c(E_i)t_c + \mu_s(E_i)t_s}{\sin\gamma} + \frac{\mu_s(E_s)t_s + \mu_c(E_s)t_c}{\sin\beta}\right)\right\}\right]}{\left[1 + \exp\left\{-\left(\frac{\mu_c(E_i)t_c}{\sin\gamma} + \frac{\mu_c(E_s)t_c}{\sin\beta}\right)\right\}\right]}. \tag{A5.2.12}$$

For symmetric reflection, this reduces to

$$\frac{V'_{c;sc}}{V'_{c;c}} = \frac{\left[1 + \exp\left\{-\left(\frac{\mu_c(E_i)t_c + \mu_s(E_i)t_s + \mu_s(E_s)t_s + \mu_c(E_s)t_c}{\sin\theta}\right)\right\}\right]}{\left[1 + \exp\left\{-\left(\frac{\mu_c(E_i)t_c + \mu_c(E_s)t_c}{\sin\theta}\right)\right\}\right]}, \tag{A5.2.13}$$

and symmetric reflection and elastic scattering

$$\frac{V'_{c;sc}}{V'_{c;c}} = \frac{\left[1 + \exp\left\{-\left(\frac{2\mu_c(E)t_c + 2\mu_s(E)t_s}{\sin\theta}\right)\right\}\right]}{\left[1 + \exp\left\{-\left(\frac{2\mu_c(E)t_c}{\sin\theta}\right)\right\}\right]}. \tag{A5.2.14}$$

Note that in the case where the sample is infinitely thick and there is no scattering from the back support then Eq. (A5.2.14) reduces to

$$\frac{V'_{c;sc}}{V'_{c;c}} = \frac{1}{\left[1 + \exp\left\{-\left(\frac{2\mu_c(E)t_c}{\sin\theta}\right)\right\}\right]}. \tag{A5.2.15}$$

In this situation, the ratio

$$\frac{V'_{c;sc}}{V'_{c;c}} = 1 \tag{A5.2.16}$$

should be used instead if, during the background run, only the scattering from the foil covering the sample is measured and any support under the sample is not measured.

A5.2.5. Absorption: Flat-Plate Transmission Geometry

In this case, the geometry is similar to flat-plate reflection and so the construction of the integrals is also very similar. However, this time, the beam exits out of the back of the sample and so the length of the scattered beam-path is $(t_s - t')/\sin\beta$ instead of $t'/\sin\beta$ for the case of reflection. This is shown in Fig. A5.2.4. Also, in this geometry, the scattering angle, $2\theta = \pi - (\gamma + \beta)$ instead of $2\theta = \gamma + \beta$ in the case of reflection. Making these substitutions, we find that

$$V'_{s;s} = \frac{WH}{\sin\gamma}\exp\left\{-\frac{t_s\mu_s(E_s)}{\sin\beta}\right\}\int_0^{t_s}\exp\left\{-t'\left(\frac{\mu_s(E_i)}{\sin\gamma} - \frac{\mu_s(E_s)}{\sin\beta}\right)\right\}dt'$$

$$= \left(\frac{WH\sin\beta}{(\mu_s(E_i)\sin\beta - \mu_s(E_s)\sin\gamma)}\right)\left\{\exp\left\{-\frac{t_s\mu_s(E_s)}{\sin\beta}\right\} - \exp\left\{-\frac{t_s\mu_s(E_i)}{\sin\gamma}\right\}\right\}. \tag{A5.2.17}$$
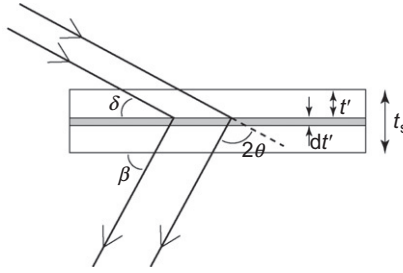
FIGURE A5.2.4   As Fig. A5.2.1 for the case of scattering from an unsupported flat-plate sample in transmission geometry.

In symmetric transmission geometry, we can take advantage of the fact that $\sin \gamma = \sin \beta = \cos \theta$ and we get

$$V'_{s;s} = \left(\frac{WH}{(\mu_s(E_i) - \mu_s(E_s))}\right) \left\{ \exp\left\{-\frac{t_s \mu_s(E_s)}{\cos \theta}\right\} - \exp\left\{-\frac{t_s \mu_s(E_i)}{\cos \theta}\right\} \right\}.$$

(A5.2.18)

In the case of elastic scattering, this is singular. In this case, we can define $\bar{\mu} = \mu(E_s) - \Delta\mu = \mu(E_i) + \Delta\mu$ and take the limit of $\Delta\mu \to 0$. We get

$$V'_{s;s} = \left(\frac{2WH}{\Delta\mu}\right) \exp\left\{-\frac{t_s \bar{\mu}_s}{\cos \theta}\right\} \sinh\left(\frac{t_s \Delta\mu_s}{2\cos \theta}\right),$$

(A5.2.19)

and expanding the $\sin h$ and taking the first term, we arrive at

$$V'_{s;s} = \left(\frac{WHt_s}{\cos \theta}\right) \exp\left\{-\frac{t_s \mu(E)}{\cos \theta}\right\}.$$

(A5.2.20)

If the sample has a supporting structure above and below it (kapton tape, e.g., see Fig. A5.2.5), the equations are modified by the fact that the incoming and outgoing beams traverse the foils. Thus,

$$
\begin{aligned}
V'_{s;sc} &= \frac{WH}{\sin \gamma} \exp\left\{-\left(\frac{t_c \mu_c(E_i)}{\sin \gamma} + \frac{t_c \mu_c(E_s)}{\sin \beta}\right)\right\} \exp\left\{-\frac{t_s \mu_s(E_s)}{\sin \beta}\right\} \\
&\quad \times \int_0^{t_s} \exp\left\{-t'\left(\frac{\mu_s(E_i)}{\sin \gamma} - \frac{\mu_s(E_s)}{\sin \beta}\right)\right\} dt' \\
&= \left(\frac{WH \sin \beta}{(\mu_s(E_i)\sin \beta - \mu_s(E_s)\sin \gamma)}\right) \exp\left\{-\left(\frac{t_c \mu_c(E_i)}{\sin \gamma} + \frac{t_c \mu_c(E_s)}{\sin \beta}\right)\right\} \\
&\quad \times \left\{ \exp\left\{-\frac{t_s \mu_s(E_s)}{\sin \beta}\right\} - \exp\left\{-\frac{t_s \mu_s(E_i)}{\sin \gamma}\right\} \right\}.
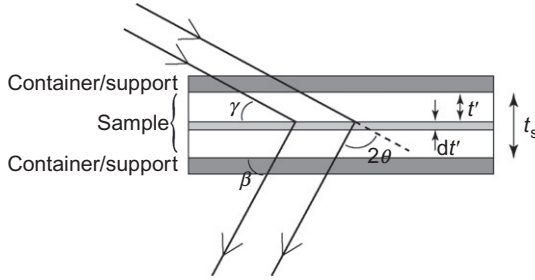\end{aligned}
$$

(A5.2.21)

FIG. A5.2.5   As Fig. A5.2.4 for the case of a sample supported by foils above and below.

For the case of symmetric scattering,

$$
V'_{\text{s;sc}} = \left(\frac{WH}{\mu_{\text{s}}(E_{\text{i}}) - \mu_{\text{s}}(E_{\text{s}})}\right) \exp\left\{-\left(\frac{t_{\text{c}}(\mu_{\text{c}}(E_{\text{i}}) + \mu_{\text{c}}(E_{\text{s}}))}{\cos\theta}\right)\right\}
$$
$$
\times \left[\exp\left\{-\frac{t_{\text{s}}\mu_{\text{s}}(E_{\text{s}})}{\cos\theta}\right\} - \exp\left\{-\frac{t_{\text{s}}\mu_{\text{s}}(E_{\text{i}})}{\cos\theta}\right\}\right],
$$

(A5.2.22)

and for symmetric and elastic scattering,

$$
V'_{\text{s;sc}} = \left(\frac{WHt_{\text{s}}}{\cos\theta}\right) \exp\left\{-\left(\frac{2\mu_{\text{c}}(E_0)t_{\text{c}} + \mu_{\text{s}}(E_0)t_{\text{s}}}{\cos\theta}\right)\right\}.
$$

(A5.2.23)

The effective volumes for the scattering from the support with and without the sample can also be evaluated. $V'_{\text{c;sc}}$ has two contributions; from the front and the back foil, both attenuated by the beam traversing the sample and the other foil:

$$
V'_{\text{c;sc}} = \frac{WH}{\sin\gamma} \exp\left\{-\left(\frac{\mu_{\text{c}}(E_{\text{i}})t_{\text{c}} + \mu_{\text{s}}(E_{\text{i}})t_{\text{s}}}{\sin\gamma}\right)\right\} \exp\left\{-\left(\frac{\mu_{\text{c}}(E_{\text{s}})t_{\text{c}}}{\sin\beta}\right)\right\}
$$
$$
\times \int_0^{t_{\text{s}}} \exp\left\{-t'\left(\frac{\mu_{\text{c}}(E_{\text{i}})}{\sin\gamma} - \frac{\mu_{\text{c}}(E_{\text{s}})}{\sin\beta}\right)\right\} dt' + \frac{WH}{\sin\gamma} \exp\left\{-\left(\frac{\mu_{\text{c}}(E_{\text{s}})t_{\text{c}} + \mu_{\text{s}}(E_{\text{s}})t_{\text{s}}}{\sin\beta}\right)\right\}
$$
$$
\times \exp\left\{-\left(\frac{\mu_{\text{c}}(E_{\text{s}})t_{\text{c}}}{\sin\beta}\right)\right\} \int_0^{t_{\text{s}}} \exp\left\{-t'\left(\frac{\mu_{\text{c}}(E_{\text{i}})}{\sin\gamma} - \frac{\mu_{\text{c}}(E_{\text{s}})}{\sin\beta}\right)\right\} dt'
$$
$$
= \left(\frac{WH\sin\beta}{(\mu_{\text{s}}(Ei)\sin\beta - \mu_{\text{s}}(E_{\text{s}})\sin\gamma)}\right) \left[\exp\left\{-\left(\frac{\mu_{\text{c}}(E_{\text{i}})t_{\text{c}} + \mu_{\text{s}}(E_{\text{i}})t_{\text{s}}}{\sin\gamma}\right)\right\}\right.
$$
$$
\left. + \exp\left\{-\left(\frac{\mu_{\text{c}}(E_{\text{s}})t_{\text{c}} + \mu_{\text{s}}(E_{\text{s}})t_{\text{s}}}{\sin\beta}\right)\right\}\right] \left\{\exp\left\{-\frac{t_{\text{c}}\mu_{\text{c}}(E_{\text{s}})}{\sin\beta}\right\} - \exp\left\{\frac{t_{\text{c}}\mu_{\text{c}}(E_{\text{i}})}{\sin\gamma}\right\}\right\}.
$$

(A5.2.24)

The result for scattering from the two foils without the sample gives the same result but without the beam traversing the sample, thus,

$$V'_{c;c} = \left(\frac{WH \sin \beta}{(\mu_s(E_i) \sin \beta - \mu_s(E_s) \sin \gamma)} \right)$$

$$\times \left[\exp\left\{ -\left(\frac{\mu_c(E_i)t_c}{\sin \gamma} \right) \right\} + \exp\left\{ -\left(\frac{\mu_c(E_s)t_c}{\sin \beta} \right) \right\} \right]$$

$$\times \left\{ \exp\left\{ -\frac{t_c \mu_c(E_s)}{\sin \beta} \right\} - \exp\left\{ -\frac{t_c \mu_c(E_i)}{\sin \gamma} \right\} \right\}.$$

(A5.2.25)

The desired ratio, $V'_{c;sc}/V'_{c;c}$, is then

$$\frac{V'_{c;sc}}{V'_{c;c}} = \frac{\left[\exp\left\{ -\left(\frac{\mu_c(E_i)t_c + \mu_s(E_i)t_s}{\sin \gamma} \right) \right\} + \exp\left\{ -\left(\frac{\mu_c(E_s)t_c + \mu_s(E_s)t_s}{\sin \beta} \right) \right\} \right]}{\left[\exp\left\{ -\left(\frac{\mu_c(E_i)t_c}{\sin \gamma} \right) \right\} + \exp\left\{ -\left(\frac{\mu_c(E_s)t_c}{\sin \beta} \right) \right\} \right]}.$$

(A5.2.26)

For the case of symmetric scattering, this becomes

$$\frac{V'_{c;sc}}{V'_{c;c}} = \frac{\left[\exp\left\{ -\left(\frac{\mu_c(E_i)t_c + \mu_s(E_i)t_s}{\cos \theta} \right) \right\} + \exp\left\{ -\left(\frac{\mu_c(E_s)t_c + \mu_s(E_s)t_s}{\cos \theta} \right) \right\} \right]}{\left[\exp\left\{ -\left(\frac{\mu_c(E_i)t_c}{\cos \theta} \right) \right\} + \exp\left\{ -\left(\frac{\mu_c(E_s)t_c}{\cos \theta} \right) \right\} \right]},$$

(A5.2.27)

and for symmetric elastic scattering

$$\frac{V'_{c;sc}}{V'_{c;c}} = \exp\left\{ -\left(\frac{\mu_s(E_0)t_s}{\cos \theta} \right) \right\}.$$

(A5.2.28)

APPENDIX 5.3. PROPAGATING RANDOM ERRORS IN THE DATA ANALYSIS

We briefly summarize some pertinent ideas of the error propagation here. More details and derivations of the general equations of error propagation presented here can be found in standard textbooks on the subject such as Prince (1982).

The variance of a stochastic variable, X, is defined as

$$\text{var}(X) = \left\langle (X - \langle X \rangle)^2 \right\rangle,$$

(A5.3.1)

where the angle brackets imply taking an average over multiple (unbiased) measurements of that variable. The variance is therefore the mean-square deviation of a series of measurements from the average value. The standard deviation is the root-mean-square variation,

$$\sigma(X) = \sqrt{\text{var}(X)}.$$

(A5.3.2)

In the case of our scattering experiment, the statistics are Poissonian: the variance on the number of counts is simply the number of counts itself and $\sigma = N$.

The covariance of two measurements, X and Y, is a measure of how much the uncertainty of one measurement depends on the result of the other and is defined as

$$\mathrm{cov}(X,Y) = \langle (X - \langle X \rangle)(Y - \langle Y \rangle) \rangle. \tag{A5.3.3}$$

Two measurements that are statistically independent will have a covariance of zero, otherwise the measurements are considered to be statistically correlated. A dimensionless correlation coefficient can be defined as

$$\rho(X,Y) = \frac{\mathrm{cov}(X,Y)}{\sigma(X)\sigma(Y)}, \tag{A5.3.4}$$

which ranges from zero for statistical independence and values of $\pm$ for complete correlation or anticorrelation.

Statistical dependence should be differentiated from functional dependence. Even when two observables are functionally dependent, measurements of these observables can still be made that are statistically independent (as is often done when the functional dependence is being measured or verified). The notion of covariance will become important later in the discussion of error propagation.

What is the variance on a quantity, F, that depends linearly on two stochastic variables X and Y, that is, $F = aX + bY$? Then,

$$\mathrm{var}(F) = a^2\,\mathrm{var}(X) + b^2\,\mathrm{var}(Y) + 2ab\,\mathrm{cov}(X,Y). \tag{A5.3.5}$$

This can easily be generalized to the case of more than two variables. This expression for finding the variance of a quantity that is a function of one or more stochastic observables can be extended to cases where the relationship is not linear in the case where the errors are small ($\sigma(F)/F << 1$). If F is some function of P observables $X_1\ldots X_P$, then

$$\mathrm{var}(F) = \sum_{i=1}^{P}\left(\frac{\partial F}{\partial X_i}\right)^2 \mathrm{var}(X_i) + 2\sum_{i,j=1(i<j)}^{P}\left(\frac{\partial F}{\partial X_i}\right)\left(\frac{\partial F}{\partial X_j}\right)\mathrm{cov}(X_i,X_j). \tag{A5.3.6}$$

If the measurements of the observables are statistically independent, then only the first sum is required.

This equation results in the simple, well-known, results that for $F = aX$,

$$\sigma(F) = a\sigma(X), \tag{A5.3.7}$$

and for $F = aXY$ that

$$\frac{\sigma(F)}{F} = \frac{\sigma(X)}{X} + \frac{\sigma(Y)}{Y}, \tag{A5.3.8}$$

if X and Y are statistically independent.

With this knowledge in hand, it is straightforward to propagate errors in the data correction procedure. Let us say that the number of detected particles in a particular data point is N_d. The detection process is random and so the uncertainty on the number of detected particles is $\sqrt{N_d}$. We thus create two

arrays: a data array which contains the set of counts, N_d, for each measured point, and an error array which contains $\sqrt{N_d}$. These two arrays are then propagated side by side through the data analysis steps. Whenever the data array is modified by a correction, the error array is also properly modified according to Eq. (A5.3.6). Because we are using $\sqrt{N_d}$ as the initial estimate for our errors, often the detector dark-current and dead-time corrections are made before the error array is created. The reason is that the detector dead time introduces an inefficiency in detection which is not random (it is highly correlated: it depends on how closely spaced in time the photons arrive). On the other hand, the dead-time corrected counts will obey Poisson statistics because the underlying scattering and detection processes are random.

A reasonable starting assumption is that all the data points are statistically independent. This is certainly true if a single detector is scanned through space and the data measured point by point. This means that all the covariance terms in Eq. (A5.3.6) are zero. This remains true right up to the Fourier transformation step in the analysis, provided no smoothing or interpolation has been carried out on the data. However, the Fourier transform changes that.

There is often confusion regarding the way in which the Fourier transform introduces statistical correlations. It appears an obvious fact that each point in $G(r)$ contains information from every point in $S(Q)$ because each point in $G(r)$ comes from an integration over all of $S(Q)$. However, this does not introduce statistical correlations *per se*. To see this, remember that the integration is just the limiting form of a sum. Each term in the sum contains a stochastic observation ($[S(Q)-1]$) with a coefficient ($Q \sin(Qr)\Delta Q$) and so, according to Eq. (A5.3.6), the variance on $G(r)$ is

$$\operatorname{var}(G(r_m)) = \frac{4}{\pi^2} \sum_i (Q_i \sin(Q_i r_m)\Delta Q_i)^2 \operatorname{var}(S(Q_i)). \qquad \text{(A5.3.9)}$$

This is a linear expression, and even though this point in $G(r)$ depends on the data in each and every point in $S(Q)$, there is no covariance term because the data points themselves are statistically independent. Thus, $\sigma(G(r_m)) = \sqrt{\operatorname{Var}(G(r_m))}$ gives a good estimate of the random errors on the mth point in G(r) at r_m.

The problem arises when you want to consider the errors from a quantity which depends on a series of points in $G(r)$. For example, perhaps you want to ask the question, what is the error on the integrated peak intensity for a peak in $G(r)$? The problem here is that neighboring points in $G(r)$ are not statistically independent. This is because there is a finite r-space resolution to the measurement of $G(r)$ that is dictated by the experiment: it comes from the finite range of Q over which the measurement was made. To a reasonable approximation, we can estimate the resolution in $G(r)$ as being π/Q_{max}. Based on this, we can guess that points within a distance $\Delta r < \pi/Q_{max}$ of each other in $G(r)$ will be statistically correlated. One approach to circumvent this problem is to evaluate $G(r)$ on a grid of points separated by $\Delta r < \pi/Q_{max}$ and to a reasonable approximation the points in $G(r)$ will be statistically independent. This approach often presents difficulties when relatively sharp features are

present in the PDF, such as is the case in crystalline materials, because there are then relatively few points defining each peak and therefore a poorly defined peak profile. This becomes hard to model quantitatively and this approach is not widely used. It is also approximate in any case since it is not true that points less widely spaced than $\pi/Q_{\max}$ are completely correlated and those more widely spaced are completely uncorrelated.

The statistical correlations between points m and n in the PDF, cov(G_m, G_n), can be determined. Assume that an experimentally measured $S(Q_i) = \bar{S}(Q_i) + \varepsilon(Q_i)$, where $\varepsilon(Q)$ is a small fluctuation due to random errors in the particular measurement and $\bar{S}(Q_i)$ is the average $S(Q)$ that you would get from making many measurements. Then, according to Eq. (3.1), the measured

$$
\begin{aligned}
G(r) &= \frac{2}{\pi} \sum_i Q_i [S(Q_i) - 1] \sin Q_i r \Delta Q_i \\
&= \frac{2}{\pi} \sum_i Q_i [\bar{S}(Q_i) - 1] \sin Q_i r \Delta Q_i + \frac{2}{\pi} \sum_i Q_i \varepsilon(Q_i) \sin Q_i r \Delta Q_i \\
&= \bar{G}(r) + \frac{2}{\pi} \sum_i Q_i \varepsilon(Q_i) \sin Q_i r \Delta Q_i.
\end{aligned}
\tag{A5.3.10}
$$

From this, we can get the variance on $G(r)$,

$$
\begin{aligned}
\text{var}(G) &= \left\langle (G - \bar{G})^2 \right\rangle = \left\langle \left(\frac{2}{\pi} \sum_i Q_i \varepsilon(Q_i) \sin Q_i r \Delta Q_i \right)^2 \right\rangle \\
&= \frac{4}{\pi^2} \sum_i Q_i^2 \left\langle \varepsilon^2(Q_i) \right\rangle \sin^2 Q_i r \Delta Q_i^2 \\
&\quad + \frac{4}{\pi^2} \sum_{i \neq j} Q_i Q_j \left\langle \varepsilon(Q_i) \varepsilon(Q_j) \right\rangle \sin Q_i r \sin Q_j r \Delta Q_i \Delta Q_j.
\end{aligned}
\tag{A5.3.11}
$$

The second sum is zero since $\langle \varepsilon(Q_i) \varepsilon(Q_j) \rangle = 0$ because the errors on different points in Q are uncorrelated and averaging over many measurements will yield zero. Thus, since by definition, $\langle \varepsilon^2(Q_i) \rangle = \text{var}(S(Q))$, we recover Eq. (A5.3.9) for var(G).

From Eq. (A5.3.6), we see that, similarly, $(G_m, G_n) = \left\langle (G_m - \bar{G}_m)(G_n - \bar{G}_n) \right\rangle$, where G_m is the value of $G(r)$ at the point $r = r_m$. Thus,

$$
\begin{aligned}
\text{cov}(G_m, G_n) &= \left\langle \left(\frac{2}{\pi} \sum_i Q_i \varepsilon(Q_i) \sin Q_i r_m \Delta Q_i \right) \left(\frac{2}{\pi} \sum_j Q_j \varepsilon(Q_j) \sin Q_j r_n \Delta Q_j \right) \right\rangle \\
&= \frac{4}{\pi^2} \sum_i Q_i^2 \left\langle \varepsilon^2(Q_i) \right\rangle \sin Q_i r_m \sin Q_i r_n \Delta Q_i^2 \\
&\quad + \frac{4}{\pi^2} \sum_{i \neq j} Q_i Q_j \left\langle \varepsilon(Q_i) \varepsilon(Q_j) \right\rangle \sin Q_i r_m \sin Q_j r_n \Delta Q_i \Delta Q_j.
\end{aligned}
$$

$$\tag{A5.3.12}$$

As before the second sum is always zero. However, in this case, terms in the first sum are not always positive as in the case of the variance, Eq. (A5.3.11), because at a particular Q-point, the product ($\sin Q_i r_m \sin Q_i r_n$) can be positive or negative. In fact, it will periodically oscillate from positive to negative and taking the sum to infinity will result in a complete cancelation of the terms in the sum. Thus, an ideal infinite Fourier transform results in $\mathrm{cov}(G_m, G_n) = 0$ and does not introduce statistical correlations between points in the PDF as we already discussed. However, summing over a finite range will yield a finite covariance given by

$$\mathrm{cov}(G_m, G_n) = \frac{4}{\pi^2} \sum_{i=1}^{N} Q_i^2 \sin Q_i r_m \sin Q_i r_n \Delta Q_i^2 \, \mathrm{var}(S(Q_i)). \qquad (A5.3.13)$$

In particular, when the two points m and n are close together in r, the two sine-waves will have nearly the same wavelength and be in phase, producing a positive product, over a significant range of the sum. When the points are further apart, the two sine-waves go out of phase quickly and terms in the sum tend to cancel (though not completely).

Once the covariance matrix is calculated, the true variance of functions of G can be determined using Eqs. (A5.3.5) and (A5.3.6). For example, the integral of a peak in $G(r)$ is simply $I_G = \sum_{m=l}^{h} G_m \Delta r_m$, where the sum runs from a point l below the peak to a point h above it, so

$$\mathrm{var}(I_G) = \sum_{m=l}^{h} \mathrm{var}(G_m)(\Delta r_m)^2 + 2 \sum_{m,n=l(m>n)}^{h} \mathrm{cov}(G_m, G_n) \Delta r_m \Delta r_n. \quad (A5.3.14)$$

To summarize, it is possible to estimate the random errors on each point individually in the PDF by propagating the random counting statistics of the raw data. This gives a variance on each point in the PDF that is accurate. However, because the number of points in the PDF is arbitrary, but the amount of information in the PDF is not, we find that the errors in neighboring points in the PDF are correlated. From a practical point of view, points in the PDF which are separated by more than $\approx \pi/Q_{\max}$ are statistically independent. Care must be taken when evaluating the errors on quantities that depend on more than one PDF point such as integrated peak intensities. The variance on this quantity is not given by the weighted sum of the variances on each of the PDF points in the sum because of the statistical correlations. However, in principle, the covariance matrix between points in the PDF can be evaluated straightforwardly and using this information, statistically reliable variances can be determined even on functions involving more than one point in the PDF.

APPENDIX 5.4.   OPTIMIZING DATA FOR DIRECT FOURIER TRANSFORM

The sample $S(Q)$ is obtained after making all the corrections outlined in Section 5.3. This function has certain known properties, such as the high- and

low-Q asymptotes that allow the data analyst to check the efficacy of the sample corrections. When these functional properties are not obeyed, the corrections procedure can be adjusted and $S(Q)$ recalculated. The most important asymptote that must be obeyed is $\lim Q \to \infty S(Q) = 1$. This will automatically be obeyed in the case of X-ray data analysis where this criterion is used to find the normalization constant for the data (Eq. 5.23). In the case of tof neutron analysis, in principle, it is possible to get an absolute $S(Q)$ directly from the corrections.

In this case, the usual procedure taken when $S(Q)$ does not asymptote properly is to vary a parameter such as sample density until the proper asymptote is achieved. The problem with this is that some corrections are multiplicative and some additive, and in any given situation, it is not clear which corrections went wrong resulting in the improper asymptote. Varying the sample density is a somewhat arbitrary response which produces a mostly, but not completely, multiplicative correction. This is not a problem if the data are to be modeled since a scale factor can be used in any model; however, it can present a problem when a model independent analysis is to be applied to the data (Chapter 6).

Another more recent data analysis problem is simply that of handling very large numbers of data points that are being generated at high-throughput instruments such as GEM at ISIS and upcoming instruments at the SNS. Arduous manual iterative corrections are clearly not feasible in this situation. An approach has been proposed for automating this "$S(Q)$ optimization" process (Peterson *et al.*, 2003). Constant multiplicative and additive constants are used to modify $S(Q)$ according to

$$S'(Q) = \alpha S(Q) + \beta. \tag{A5.4.1}$$

The factors α and β are varied in such a way as to optimize quantitative PDF quality criteria that give a measure of the quality of the PDF. In particular, the most useful quality criterion is one that empirically measures the size of ripples coming from systematic errors in the data in the unphysical low-r region of $G(r)$. This empirical quality parameter is defined as,

$$G_{low} = \frac{\int_0^{r_{low}} r^2 \left[G(r) + 4\pi r \rho_{fit} \right]^2 dr}{\int_0^{r_{low}} [4\pi r \rho_{fit}]^2 dr}. \tag{A5.4.2}$$

First, a straight line is fit through $G(r)$ from $G(0) = 0$ to a point r_{low} below the first peak in the PDF. It was found that best results were obtained when an r^2 weighting was used in the fit, so it was not biased by large ripples at very low-r (Peterson *et al.*, 2003). This line has a slope of $-4\pi\rho_{fit}$ which serves to define ρ_{fit}. G_{low} is then evaluated according to Eq. (A5.4.2). A least-squares regression is then applied where α and/or β are systematically varied to minimize G_{low}. In this way, the fine tuning of the data normalization can be automated.

The regression can also be constrained so that α and β are varied in such a way that $\rho_{\text{fit}} = \rho_0$, the real sample number density. In this way, a $G(r)$ is produced with a scale factor of approximately one, though because of the arbitrariness of the corrections the real scale factor should be determined from modeling.

If the probable source of the problem is known, some more meaningful steps can be taken to correct the data; for example, multiple scattering that takes place first in the sample, then elsewhere in the apparatus. This kind of multiple scattering is not accounted for in the corrections. This becomes a problem for samples that have a significant amount of incoherent scattering. In this case, the ratio of multiple scattering (that depends on the total scattering cross section) to signal (that depends on the coherent cross section) is higher, and it becomes more critical to correct for this source of multiple scattering to get a properly normalized $S(Q)$. This effect has been noticed, for example, in scattering from compounds of elements with a mixture of positive and negative neutron scattering lengths such as the manganites (Louca, 2003). In this case, a nickel standard can be measured that has the same total scattering cross section (and therefore approximately the same sample/apparatus multiple scattering) as the sample under study. The Nickel data are analyzed using the imperfect corrections. The nickel data are modeled and additive and multiplicative corrections made to the data until a scale factor of one and the correct high-Q asymptote are obtained. The additive correction is presumed to come from the uncorrected multiple scattering which is proportional to the total sample cross section. The additive correction suitable for the real experiment is then obtained by rescaling the additive constant found for the Ni by the ratio of the sample and nickel total cross sections,

$$\beta_s = \beta_{\text{Ni}} \left(\frac{\rho^s V'_s \langle b_s^2 \rangle}{\rho^{\text{Ni}} V'_{\text{Ni}} \langle b_{\text{Ni}}^2 \rangle} \right). \tag{A5.4.3}$$

Here, it is the actual sample (powder) densities that are used. The effective sample volumes (Appendix 5.1) can be replaced by the real sample volumes without loss of accuracy, provided the absorption cross sections of the sample and data are similar.

The approach of using a standard and modeling it to obtain a scale factor, or indeed if the structure of the material is known with some certainty modeling the sample PDF itself, is a useful way of obtaining properly normalized data. Since two independent variables need to be known, α and β, two pieces of information are needed to constrain them. The high-Q asymptote of $S(Q)$ is one piece of information. A convenient but imprecise additional piece of information is ρ_{fit}, defined above. Using the scale factor from modeled data as described here is another, more arduous but more reliable method, for fixing the second parameter. This is true regardless of whether the scale error results from multiple scattering or not. As we said before, if no scale-dependent model-independent analyses (such as integrating PDF peak intensities) are to be carried out,

accurate data normalization is less important, provided sample scale factor is present as a parameter in any modeling (Peterson *et al.*, 2003).

APPENDIX 5.5. DATA CORRECTIONS EXAMPLE: TOF NEUTRON: PDFgetN

To illustrate the process of obtaining the total scattering structure function, $S(Q)$, and thence a PDF from tof neutron data, we show an example of a typical data analysis using the PDFgetN program (Peterson *et al.*, 2000). The analysis steps carried out by the program are described in detail earlier in this chapter and in Appendices 5.1–5.3. This program runs on windows, linux, and most unix platforms. It is available from total scattering home-page (http://www.totalscattering.org/). The description reproduced here draws heavily from one of the tutorial examples in the program distribution.

The data analyzed in this illustration are from a sample of $La_{0.75}Ca_{0.25}MnO_3$ and belongs to the family of manganites exhibiting the so-called colossal magneto-resistance effect. The data were measured at 300 K on the special environment powder diffractometer (SEPD) at the intense pulsed neutron source (IPNS) at Argonne National Laboratory. This instrument has 160 detectors that are grouped into distinct banks centered at certain angles. Data from detectors away from the central angle are "time focussed" electronically so that the same "Q-value" is binned in the same "time-channel" for all the detectors in the bank. The binning of data from various detectors into detector banks is done electronically during the data collection. The assignment of detectors to detector banks is controlled by a user-defined "histogram"' which is chosen at data-collection time. In the current histogram, the beam monitor is designated as bank 5 and there are 8 banks in total. The sample was filled in an extruded vanadium container that had an inner radius and wall thickness of 0.5559 and 0.0127 cm, respectively. The experimental environment consisted of a closed-cycle helium refrigerator with an aluminum heat shield mounted. The data that were collected are summarized in Table A5.5.1.

TABLE A5.5.1 Datasets That are Used in the Data Analysis Example Presented Here

Dataset	Data run numbers
Sample	Sepd9085.asc
Empty container	Sepd9060.asc
Vanadium rod; no shields	Sepd9061.asc
Empty instrument	Sepd9062.asc

The PDFgetN program has an X-windows GUI interface for straightfor-
ward data input and analysis. It also has embedded data such as atomic
weights and neutron scattering cross sections to speed up the data analysis
process. Finally, one of the philosophies behind the PDFgetN program is that
all of the parameters used to obtain a particular PDF are stored within the PDF
file itself. This is known as the data analysis HISTORY. This is important for
the purposes of reproducibility and accountability: given the raw data and the
analysis parameters it should always be possible for someone to reproduce a
particular PDF; and to see exactly what input parameters were used to get
it. However, it has one additional advantage. The PDFgetN program can read
this history information from the PDF file and enter it into its various input
fields. These can then be modified as desired to carry out the data analysis.
This makes analyzing multiple similar datasets (e.g., a temperature series)
very straightforward because the great majority of the inputs do not change
from one dataset to another.

The user first selects the correct template for the particular diffractometer
that was used to collect the data; in this case, SEPD. The experimental infor-
mation is then typed into the various fields as shown in Fig. A5.5.1. Note that
no instrument background is subtracted from the vanadium rod. This is
because SEPD has inherently a very low background that is negligible for
the vanadium rod measurement which is carried out with no heat shields in
place. A background from the empty instrument is measured for the data

FIGURE A5.5.1   Experimental information window of PDFgetN. Note the "Create $S(Q)$" and
"Plot" buttons. Once essential information, such as sample composition and dimensions, is
entered, $S(Q)$, and $G(r)$ are just the click of a button away.

collected with heat shields in place. Data from the sample are not smoothed. By default, the empty container, vanadium rod, and sample background will be smoothed using a Savitzky–Golay filter of zeroth order. This is done to improve statistics on the assumption that all the backgrounds are slowly varying and smoothing them will not introduce significant distortions. Smoothing can be turned off if desired. The tiny residual Bragg-peaks are also removed from the vanadium data by default. The severity of smoothing, and the smoothing protocol, are controlled by varying the "smoothing parameters" fields.

Once the experimental information is filled in the sample information is entered, as shown in Figs. A5.5.2 and A5.5.3. The chemical elements in the
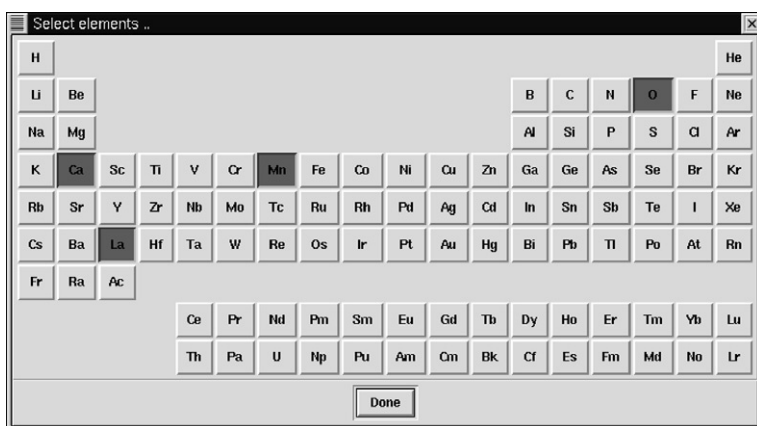
FIGURES A5.5.2   Window in PDFgetN for selecting chemical elements present in the sample.
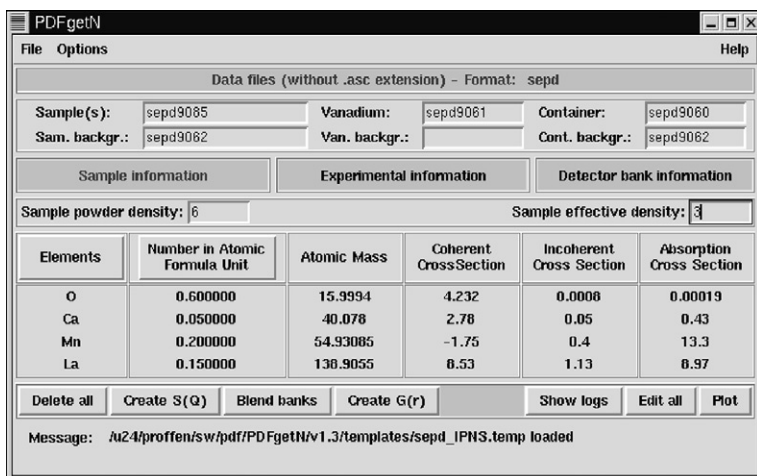

FIGURE A5.5.3   Sample information window of PDFgetN.

sample are selected from the pop-up periodic table window (Fig. A5.5.2) and the chemical formula entered from the keyboard. The neutron scattering cross sections that will be used automatically appear as shown in Fig. A5.5.3. All these values can be edited manually in the history file if necessary. The sample powder density is the weight of the sample divided by its volume (i.e., the density of the loose powder). This is not used explicitly anywhere in the analysis and may be left blank. Instead, the density is treated like a parameter that is used to normalize the data and takes the name "effective density." This field has to contain a value for the program to run and a good initial value is the true sample (powder) density, if it was measured, or alternatively 0.5 times the theoretical density of the sample.

Next, information about the detector histogram must be entered. This window is shown in Fig. A5.5.4. This histogram information is contained in the header of the data runfile and can be automatically obtained by running a preliminary analysis (clicking the "create $S(Q)$" button) which creates an intermediate file containing the detector bank information. PDFgetN will then ask the user if this information should be accepted and will automatically load it.

With the experimental information all entered, it is now possible to proceed with the analysis by clicking "create $S(Q)$." The resulting $S(Q)$ is calculated for each bank. When the program finishes, this information can be viewed using the interactive plotting capability, as shown in Fig. A5.5.5. The user can zoom in on different parts of the PDF by defining regions using the mouse. If the data are not properly normalized; that is, the $S(Q)$ values do not approach unity at high-Q, the effective density can be modified and the analysis rerun. If the $S(Q)$ values from different detector banks do not properly

PDFgetN								
File Options								Help
Data files (without .asc extension) – Format: sepd								
Sample(s): sepd9085			Vanadium: sepd9061			Container: sepd9060		
Sam. backgr.: sepd9062			Van. backgr.:			Cont. backgr.: sepd9062		
Sample information			Experimental information			Detector bank information		
Bank Number	Angle	Qmin	Qmax	Include Bank	Add Data	Add Background	Multiply Data	Multiply Background
1	139.69	2.24	46.03	■				
2	150.00	2.30	47.32	■				
3	90.00	1.69	34.51	■				
4	60.00	1.19	24.26	■				
5	14.62	0.30	6.12	■				
6	29.78	0.61	12.12	■				

Combined S(q) data: Qmin: 0.30   Qmax: 47.32

Delete all	Create S(Q)	Blend banks	Create G(r)		Show logs	Edit all	Plot

Message: Intensity file with bank information created

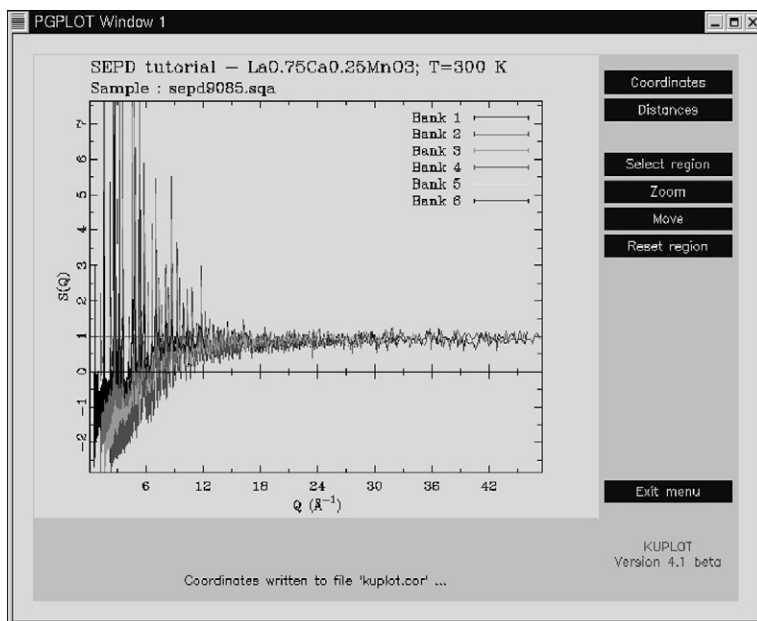FIGURE A5.5.4   Detector-bank information in PDFgetN.

FIGURE A5.5.5   Plot window for PDFgetN here showing $S(Q)$ from six detector banks. The plot can be zoomed by selecting regions using the mouse. By positioning the cursor and clicking the mouse, it is also possible to get coordinates.

line up with each other, then the data can be scaled bank by bank, or a constant added to a bank, to line the data up. Bank by bank variations require corrections of less than 5% in general and a larger correction may indicate a problem with the data in one of the banks; for example, a noisy detector. In this case, banks can be eliminated from the analysis or raw data can sometimes be reprocessed with particular detectors eliminated from the bank. Remember to reprocess the vanadium data, used for normalization, in the same way even if the detectors are all good in the vanadium dataset! $S(Q)$ values that slope at high-Q often indicate problems with the background/empty can subtraction; it might be necessary to change some of the can parameters or scale the background.

Once satisfied with the result, the data can be blended. The range of data to be accepted from each bank is specified in the bank parameters. The bank-by-bank $S(Q)$ values are then combined into a single $S(Q)$ to improve the overall statistics. The result is shown in Figs. A5.5.6 and A5.5.7 in the form of $S(Q)$ and the reduced structure function $Q[S(Q) - 1]$, respectively.

The reduced structure function, $Q[S(Q) - 1]$ oscillates around zero at high-Q. The signal-to-noise ratio is decreasing with increasing Q in $S(Q)$ because of the Debye–Waller factor. This effect is exacerbated in the reduced structure function, $Q[S(Q) - 1]$ because of the Q-weighting which multiplies the high-Q
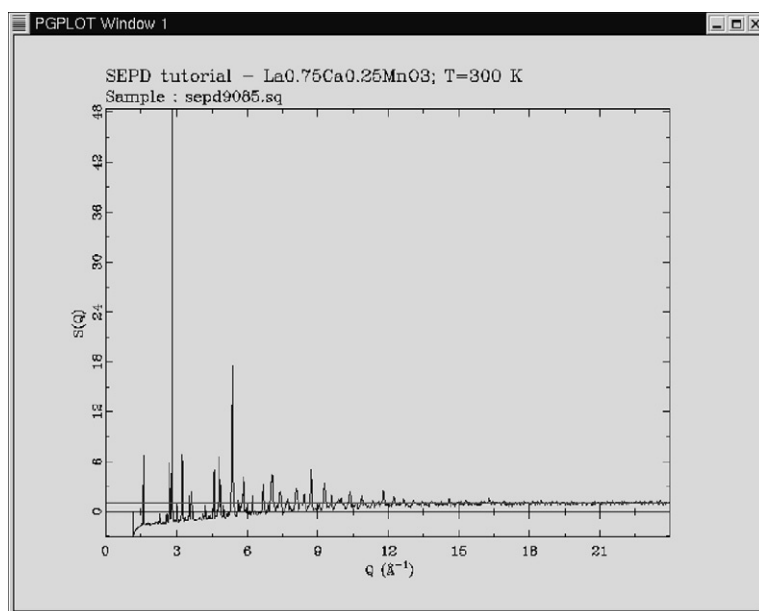
FIGURE A5.5.6   Blended *S*(*Q*) in the PDFgetN plot window.
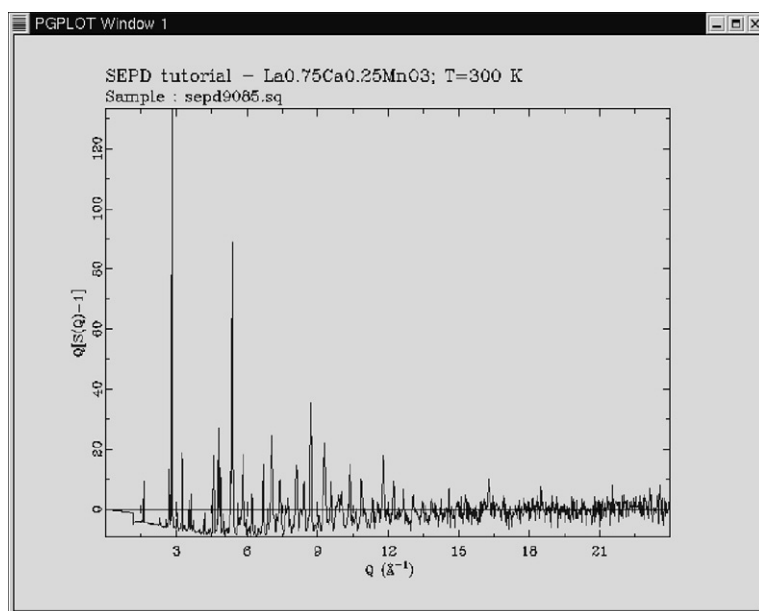

FIGURE A5.5.7   Same as Fig. A5.5.6 but plotted as the reduced structure function, *Q*[*S*(*Q*) − 1].

region by Q which can be as much as a factor of 50! The data are terminated at a value of Q_{max} that is chosen depending on the signal-to-noise ratio in the reduced structure function. This underscores the importance of getting good statistics in the high-Q region of the data. In this case, a Q_{max} of 24 Å^{-1} was chosen. The data are then Fourier transformed by clicking the "create $G(r)$" button resulting in the PDF shown in Fig. A5.5.8.

These data from a manganite sample are particularly challenging because of the relatively weak coherent, and strong incoherent, scattering of the sample due to the negative scattering length of manganese. This results in significant backgrounds relative to the coherent scattering intensity so that imperfections in the corrections have an exaggerated effect. The negative scattering length of manganese is evident by the observation of Mn-O and Mn-(La,Sr) peaks which are negative (e.g., the peak at 1.9 Å). The imperfect corrections are apparent because the function $G(r)$ does not decrease linearly from the origin with the slope of $-4\pi\rho_0$ in the region below the first peak at 1.9 Å as expected theoretically. In fact, the deviations from this behavior are quite dramatic (and much worse than observed for typical datasets on better behaved samples). Nonetheless, the data in the structural region are still of high quality. This is borne out by model fits to the data.
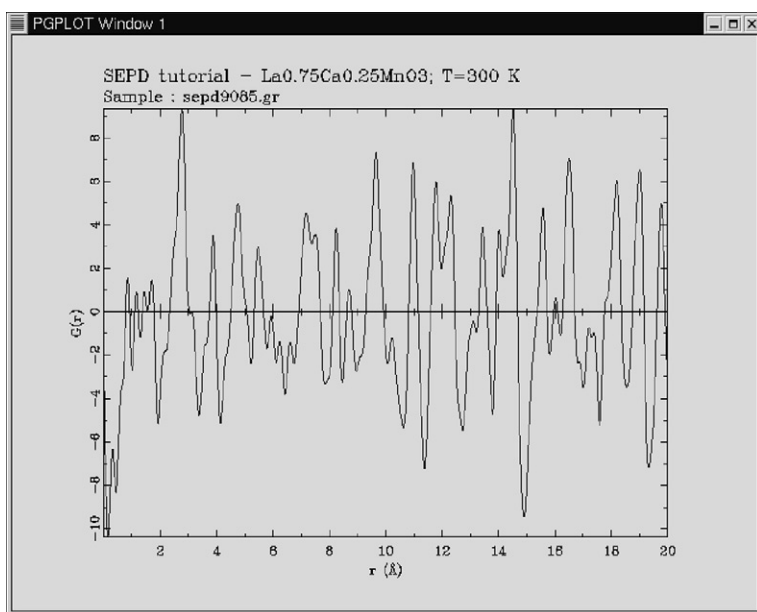

FIGURE A5.5.8 Reduced pair distribution function, $G(r)$, from the data shown in Figs. A5.5.5–A5.5.7, shown in the PDFgetN plot window.

REFERENCES

Abeykoon, M., Malliakas, C.D., Juhas, P., Bozin, E.S., Kanatzidis, M.G., Billinge, S.J.L. (2012) *Z. Kristallogr., ***227**, 248.

Ankudinov, A.L. & Rehr, J.J. (2000) *Phys. Rev. B*, **62**, 2437.

Bevington, P.R., Robinson, K.D. & Bunce, G. (1992) *Data Reduction and Error Analysis for the Physical Sciences* (2nd Edition). New York: McGraw-Hill.

Billinge S.J.L., 1992. Local Atomic Structure and Superconductivity of $Nd_{2-x}Ce_xCuO_{4-y}$: A Pair Distribution Function Study. University of Pennsylvania, Thesis.

Billinge, S.J.L., Farrow C.L., 2012. (to be published).

Billinge, S.J.L., Farrow, C.L., Juhas, P. 2011. Patent 61/563258.

Blech, I.A. & Averbach, B.L. (1965) *Phys. Rev. A*, **137**, 1113.

Bodek, K., Böni, P., Hilbes, C., Lang, J., Lasakov, M., Lüthy, M., Kistryn, S., Markiewicz, M., Medviediev, E., Pusenkov, V., Schebetov, A., Serebrov, A., Sromicki, J. & Vasiliev, A. (2000) *Neutron News*, **3**, 29.

Chupas, P.J., Qiu, X., Hanson, J.C., Lee, P.L., Grey, C.P. & Billinge, S.J.L. (2003) *J. Appl. Crystallogr.*, **36**, 1342.

Cowley, J.M. (1992) *Electron Diffraction Techniques*. Oxford: Oxford University Press.

Cromer, D.T. & Liberman, D.A. (1970) *J. Phys. Chem.*, **53**, 1891.

Cumbrera, F.L. & Sanchez-Bao, F. (1995) *J. Appl. Crystallogr.*, **28**, 408.

Dimitrov, D., Röder, H. & Louca, D. (1999) *Phys. Rev. B*, **60**, 6204.

Doyle, P.A. & Turner, P.S. (1968) *Acta Crystallogr.*, **24**, 390.

Dwiggins, C.W.Jr., (1972) *Acta Crystallogr. A*, **28**, 155.

Dwiggins, C.W. & Park, D.A.Jr., (1971) *Acta Crystallogr. A*, **27**, 264.

Egami, T. (1978) *J. Mater. Sci.*, **13**, 2587.

Ergun, S. (1968) J.P.L. Walker (Ed.), *Chemistry and Physics of Carbon* (p. 211). New York: Marcel Dekker.

Farrow, C.L., Shaw, M., Kim, H.J., Pavol, J. & Billinge, S.J.L. (2011) *Phys. Rev. B*, **84**, 134105.

Fox, A.G., O'Keefe, M.A. & Tabbernor, M.A. (1989) *Acta Crystallogr. A*, **45**, 786.

Hammersley, A.P. 2004. ESRF Internal Reprot ESRF98HA01T.

Hammersley, A.P., Svenson, S.O., Hanfland, M. & Hauserman, D. (1996) *High Press. Res.*, **14**, 235.

Hannon, A.C., Howells, W.S. & Soper, A.K. (1990) *Neutron Scattering Data Analysis Institute of Physics Conference Series* **107**, (p. 193). .

Hinrichsen, B., Dinnebier, R.E. & Jansen, M. (2006) *Z. Kristallogr.*, **23**(Supplement), 231.

Howe, M.A., McGreevy, R.L. & Howells, W.S. (1989) *J. Phys. Condens. Matter*, **1**, 3433.

Howells, W.S. (1984) *Nucl. Instrum. Methods*, **219**, 543.

Howells, W.S. (1985) *Nucl. Instrum. Methods*, **235**, 553.

Howells, W.S. 1986. Rutherford Appleton Laboratory Report, RAL-86-042.

Hubbell, J.H., Seltzer, S.M. 1997. *Tables of X-ray Mass Attenuation Coefficients and Mass Energy-Absorption Coefficients* (version 1.03), [Online]. Available: http://physics.nist.gov/xaamdi [2002, February 25]. National Institute of Standards and Technology, Gaithersburg, MD. Originally published as NISTIR 5632, National Institute of Standards and Technology, Gaithersburg, MD. 1995.

Hughes, I.G. & Hase, T.P.A. (2010) *Measurements and their Uncertainties: A Practical Guide to Modern Error Analysis*. Oxford: Oxford University Press.

Ida, T. & Toraya, H. (2002) *J. Appl. Crystallogr.*, **35**, 58.

Ino, T. (1957) *J. Phys. Soc. Jpn.*, **12**, 495.

Juhas, P., Dykhne, T., Farrow, C.L., Billinge, S.J.L. 2012. (to be published).

Kaplow, R., Strong, S.L. & Averbach, B.L. (1965) *Phys. Rev. A*, **138**, 1336.

Kaszkur, Z. (1990) *J. Appl. Crystallogr.*, **23**, 180.

Kendig, A.P. & Pings, C.J. (1962) *J. Appl. Phys.*, **36**, 1692.

Kissel, L., Zhou, B., Roy, S.C., Sengupta, S.K. & Pratt, R.H. (1995) *Acta Crystallogr. A*, **51**, 271.

Klug, H.P. & Alexander, L.E. (1968) *X-ray Diffraction Procedures for Polycrystalline and Amorphous Materials*. New York: Wiley.

Kolb, U., Mugnaioli, E. & Gorelik, T.E. (2011) *Cryst. Res. Technol.*, **46**, 542.

Laaziri, K., Kycia, S., Roorda, S., Chicoine, M., Robertson, J.L., Wang, J. & Moss, S.C. (1999) *Phys. Rev. B*, **60**, 13520.

Leadbetter, A.J. & Wright, A.C. (1972) *J. Non-Crystal. Solids*, **7**, 141.

Lorch, E. (1969) *J. Phys. C*, **2**, 229.

Louca, D. (2003) *J. Phys. Chem. Solids*, **64**, 343.

Lovell, R., Mitchell, G.R. & Windle, A.H. (1979) *Acta Crystallogr. A*, **35**, 598.

Lovesey, S.W. (1984) *Theory of Neutron Scattering from Condensed Matter*. Oxford: Oxford Science Publications.

Masadeh, A.S., Bozin, E.S., Farrow, C.L., Paglia, G., Juhas, P., Karkamkar, A., Kanatzidis, M.G. & Billinge, S.J.L. (2007) *Phys. Rev. B*, **76**, 115413.

Narayan, R. & Ramaseshan, S. (1979) *J. Appl. Crystallogr.*, **12**, 585.

Nield, V.M. & Keen, D.A. (2001) *Diffuse Neutron Scattering from Crystalline Materials*. Oxford: Oxford Science Publications.

Paalman, H.H. & Pings, C.J. (1962) *J. Appl. Phys.*, **33**, 2635.

Paalman, H.H. & Pings, C.J. (1963) *Rev. Mod. Phys.*, **35**, 389.

Page, K., White, C.E., Estell, E.G., Reinhard, B. & Neder, A. (2011) *J. Appl. Crystallogr.*, **44**, 532.

Peralta, M. (2012) *Propagation of Errors: How to Mathematically Predict Measurement Errors to First and Second Order*. United States: CreateSpace.

Peterson, P.F., Gutmann, M., Proffen, T. & Billinge, S.J.L. (2000) *J. Appl. Crystallogr.*, **33**, 1192.

Peterson, P.F., Bozin, E.S., Proffen, Th. & Billinge, S.J.L. (2003) *J. Appl. Crystallogr.*, **36**, 53.

Petkov, V. (1989) *J. Appl. Crystallogr.*, **22**, 387.

Petkov, V. & Danev, R. (1998) *J. Appl. Crystallogr.*, **31**, 609.

Petkov, V., Jeong, I.-K., Mohiuddin-Jacobs, F., Proffen, T. & Billinge, S.J.L. (2000) *J. Appl. Phys.*, **88**, 665.

Placzek, G. (1952) *Phys. Rev.*, **86**, 377.

Poncett, P.F.J. 1977. ILL Internal Report, 77PO139S.

Powles, J.G. (1973) *Mol. Phys.*, **26**, 1325.

Price, D.L. & Saboungi, M.-L. (1998) S.J.L. Billinge & M.F. Thorpe (Eds.), *Local Structure from Diffraction* (p. 23). New York: Plenum.

Prince, E. (1982) *Mathematical Techniques in Crystallography and Materials Science*. New York: Springer-Verlag.

Prince, E. (1994) *Mathematical Techniques in Crystallography and Materials Science* (2nd Edition). New York: Springer-Verlag.

Pusztai, L. & McGreevy, R.L. (1997) *Phys. B*, **234–236**, 357.

Qiu, X., Thompson, J.W. & Billinge, S.J.L. (2004) *J. Appl. Crystallogr.*, **37**, 678.

Ruland, W. (1964) *Br. J. Appl. Phys.*, **15**, 1301.

Sears, V.F. (1975) *Adv. Phys.*, **24**, 1.

Serimaa, R., Pitkanen, T., Vahvaselka, S. & Paakkari, T. (1990) *J. Appl. Crystallogr.*, **23**, 11.

Shannon, C.E. (1949) *Proc. IRE*, **37**, 10.

Soper, A.K. & Egelstaff, P.A. (1980) *Nucl. Instrum. Methods*, **178**, 415.

Soper, A.K., Howells, W.S., Hannon, A.C. 1989. Rutherford Appleton Laboratory Report, RAL-89-046.

Soper, A.K. (1990) *Neutron Scattering Data Analysis Institute of Physics Conference Series* **107**, (p. 57).

Taylor, J.R. (1997) *An Introduction to Error Analysis: The Study of Uncertainties in Physical Measurements*. Sausalito: University Science Books.

Terwilliger, T.C. (1994) *Acta Crystallogr. D*, **50**, 11–16.

Thijsse, B.J. (1984) *J. Appl. Crystallogr.*, **17**, 61.

Tian, P. & Billinge, S.J.L. (2011) *Z. Kristallogr.*, **226**, 898.

Thorpe, M.F., Levashov, V.A., Lei, M. & Billinge, S.J.L. (2002) S.J.L. Billinge & M.F. Thorpe (Eds.)*, From Semiconductors to Proteins: Beyond the Average Structure*. New York: Kluwer/Plenum.

Toby, B.H. (2005) *J. Appl. Crystallogr.*, **38**, 1040.

Toby, B.H. & Billinge, S.J.L. (2004) *Acta Crystallogr. A*, **60**, 315.

Toby, B.H. & Egami, T. (1992) *Acta Crystallogr. A*, **48**, 336.

Tucker, M.G., Dove, M.T. & Keen, D.A. (2001) *J. Appl. Crystallogr.*, **34**, 780.

Waasmaier, D. & Kirfel, A. (1995) *Acta Crystallogr. A*, **51**, 416.

Warren, B.E. (1990) *X-ray Diffraction*. New York: Dover.

Waser, J. & Schomaker, V. (1953) *Rev. Mod. Phys.*, **25**, 671.

Wilson, A.J.C. (1995) *International Tables for Crystallography*. Dordecht: Kluwer Academic Press.

Yang, X., Billinge, S.J.L. 2012. (unpublished).

Yang, X., Juhas, P., Dykhne, T., Farrow, C.L., Billinge, S.J.L. unpublished.

Yarnell, J.L., Katz, M.J., Wenzel, R.G. & Koenig, S.H. (1973) *Phys. Rev. A*, **7**, 2130.

Selected Bibliography

Overviews of data corrections: Some of the best resources are the manuals and the tutorial sections of data analysis programs mentioned in the text. Some additional resources are below.

Wagner, C.N.J. (1978) *J. Non-Crystal. Solids*, **31**, 1.

Waseda, Y. (1980) *The Structure of Non-Crystalline Materials*. New York: McGraw-Hill.

Pynn, R. 1990. Neutron Scattering—A Primer, Los Alamos Science #19 Excellent Background on Neutron Scattering in General.

Wright, A.C., Vessal, B., Bachra, B., Hulme, R.A., Sinclair, R.N., Clare, A.G. & Grimley, D.I. (1995) D.A. Neumann, T.P. Russell & B.J. Wuensch (Eds.), *Neutron Scattering for Materials Science II*. Warrendale: Materials Research Society Publications.